2015-02-01

Energy Process Enabled by Cryogenic Carbon Capture

Mark Jensen
Brigham Young University - Provo

Energy Processes Enabled by Cryogenic Carbon Capture

Mark J. Jensen

A dissertation submitted to the faculty of
Brigham Young University
in partial fulfillment of the requirements for the degree of

Doctor of Philosophy

Larry L. Baxter, Chair
Morris D. Argyle
David Frankman
Thomas Knotts
John Hedengren

Department of Chemical Engineering

Brigham Young University

February 2015

ABSTRACT

Energy Processes Enabled by Cryogenic Carbon Capture

Mark J. Jensen
Department of Chemical Engineering, BYU
Doctor of Philosophy

Global climate change concerns help shape current environmental regulations, which increasingly seek to reduce or capture CO_2 emissions. Methods for capturing CO_2 emissions from energy processes have been the focus of numerous studies to provide support for those seeking to reduce the environmental impact of their processes. This research has (1) simulated a baseline case of energy-storing cryogenic carbon capture for implementation on a 550 MW_e coal fired power plant, (2) presented a novel cryogenic carbon capture process for removing CO_2 from natural gas down to arbitrary levels, (3) presented a natural gas liquefaction process that has the ability to be highly CO_2 tolerant, and (4) developed theoretical models and their experimental validation of CO_2 capture predictions for all aforementioned processes.

Keywords: Cryogenic Carbon Capture, CCC, External Cooling Loop, ECL, energy storage, natural gas processing, liquefied natural gas, LNG

ACKNOWLEDGEMENTS

I would like to acknowledge the loving support of my wife, Hayley, and my son, Jeffrey. They were always supportive and very understanding.

I am very appreciative of my graduate committee. I am especially grateful to Dr. Larry Baxter for his time and patience with me. He was truly a great mentor and adviser and gave me excellent opportunities to grow. I'm also thankful for Dr. Thomas Knotts' help with evaluating thermodynamic data.

I am very thankful to fellow students that have performed research with me, and have worked alongside me. I thank David Bergeson and Christopher Russell for their help with Aspen Plus simulations and for teaching me shortcuts and tricks as they discovered them. I appreciate Brandon Loong, Ammon Eaton, and Timo Groves for persevering through the many frustrations of building our experimental apparatus.

I would like to acknowledge the support and friendship from Sustainable Energy Solutions. Especially, I acknowledge Dr. David Frankman, Christopher Hoeger, Eric Mansfield, and Christopher Bence for their technical guidance.

TABLE OF CONTENTS

LIST OF TABLES

LIST OF FIGURES

NOMENCLATURE

Symbol	Property	Units
A	area	m^2
a	pure component parameter	$J\ m^3/mol^2$
b	volume parameter	m^3/mol
e_{sp}	specific energy	J/kg
f	temperature dependence of the pure component parameter a	unitless
F_i	area fraction of species i	unitless
k_{ij}	binary interaction parameter	unitless
N	number of species in a mixture	unitless
n_{comp}	number of components	unitless
n_{sub}	number of sub groups	unitless
P	pressure	Pa
P_c	critical pressure	Pa
P_i^{vap}	vapor pressure of species i	Pa
P_i^{sub}	solid vapor pressure of species i	Pa
Q	heat duty	W
Q_k	surface area parameter of functional subgroup k	unitless
q_i	surface area parameter for species i	unitless
R	universal gas constant	J/mol/K
R_k	Van der Waals volume parameter of functional subgroup k	unitless
r_i	volume parameter for species i	unitless
T	temperature	K
T_c	critical temperature	K
T_m	melting temperature	K
t_r	response time	min
U	heat transfer coefficient	$W/m^2/k$
v_{mix}	mixture volume	m^3/mol
V_i	volume fraction of species i	unitless
V_i'	modified volume fraction of species i	unitless
V_i^{liq}	liquid molar volume of species i	m^3/mol
V_i^{solid}	solid molar volume of species i	m^3/mol
V_m	molar volume	m^3/mol
x_i	condensed phase mole fraction of species i	unitless or %

Symbol	Property	Units
$X_{j,i}$	mole fraction of group *j* in a pure fluid of species *i* molecules	unitless
X_{M_i}	mole fraction of group *i* in mixture	unitless
y_i	vapor mole fraction of species *i*	unitless or %
z	coordination number	unitless
Z	compressibility	unitless
α	dimensionless quantity for PSRK EOS	unitless
$\bar{\alpha}_i$	dimensionless quantity for PSRK EOS	unitless
γ_{comb}	combinatorial term of activity coefficient	unitless
γ_{res}	residual term of activity coefficient	unitless
$\Gamma_{j,i}$	residual contribution to the activity coefficient of group j in a pure fluid of species i	unitless
Γ_{M_i}	residual contribution to the activity coefficient of group *i* in the mixture	unitless
Δc_p	change in heat capacity from liquid to solid	J/mol/K
Δh_m	heat of fusion at the melting temperature	J/mol
ΔT	correlation for temperature difference in heat exchanger	K
$\Delta u_{i,j}$	measure of interaction energy between groups *i* and *j*	unitless
η_{rt}	round trip efficiency	%
$\Theta_{j,i}$	surface area fraction of group j in a pure fluid of species i	unitless
Θ_{M_i}	surface area fraction of group i in mixture	unitless
$\nu_{j,i}$	number of j subgroups present in species i	unitless
ρ	mass or molar density	kg/m^3 or mol/m^3
ρ_e	energy density	J/m^3
σ	material strength	MPa
ϕ_i^{sub}	fugacity coefficient of pure species *i* at the sublimation pressure	unitless
$\bar{\phi}_i^{liq}$	liquid partial fugacity coefficient at total pressure	unitless
$\bar{\phi}_i^{vap}$	vapor partial fugacity coefficient at total pressure	unitless
ω	acentric factor	unitless

Subscript	Definition
e	electrical
th	thermal

NOMENCLATURE (Chemical Species)

Symbol	Chemical Species
Ar	argon
CH_4	methane
C_2H_6	ethane
C_3H_8	propane
CO_2	carbon dioxide
HC1	hydrocarbon 1
HC2	hydrocarbon 2
HC3	hydrocarbon 3
HCl	hydrogen chloride
H_2O	water
H_2S	hydrogen sulfide
Hg	mercury
MEA	monoethanolamine
N_2	nitrogen
NO	nitric oxide
NO_2	nitrogen dioxide
NO_x	nitrogen oxides
O_2	oxygen
SO_2	sulfur dioxide
SO_x	sulfur oxides

1 INTRODUCTION

The global energy industry has an established legacy of adaptation and mitigation of environmental concerns which continues now with CO_2 emissions. Global climate change presents one of the largest environmental concerns the industry has ever faced, partly because over 80 % of global energy comes from fuel combustion, with coal and natural gas combustion providing over 40 % and 20 % of electrical energy, respectively[1]. Both of these fuels produce electrical power primarily in large stationary sources and therefore represent both the largest point sources of CO_2 emission and the greatest opportunity for CO_2 emission mitigation. Another significant opportunity for CO_2 mitigation involves preparation of natural gas for pipeline transport or liquefaction. Several technologies can mitigate CO_2 emissions for these energy processes. Most of the remaining CO_2 emission comes from mobile sources or from small, distributed sources such as homes and commercial businesses. There are fewer options for CO_2 capture from these sources.

The most mature carbon capture technologies originate in CO_2 separation from natural gas as one part of natural gas processing. Raw natural gas often contains excess CO_2 that must be removed. The most common removal technology is amine-based absorption-desorption. This technology is well established for natural gas processing and LNG pretreatment and is now being adopted for flue gases. Flue gas applications differ significantly from the natural gas process since natural gas streams generally operate at much higher pressure, lower volumetric flow rate, and under reducing conditions compared to flue gases. Flue gas applications demonstrate the large

energy and economic costs of amine-based CO_2 capture. Energy and cost efficiency drive all energy processes. These figures of merit frame the discussion in this document for coal-fired power plants, natural gas processing, and LNG pretreatment with applications of cryogenic carbon capture to meet their needs. The first application is reducing CO_2 emissions from coal fired power plants, while providing an opportunity for energy storage. The second application is removing CO_2 in natural gas to meet pipeline standards in a less energy intensive manner. The third application is liquefying natural gas without CO_2 pretreatment for improving LNG yield.

The Environmental Protection Agency has established regulations to limit CO_2 emissions from future, non-peaking electricity generation stations to 1,100 lbs CO_2/MWh (500 kg CO_2/MWh)[2]. This limit slightly exceeds emissions of modern combined-cycle gas plants but is well below that of coal-fired plants. Even supercritical coal-fired power plants will require nearly 50 % CO_2 capture to meet these standards because their CO_2 emissions are in the range of 1,800-2,000 lbs CO_2/MWh (820-910 kg CO_2/MWh)[3]. Several technologies currently exist that can capture and thus reduce CO_2 emissions to meet regulations. However, while regulatory compliance is possible with current technologies, the associated energy penalty of CO_2 capture and resulting increased cost of electricity are substantial and pose significant changes to economies. Therefore, in pursuit of decreasing energy penalty and cost of CO_2 capture, External Cooling Loop Cryogenic Carbon Capture (CCC ECL) is outlined and simulated for incorporation into a full-scale, coal-fired power plant. In addition, an energy storage version is outlined for minor incremental cost, to facilitate synergy with intermittent power sources.

The legislative environment in over 60 countries encourages growth of renewable energy sources as a fraction of total power production. While increasing incentives and targets for renewable energy production, most of these same countries have targets for reducing emissions

making it more difficult for new coal-fired power plants to be permitted[4]. As of 2011, global wind energy capacity was 237 GW with nearly half of that figure being added between 2009 and 2011[5]. Global photovoltaic (PV) solar capacity as of 2011, according to the International Energy Agency (IEA), is at 40 GW with an annual growth rate of 40 % since 2009[6]. Current renewable energy production is intermittent and geographically limited. Because most renewable energy sources are intermittent and change rapidly and largely unpredictably in time, they reduce the usable life of and cause inefficiencies in base load generation facilities, such as coal fired power plants. The significance of rapidly responding energy storage becomes crucial to maintaining a reliable electric grid as renewable energy sources gain a larger portion of the energy market.

Sustainable Energy Solutions (SES) proposes an integrated Energy-Storing Cryogenic CO_2 Capture (CCC ES) system suitable for any stationary CO_2 source, especially coal-fired power plants. The system matches ramping of renewable energy, stores energy for smoothing base-load energy production, and removes CO_2 emissions from the base-load energy production. Capturing CO_2 consumes approximately 12-18 % of the base-load energy production for CO_2 capture[7], with energy storage efficiencies of greater than 90 % roundtrip (energy into system vs energy output)[8], and it significantly improves the energy efficiency and stability of the electric grid. The CCC ES process stores energy efficiently and changes load rapidly over a significant fraction of a power plant capacity. The energy storage option can reduce peak load parasitic losses by shifting loads to non-peak or cheaper generation times. The rapid load change capability provides major grid management capabilities that are essential to accommodate intermittent supplies, such as renewable wind and solar energy.

There is an increasing need for processing of natural gas to meet composition standards and separate high-value products, such as natural gas liquids, with increasing natural gas

production both domestically and globally. Typical pipeline specifications limit CO_2 to 2-4 %, with CO_2 concentration in some fields starting as high as 70 %. Removal of CO_2 in natural gas is an industry driven practice rather than regulation driven, providing an opportunity for more immediate adoption of promising new technologies. In a similar manner to removing CO_2 from flue gas, natural gas processing by cryogenic carbon capture (CCC NG) is outlined to present a less energy intensive method for meeting CO_2 pipeline specifications.

Electricity production from natural gas is a rapidly growing industry. In order to transport natural gas from sources to users, pipelines are generally used. However, for global trade and as new gas fields are developed, pipelines are either not present or insufficient to transport natural gas. Therefore, natural gas liquefaction is a growing industry with natural gas being pretreated to remove CO_2 down to 50 ppm in order to prevent freeze out in conventional heat exchangers. Natural Gas Liquefaction by CCC (CCC LNG) is outlined to replace conventional pretreatment and liquefaction with a simple CO_2 tolerant liquefaction system with CO_2 being removed as a solid from the LNG. In the event of industry reluctance to deal with LNG saturated with CO_2, another process is outlined to remove CO_2 at low pressures to achieve the conventional 50 ppm CO_2 specification.

This dissertation presents the feasibility of CCC ES, which includes detailed energy and financial analyses along with lab demonstrations of critical process unit operation. The specific hypotheses being tested are that (1) CO_2 capture performance of CCC processes can be adequately predicted, (2) the energy and economic cost of baseline CCC ES are more competitive than current technologies. To test these hypotheses, the work plan included four tasks (1) process simulations, (2) energy analysis, (3) economic evaluation, and (4) lab scale demonstrations of CCC ES, CCC NG, and CCC LNG. Aspen Plus simulation software codes will be used to simulate and optimize

CCC ES as a process and as individual unit operations. Stand-alone or integrated codes will be authored to reconcile simulation results from Aspen Plus. Economic evaluations will be completed following DOE guidelines for levelized cost. An apparatus for process demonstration will be custom designed and manufactured.

The remainder of this dissertation begins with a background section reviewing options for CO_2 capture, grid-scale energy storage, natural gas processing, and natural gas liquefaction. Following the background section, cryogenic carbon capture is discussed in general terms, as applicable for the applications later discussed. Methods of CO_2 capture prediction are presented with validation from closely related data available in the literature. The experimental apparatuses are explained that are used for demonstration of CCC processes. With that framework set, each of the CCC applications are discussed in detail with experimental results. This dissertation concludes with final conclusions summarizing the important principles of this research.

2 BACKGROUND

Coal is a relatively cheap and extremely abundant energy resource that will play a significantly increasing role in the world energy future. Coal-fired power plants currently provide 19 % of total energy, yet account for 28 % of the global CO_2 emissions[9], far more than most alternative power production methods. Natural gas is considered by most to be the most widely accepted alternative to coal and emits roughly half of the CO_2 per energy produced compared to coal[10]. Carbon capture technologies are discussed along with energy storage options for grid-scale electricity production. Following that discussion, more specific natural gas processing and natural gas liquefaction technologies are explored.

2.1 Carbon Capture for Power Plants

Several methods for CO_2 capture are available. Many CO_2 separation technologies target different industries including energy production, cement production, aluminum and steel manufacturing, and natural gas production. The literature reviews current technologies for these industries[11-14]. These technologies for coal-fired power plants fall into the categories of oxy-combustion, chemical looping, absorbents, adsorbents, membranes, and cryogenic processes. All have parasitic loads, consuming a significant fraction of the power produced, and thus reduce the net power plant output. The energy penalties vary among the technologies, and Table 2-1 shows a general sense of their current performance. Energy penalties for chemical looping are absent from

Table 2-1 because chemical looping is generally only applied to high-pressure combustion systems where it takes advantage of the high pressure to be more competitive. Energy penalties are reported in units of MJ_e/kg CO_2 rather than MJ_{th}/kg CO_2 to account for the extra coal consumed to operate the carbon capture.

Table 2-1 Summary of energy penalties by technology

Process	Mean (MJ_e/kg CO_2)	Median (MJ_e/kg CO_2)	Low (MJ_e/kg CO_2)	High (MJ_e/kg CO_2)	References
Oxy-combustion	1.69	1.53	1.51	2.02	[15, 16]
Chemical Looping	-	-	-	-	
Absorbents	1.72	1.38	0.97	4.20	[17-26]
Adsorbents	3.39	2.55	2.02	5.60	[17, 27]
Membranes	1.30	1.29	0.95	1.90	[28, 29]
Cryogenics	0.98	1.03	0.74	1.18	this study,[30, 31]

2.1.1 Oxy-combustion

This method of CO_2 management uses a pre-combustion air separation unit (ASU). Oxygen is cryogenically distilled from air to combust with coal, resulting in nominally pure combustion products, CO_2 and H_2O. The resulting flue gas cools, condensing out H_2O, and then nominally pure CO_2 is pressurized and sequestered or used for enhanced oil recovery. At least two full-scale power plants are planned to be built with this technology in the near future, White Rose (UK) and FutureGen 2.0 (USA). Hurdles for widespread adoption of oxy-combustion include its high energy penalty due to the extreme, low temperatures (~73 K) required for cryogenic distillation of O_2 from air[32]. The resulting energy penalty is in the range of 1.5-2.0 MJ_e/kg CO_2 captured. There is little expectation for reducing the energy penalty due to the constraints in the air separation unit with similar molecular weights and vapor pressures of N_2 and O_2. The second disadvantage is the

essential plant rebuild required for existing plants since it changes everything downstream of the ASU.

2.1.2 Chemical Looping

Chemical looping poses a similar approach to CO_2 management, but oxygen is introduced as part of an oxidized metal, such as iron titanium oxide[33], instead of as a gas. Oxygen, typically from air, binds to the solid metal carrier in a fluidized bed, and then the oxidized solid metal is transported to a second fluidized bed where combustion occurs. The solid metal returns to the first fluidized bed to be oxidized[34]. The combustion products are handled similarly to those of oxy-combustion with the same back end processing. Some of the most significant concerns with chemical looping include the effects of thermally cycling the oxidizing metal carrier. Deactivation with use and entropy losses due to heating and cooling of the solid particles significantly affect the energy penalty. However, chemical looping benefits from the combustion process operating at high pressures. If chemical looping were to be applied to the near atmospheric combustion of this study's base power plant, the energy penalties would significantly increase. Disregarding the energy for final compression, the energy penalty range is 0.2-0.5 MJ_e/kg CO_2 captured when applied to high pressure combustion systems[35, 36]. Currently, research and development is being performed at the National Carbon Capture Center on a 150 kW_e equivalent system[37]. A summary of several other systems of various chemical looping projects is available from NETL[38]. Because most of the power plant must be replaced to implement chemical looping on an existing facility, chemical looping is generally not considered as a retrofit option.

2.1.3 Absorbents

Amine scrubbing processes are by far the most widely used form of CO_2 removal technology and have been researched for decades[17]. They are commercially available for multiple

applications. However, power-plant scale and reliability requirements significantly exceed those of commercial absorption processes. Amine sorbents bind to the CO_2, removing it from the process stream. The data from Table 2-1 show a large variation in energy penalties despite similar sorbent composition. They range from 0.72-4.20 MJ_e/kg CO_2 depending on the power plant and the design of the system. Generally, NETL has considered an amine carbon capture system to have an associated energy penalty of 1.3 MJ_e/kg CO_2 captured[39]. Variations on compressors, pressures, percent sorbent, and the sorbent composition used are all major contributors to the energy penalties experienced by these processes[22]. A major benefit of this system is that it is a very mature system[17]. It is also commercially available for power plants, although many absorbents are not past the pilot scale. Currently, a Selexol process is being commissioned for the full-scale Kemper power plant (USA). The drawbacks include the size of the process as well as the toxicity of the chemicals and the energy cost to the system. Other, less commonly used, amine sorbents include a mixture of primary, secondary, and tertiary amines. These sorbents have similar energy penalties to more traditional MEA sorbents.

The primary disadvantages of chemical absorption are: (1) the significant energy required to operate the scrubbing system, (2) the amount, toxicity, and instability and atmospheric reactivity of the solvent, (3) the cost, and (4) the incompatibility with traditional power plant operations in terms of load following, operation, and design. The principal energy demands are reboiling and steam generation, with secondary demands of electrical power[40].

Other types of sorbents, such as Opticap by B & W, have many drawbacks similar to those mentioned for amines, but additionally have far less research supporting them and are not as commercially available. They are, however, sometimes more efficient as shown by a comparison

conducted at NCCC, where Opticap proved significantly more efficient under similar circumstances as MEA to remove CO_2[21].

2.1.4 Adsorbents

Due to the physical attraction between CO_2 and other species, adsorbents are used for CO_2 capture. Typical CO_2 adsorbents include zeolites, molecular sieves, and activated carbon which preferentially adsorb the CO_2 from air fired combustion products. Once the adsorbent is saturated with CO_2, it generally regenerates with a pressure and/or temperature swing. The energy penalty of adsorbents depends primarily on the energy required for the cyclical change in conditions and are in the range of 2.0-5.6 MJ_e/kg CO_2 captured[17, 27].

2.1.5 Membranes

Membranes are used in the carbon capture process as an effective alternative to chemicals. Membranes are generally employed post-combustion, separating CO_2 from the flue gas at typical exhaust conditions by allowing CO_2 to penetrate the membrane faster than other species, specifically N_2. The membranes are commonly made from polymers[41]. The membrane selectively separates components in the stream, specifically the CO_2 molecules. Testing of membranes has only been conducted on very small scales compared to amine processes. The distinct advantage they have is the absence of toxic chemicals. Membrane separation requires replacement membranes[42] as well as significant pumping power[43], the latter resulting in energy penalties within the range of 0.95-1.9 MJ_e/kg CO_2 captured[28, 29], while still having the difficulty of producing high purity CO_2.

2.1.6 Cryogenic Processes

Cryogenic technologies come in several forms, including the thermal swing process, inertial carbon extraction system, and the CCC ECL. A thermal swing process freezes out CO_2 as a solid directly onto the surface of a heat exchanger. The heat transfer degrades with time as solid CO_2 fouls the surface. At some point, a second parallel heat exchanger begins processing the stream while the first warms and regenerates[44]. In the case of 90 % CO_2 capture from a coal-fired power plant, Pan et al. report that the process energy penalty is 1.18 MJ_e/kg CO_2[30]. Significant energy losses incur with the temperature swing of the heat exchanger. In addition, heat transfer rates reduce as CO_2 solids form on the heat exchanger surfaces. Mechanical cleaning has been proposed for handling the solids formation and keeping heat exchange surfaces clean. While Alstom has generally been interested in this basic process, Shell has also investigated similar processes and shown good agreement between predictions and experimentation[45]. Alstom has slowed the development of the thermal swing process because of minor energy penalty improvements and major capital costs compared with conventional amine systems.

Inertial Carbon Extraction System, an expansion process, forms solid CO_2 without any of the surface fouling issues[46]. Flue gas is expanded through a nozzle, and solid CO_2 particles form with the heat transfer coming from expansion rather than a surface. A cyclone separates the gas/solid stream. The design, operation, and maturity of this process are significant obstacles to commercialization.

Cryogenic carbon capture is a more advantageous process from energy and cost perspectives, yet has significant technical hurdles to be resolved before the technology can be demonstrated in a commercial setting. The advantages of superior energy efficiency stem from (1) the more moderate cryogenic temperatures compared to air separation required for CO_2

desublimation from flue gas and (2) the ease of liquid/solid separation compared with vapor/liquid separation of the other competing CO_2 removal systems. Additionally, cryogenic carbon capture pressurizes the CO_2 when it is in a condensed phase, not as a gas. Solid/liquid pressurization requires far less energy than gaseous compression. Another advantage is the ability to also separate H_2O, SO_x, NO_2, HCl, and Hg from the flue gas[47, 48]. Although, cryogenic carbon capture remains a relatively young technology, it is being actively developed by multiple groups[31, 49-51].

2.2 Grid-Scale Energy Storage

Grid-scale energy storage systems support a diversified portfolio of electricity production. There exists a large and growing global and regional demand for grid-scale systems to support frequency regulation, peak shaving, and load leveling. The importance of energy storage systems will increase disproportionately with time because of growing energy demand, increasing consequences of grid failures associated with increasing economic reliance on electricity, and increased development of intermittent power sources. Many technologies serve energy storage needs, and it is reasonable to expect that new energy storage technologies will be developed in the near future to meet increasing needs.

Global energy production and consumption demand is increasing rapidly, in part because of increasing world population. New estimates show that global population will reach 8-11 billion people by 2050. The United Nations projects that a majority of this expansion will occur in under-developed and developing countries, which have growing energy demands, specifically electricity[52]. In addition to increasing population, recently improved economic conditions for much of the world's population bring an associated increase in energy demand of all types, including electricity. Since 1981, the global population living in abject poverty has decreased by over 700 million people and from over 50 % to about 20 % of the world population[53], with about half of the

change occurring since 2000. This exceeds the current population of every country except China and India by more than a factor of two. To sustain this impressive economic improvement will require dramatic increases in energy availability and reliability, for which energy storage is an essential component, even if global population were not increasing. According to the U.S. Energy Information Administration (EIA), global electricity demand will increase by 2.3 % annually from 2008 to 2035. This will result in a near doubling of current global electrical energy consumption from 19,110 TWh in 2008 to 35,230 TWh in 2035[54]. This will also stretch the capability of power generators and transmissions systems well beyond current capacities.

Emerging economies such as China, Brazil, Indonesia, India, and Russia will continue to see increased electricity demand from their escalating middle class populations. According to the International Energy Agency (IEA), Organization for Economic Co-operation and Development (OECD) countries accounted for 73.1 % of the 6,115 TWh of electricity generated in 1973. In 2010, OECD countries accounted for 50.7 % of the 21,431 TWh of global electricity generation[55]. These snapshots of consumer energy demand highlight that both developed and developing economies' energy demands will likely increase in the future, with disproportionate increases occurring in developing economies.

The projected increase in global electricity demand requires more and better base load and peaking power sources and expanded capacity to meet demand and for frequency regulation and load leveling. Environmental, economic, and reliability challenges associated with meeting this demand are formidable. Much focus in future utility development, regulation, and management will be devoted to securing an inexpensive, consistent power supply. Governments, corporations, and other organizations will struggle to meet future needs without innovative technologies and practices.

A failure to provide necessary power has both social and economic effects. For example, the two-day blackouts across India in July 2012 highlight the potential problems that can arise from inadequate power capacity. Such disruptions affected nearly every aspect of life. Hospitals, wastewater treatment plants, traffic lights, trains, businesses, and residential appliances including refrigeration and temperature control systems were unable to operate over the course of two days. Traffic jams, stranded passengers, and general confusion led to protest and civil unrest[56]. Similar blackouts, affecting fewer people, have occurred in most regions, including a two-day event in the US and Canada in August 2003. The costs of unreliable electrical power to the US alone have been estimated at $80 billion annually, with wide range of uncertainty[57]. These events illustrate problems that arise with inadequate or unreliable electrical power.

Electricity supply management requires new power plant construction. As part of this strategy, energy storage enhances reliability and mitigates unanticipated disruptions while significantly increasing effective capacity. Energy storage must be able to handle both predictable and unpredictable changes in energy demand. Enhancing grid utility, communication, and especially reliability often goes by the moniker smart grid. It is only a slight overstatement that any grid can be made smart with appropriate energy storage technologies while no grid can be made truly smart without it.

Renewable electricity generation draws power from natural energy sources, primarily the wind and the sun. Harnessing these natural sources of energy provides great promise for an environmentally clean energy source. Renewable energy intermittency represents a significant challenge to its most effective use. This challenge increases with increased fraction of intermittent power. In one investigation, electric power generation in the southwestern United States varied month to month and year to year. Over the period of 2004-2006, total energy generation varied

from 5,000 GWh to almost 12,000 GWh during 2004 through 2006[58]. However, the most challenging aspects of intermittent energy are the hour-by hour or minute-by-minute variations in output. Effective energy storage can transform the intermittent energy production rates to more closely match the energy demand rates, thereby greatly increasing the value of the intermittent sources.

Electrical power demand exhibits 24-hour cycles typically with greater demand occurring during the day, especially the afternoon and evening, less demand during the late night and early morning. Typical demand fluctuations appear in Figure 2-1 and can be as high as 8 % per minute. Conventional electricity generating sources such as coal-fired, natural-gas-combined-cycle, and nuclear power plants provide reliable and generally cost effective base-load power generation. These power generating systems work well at meeting the evolving baseline demand. However, they respond slowly to changes in demand. Large turn-down ratios decrease their efficiency and rapid or even modest load-change rates shorten the lifetime of critical boiler components, most notably heat exchangers (super heaters and steam generators) and in some cases steam turbine blades. Peaking power plants typically supply the incremental power for peak demand, the most typical of which is a simple-cycle gas turbine. The simple-cycle turbine produces power less efficiently than the combined-cycle system, but it can respond to load changes rapidly. It also is less capital intensive than the base-load plants and therefore less expensive to idle during low demand. Commonly, the capacity factor for peaking plants is in the 25-35 % range while that for the base-load plants exceeds 80 %[59]. The combination of low capacity factor, low efficiency, and sometimes relatively small scale of peaking plants usually increases the incremental cost of power during peak demand, frequently by factors of 2-6. Some of the same factors increase the CO_2 intensity of peak power, though this increase is usually less dramatic.

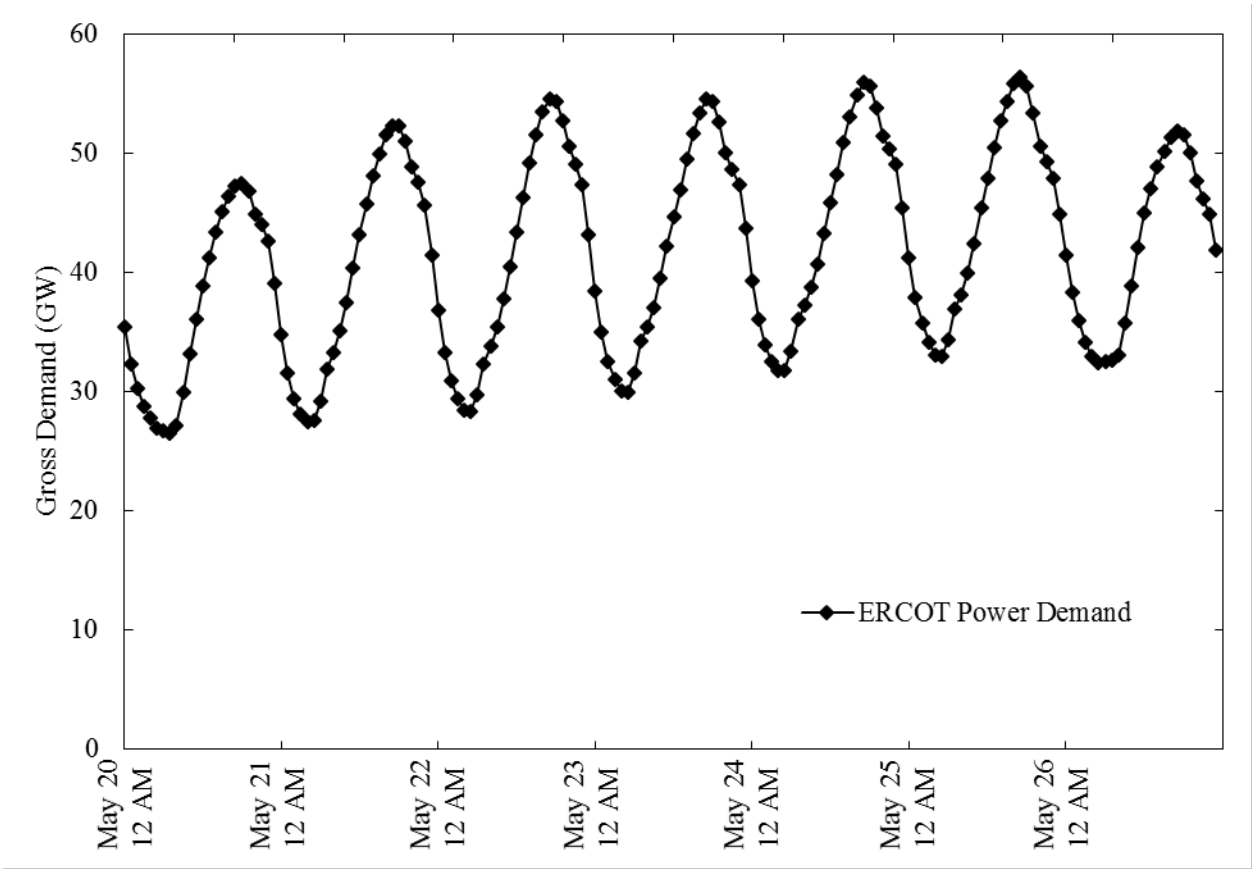

Figure 2-1 Energy demand for Electric Reliability Council of Texas (ERCOT) from Sunday May 20, 2012 to Saturday May 26, 2012

Energy storage systems could meet fluctuating demand by storing energy during times of low demand and releasing energy during times of high demand. Many energy storage technologies complement traditional base-load power generating stations by providing fast response time and additional generative capacity during peak demand times. Although all energy storage systems lose some energy (otherwise they would be generation systems, not storage systems), the economics and overall efficiency drops associated with peak power generation can offset the cost of the storage system and its inefficiencies.

Increasing use of intermittent energy supplies such as wind and solar escalate the need for energy storage exponentially. Historically, grid-scale energy storage started with pumped hydroelectric systems and grew rapidly through the late 1900's as seen in Figure 2-2. Pumped storage accounts for 98.2 % of all grid-scale energy storage as of 2013. Pumped storage seems to follow an s-curve with the rate of new installations declining. This decline coincides with a rise in contributions from several alternative technologies for grid-scale energy storage: compressed air, molten salt, liquid air, and several varieties of batteries. Interestingly, the molten salt thermal storage and two compressed-air energy storage systems account for 71.2 % and 22.6 % of all non-pumped-storage systems.

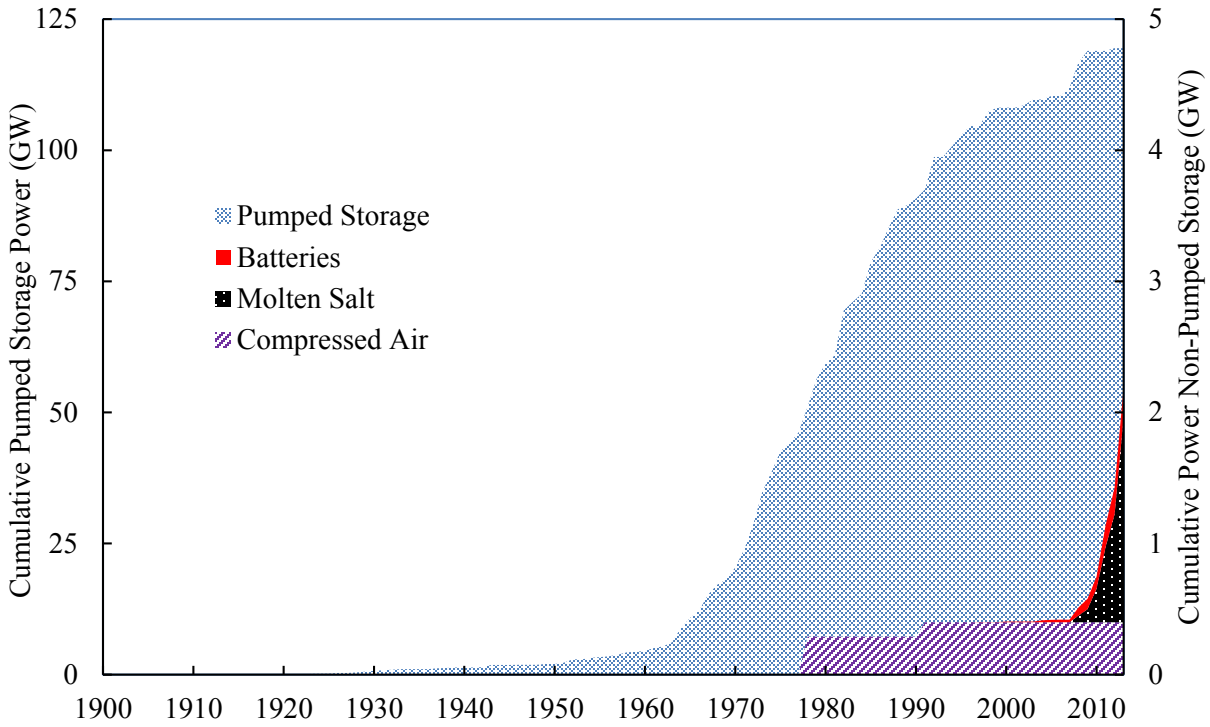

Figure 2-2 Global cumulative power of grid-scale energy storage systems.

Pumped storage systems are generally built with new hydropower installations, and the U.S. Energy Information Agency expects virtually no domestic growth of hydropower installations from 2013-2040[60]. While the outlook for pumped storage appears weak in the US, other countries may become important in continuing the growth of the historically dominant energy storage technology. Pumped storage has the appeal of large installations (> 1 GW) and high efficiencies (> 75 %), see Table 2-2.

Table 2-2 Operating data from the ten largest pumped storage plants in the United States[61]

Plant Name	State	Power (GW)	Energy (GWd)	Avg. Head (m)	Eff. (%)
Bath County	VA	3.00	0.99	359	80
Ludington	MI	1.87	0.72	111	72
Raccoon Mountain	TN	1.65	1.31	273	79
Castaic	CA	1.28	0.50	326	67
Bad Creek	SC	1.07	1.00	350	82
Helms Pumped Storage	CA	1.21	7.67	490	74
Blenheim Gilboa	NY	1.16	0.50	335	75
Northfield Mountain	MA	1.08	0.44	227	75
Rocky Mountain Hydro	GA	1.05	0.24	197	84
Muddy Run	PA	1.07	0.46	108	71

With global energy consumption expected to double by 2040 and the weak outlook for pumped storage, energy storage needs will be met in part with developing and new energy storage technologies and with increased responsiveness of electricity production. If pumped hydro is constrained at its current level and energy storage needs are indeed doubled by 2040, it would result in every other energy storage option increasing at 16 % annually. While this growth of energy storage may seem manageable, it is compounded by increasing non-dispatchable renewable

energy production. In particular, wind energy is expected to grow 9.80 % annually to 2040[62] with most wind energy installations directly requiring an energy storage system.

In evaluating any energy storage system, it is important to determine appropriateness based on key metrics: efficiency, cost, response, size, and other limiting factors. For example, a NaS battery system is currently the most commercially viable battery system, and costs are anticipated to decrease with increased installation size[63]. The best battery systems may qualify with excellent response, efficiency, and no geographical restrictions, but have an undesirable high cost per unit of power ($/kW) compared to pumped hydroelectric systems. In Table 2-3, energy storage options with potential grid-scale deployment are compared across several key decision factors, including round trip storage efficiency (energy into system vs energy output), capital cost per unit of power, largest single site installations, and primary barriers or considerations for implementing the technology with new installations. Data are taken from existing installations, with estimates noted.

Table 2-3 Grid-scale energy storage technology summary[64-72]

	Technology	Eff. (%)	Cap Cost ($/kW)	Largest Inst. (MW)	Primary Barrier
Mechanical	Pumped Hydro	65-85	200-600	3,000	Geography
	Compressed Air	56-75	400-464	300	Geography
	Flywheel	81	1,500	20 [A]	Materials
Electro-Chemical	Pb Acid	90	1,200-2,300	90	Cycling/Lifetime
	Flow Batteries	75-85	1,900-2,500	25 [B]	Cycling/Lifetime
	NaS Battery	45-89	6,000	34 [A]	Cycling, Heat Control
Thermal	Molten Salt	95-99.9	7,250-9,000	360	Geography
	Liquid Air	35-70	Est. 900-1,900	5 [A]	Combined Heating
	CCC ES	99	< 100	- [B]	CO_2 Capture

Expectation of future largest installations to be on order of [A]100 MW or [B]1,000 MW

Whatever the growth rate may become, energy storage technology development will undoubtedly continue to support a rapidly growing industry. Energy storage system growth will not only support current energy storage technologies, but will also create an environment for new technology research and creation. However, for any new system to have a significant scale impact, it must be able to favorably compete with pumped storage.

2.3 Natural Gas Processing

Globally, natural gas is an important source of energy and is becoming increasingly transportable through expanding pipelines and by liquefaction. However, raw natural gas compositions, energy content, and producibility differ greatly. Standards for natural gas pipelines constrain the composition that is allowable for transport and most raw natural gas requires processing prior to putting it into natural gas pipelines. Conventional natural gas processing involves separating H_2S, CO_2, and natural gas liquids and generally include amine-based solvents in absorption and stripping columns for CO_2 separation[73]. These technologies consume energy, present safety problems, and represent operational and siting challenges for natural gas with high initial CO_2 concentrations. Generally, energy demands of existing technologies scale with the CO_2 flow rather than the natural gas flow.

Uses of natural gas are composition sensitive. Some components, such as condensable hydrocarbons, go by the term natural gas liquids and represent high-value feedstock for the petrochemical industry. Losses on selling the natural gas are often offset by profitability of the recovered natural gas liquids. Typical pipeline and liquefaction process natural gas compositions for the US market appear in Table 2-4.

Table 2-4 Typical natural gas pipeline and liquefaction process compositions[74, 75]

Component	Pipeline Composition	Liquefaction Composition
Methane	> 75 %	> 97 %
Ethane	< 10 %	< 1 %
Other Hydrocarbons	< 7.5 %	< 3 %
Nitrogen & Inerts	< 3-4 %	< 2 %
Carbon Dioxide	< 2-4 %	< 50 ppm
Sulfur	< 0.05-0.20 g/scf	< 14 ppm
Water	< 7 lbs/mmcf	trace

Many CO_2 separation technologies have been developed and targeted for different industries including energy production, cement production, aluminum and steel manufacturing, and natural gas production. The literature reviews the current technologies for these industries[11-14]. These processing technologies fall into the categories of adsorption, absorption, membranes, and cryogenic processes. Reviews of natural gas-CO_2 separation technologies are readily available[12, 13, 76]. Due to the variation of natural gas compositions, many technologies exist with niche applications and differing maturity. This discussion centers on the current state of cryogenic processes with CO_2 phase separation, as these technologies are the most similar to the CCC NG process described later in this document. Gas-liquid separation occurs with operating temperatures above the CO_2 triple point temperature of 216.55 K[77] or within the limits of CO_2 solubility. These gas-liquid separation technologies include C3sep and the Ryan-Holmes process. Other technologies involve solids formation, including the thermal swing process, CryoCell, and Controlled Freeze Zone.

2.3.1 *Cryogenic Distillation*

Many groups have studied cryogenic distillation for removal of CO_2 and this technology is part of many separation processes. The high energy cost of distillation stems from the cooling required, which in the case of cryogenics involves compression and expansion, either of the natural gas directly or in a closed refrigeration system. Gillespie explored the energetics and economics of cryogenic distillation and found that it makes sense with natural gas streams rich in liquids[78]. Berstad et al. reports an energy penalty of 1.9 MJ_e/kg CO_2 for removing CO_2 to an LNG specification of 50 ppm starting with 50.6 % CO_2 (crediting for C_3 and C_4 recovery with 59 % efficiency for thermal to electric conversion)[79]. However, the cryogenic distillation process has minor incremental costs for separating high-value natural gas liquids and becomes economical in many instances when there is potential natural gas liquids recovery.

2.3.2 *C3sep Process*

The C3sep technology uses expansion cooling to form CO_2-rich liquid droplets that can be separated with a rotating particle separator. Typically, residence times of 100 s would be necessary for droplets to reach a size of 20 μm. However, the rotating particle separator is able to separate particles of a few microns, decreasing the necessary droplet growth time to less than 1 s[80]. While this technology provides a great liquid/gas separation, the product gas must still undergo secondary treatment to achieve pipeline standards of CO_2 removal[81]. Therefore, this technology is not a standalone solution and must be combined with other technologies to adequately process natural gas.

2.3.3 *Ryan-Holmes Process*

The Ryan-Holmes process uses the addition of another component to increase the solubility of CO_2 in the non-methane components of the natural gas stream[82]. While this can provide stand-

alone separation capabilities adequate for pipeline specifications, it loads the natural gas liquids, used to increase solubility, with CO_2. The original CO_2 uniformly distributed in the natural gas and liquids is now concentrated in the natural gas liquids. With natural gas liquids being the more valued fraction of natural gas production, it is difficult to justify economically, since another separation technology, typically cryogenic distillation[83], must still be employed to reduce CO_2 in the natural gas liquids. However, the process exploits an important concept of CO_2 solubility and the potential for cryogenic processing without solid formation that can be seen in other technologies.

2.3.4 Thermal Swing

The thermal swing process freezes CO_2 as a solid directly onto the surface of a heat exchanger. The heat transfer degrades with time as solid CO_2 fouls the surface. At some point, a second parallel heat exchanger begins processing the stream while the first warms and regenerates[44]. While Alstom has generally explored this process, Shell has also investigated the process and shown good agreement between predictions and experimentation[45]. Alstom has slowed the development of the thermal swing process because of only minor energy penalty improvements and major capital costs compared with conventional amine systems.

2.3.5 CryoCell

The CryoCell technology uses Joule-Thomson expansion into a process vessel to cool natural gas to form solid CO_2 particles[84]. CO_2-lean gas flows from the top of the tank. Taking a concept from the Ryan-Holmes process of increasing the solubility, a stream of ethane can transform CO_2 from a solid to a liquid at the bottom of the vessel[85, 86]. Thus solid CO_2 is only present in the CryoCell process in one unit operation with no moving parts. Another application of the CryoCell process removes the solid from the process vessel without first liquefying but

requires moving parts[87]. Because the cooling occurs through expansion, the end product natural gas must be recompressed to transport pressures. Tests have successfully demonstrated removal of CO_2 down to as low as 3 % CO_2 from natural gas streams containing 13-60 %[88]. The CryoCell technology has slowed in its development for natural gas processing applications, but has seen recent interest in other applications[89].

2.3.6 Controlled Freeze Zone

The Controlled Freeze Zone (CFZ) involves a pressurized distillation column with a central region in which CO_2 solidifies[90, 91]. This cryogenic separation process removes CO_2 from raw natural gas in a process that controls CO_2 freezing within the distillation tower. In addition to CO_2 removal, H_2S is also removed during the process[92]. One downside to the CFZ process is that C_2H_6 and CO_2 can form an azeotrope and liquefy at similar conditions. This results in the disposal of valuable ethane with the CO_2 product[93]. ExxonMobil's Shute Creek Treating Facility near LaBarge, Wyoming demonstrates CFZ feasibility by achieving CO_2-rich streams with less than 0.5 % methane and methane-rich streams with as little as 100 ppm CO_2[93]. Exxon expects that the CFZ is particularly applicable to natural gas streams with high CO_2 and H_2S concentrations that are normally considered uneconomical[94].

2.4 Natural Gas Liquefaction

LNG quality requirements are 2 and 2.5 % CO_2 in Canada and the EU, respectively[95]. The US does not currently have LNG quality requirements, but re-vaporized LNG must meet natural gas pipeline standards of 2-4 % CO_2[96]. Even with these standards, natural gas is pretreated for CO_2 removal down to 50 ppm before liquefaction in practice. The reason for CO_2 removal down to 50 ppm stems from concerns with degradation of operability due to potential CO_2 freezing during natural gas liquefaction. The solubility of CO_2 in the final LNG product at normal conditions is

higher than 50 ppm[97]. Thus it is important to consider CCC LNG applied to the practice of achieving 50 ppm CO_2 and the potential for CO_2 tolerant liquefaction. Many CO_2 removal technologies exist and may be used as a pretreatment to reduce CO_2[11-13]. The technologies most similar to CCC LNG that focus on solid phase formation of CO_2 are thermal swing, CryoCell, and Controlled Freeze Zone (CFZ). These technologies have been previously described in terms of natural gas processing for removing CO_2 to meet pipeline standards. In the application of these same technologies to natural gas liquefaction, colder temperatures along with a few process variations must be considered.

While the thermal swing process is generally envisioned for CO_2 solids forming from the vapor phase, this can also be applied to natural gas liquefaction. In this case, both the vapor and liquid phases will form solid CO_2 as they cool, but should not prove much more difficult that the natural gas processing application.

CryoCell technology can be applied as a pretreatment with re-pressurization for high-pressure liquefaction or as part of the cooling process with low-pressure liquefaction. If integrated into the cooling process, colder temperatures must be reached after the CryoCell for liquefaction of the natural gas because of the natural gas' lower pressure. The colder liquefaction temperature is significantly more energy intensive.

As previously mentioned, the Controlled Freeze Zone (CFZ) by ExxonMobil has been demonstrated with CO_2 removal down to 100 ppm in the methane-rich stream[93]. The natural gas product stream would still need to be liquefied, but of the available cryogenic processes, CFZ is the most commercialized. For this technology, Berstad et al. reports an energy penalty of 1.9 $MJ_e/kg\ CO_2$ for removing CO_2 down to a LNG specification of 50 ppm for a particular starting

composition with 50.6 % CO_2 (crediting for C_3 an C_4 recovery with 59 % efficiency for thermal to electric conversion)[79].

While conventional pretreatments in some instances may have a low energetic and/or economic cost, cryogenic treatment's primary energy cost are marginal since the natural gas must be cooled for liquefaction regardless. Similar to the CFZ process, CCC LNG embraces the solid formation of CO_2, but uses low energy methods of solid/liquid separation for bulk CO_2 removal. Two variations of CCC LNG are later presented with distinctions made by operating pressure. In the low-pressure regime, 50 ppm separation can be achieved while the natural gas remains in the vapor phase. Therefore, the CCC LNG would replace the pretreatment with a desublimating heat exchanger and filtration system that cools the natural gas from its compositionally dependent frost point to the temperature necessary for 50 ppm CO_2 while removing all the solids formed. In the high-pressure regime, the pretreatment plant is made unnecessary by replacing the natural gas liquefaction heat exchanger with a desublimating heat exchanger and filtration system. In this regime, 50 ppm CO_2 is not achieved, and the CO_2 removal is dictated by the solubility of CO_2 in the LNG. While LNG with 50+ ppm may not be feasible for commercial application in some instances, there are many cases where natural gas is liquefied and vaporized to serve natural gas distribution in pipelines during demand swings. In these cases, high-pressure CCC LNG with 50+ ppm CO_2 can avoid the requirements of CO_2 specifications. In all cases, the high-pressure system can achieve 50 ppm or lower by dropping the pressure and operating in a low-pressure mode.

3 CRYOGENIC CARBON CAPTURE (CCC)

Cryogenic carbon capture was first invented and patented by Dr. Larry L. Baxter, Professor at Brigham Young University[98]. Cryogenic carbon capture is a post-combustion technology that causes CO_2 to desublimate from the process stream thru refrigeration and/or expansion, see Figure 3-1. Desublimation presents a significant energy advantage over other separation technologies in that the CO_2 phase that forms is essentially pure, unlike a liquid CO_2 solution which must be distilled or stripped[51]. The parasitic energy load of 90 % carbon capture, which is effectively consumed in operating the compression and/or refrigeration cycle(s), is approximately 18 % of the power produced by the coal combustion facility. In terms of natural gas processing, the process variables change significantly enough that it is difficult to characterize the parasitic load.

3.1 Solids Formation

The key to successful cryogenic carbon capture is continuous formation of CO_2 solids without fouling. The primary methods of heat exchange in the CCC desublimating heat exchangers are expansion cooling, indirect contact heat exchange, and direct contact heat exchange.

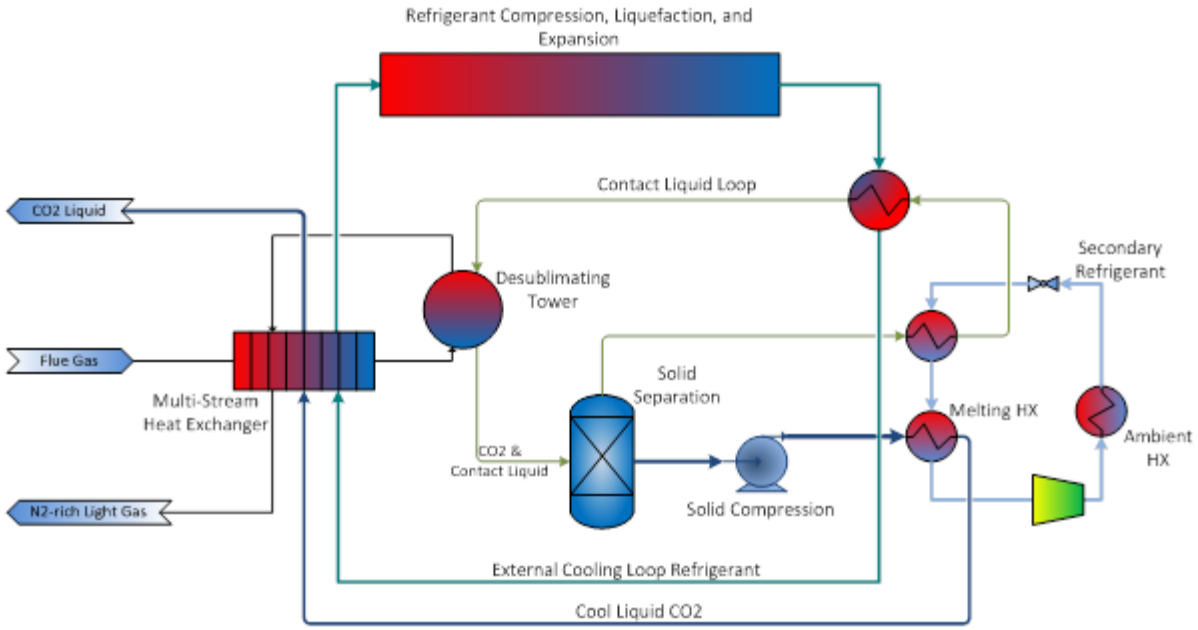

Figure 3-1 Simple schematic of external, cooling-loop cryogenic carbon capture (CCC ECL)

3.1.1 Desublimation by Expansion Cooling

Both an expansion valve and turbine can be used to provide the pressure drop for cooling needed to cause CO_2 desublimation. The turbine reaches colder temperatures more efficiently than indirect heat transfer processes. To offset the pressure loss due to expansion, the process stream must be compressed. This process is a solids-forming inverse Brayton cycle cryogenic process that uses the flue gas as its own refrigerant, or an auto-refrigerant process. At the coldest temperatures, flue gas forms solid CO_2 during the expansion. These solids present both an abrasion and an imbalance problem. The abrasion problem differs little from droplet formation during steam expansion, and stream turbines routinely condense 8 % or more stream during expansion with no adverse effects. By contrast, the CO_2 content in the flue gas at this stage of the SES's CCC process is 5 %. The imbalance problem could be more difficult to mitigate. Liquid water condensing from

steam does not accumulate on turbine blades but solid CO_2 might. SES has successfully tested this process on small but commercial cryogenic turbines with simulated flue gas. Nevertheless, interest remains high in a process that does not require direct flue gas expansion in a turbine or flue gas (a sour gas) compression in a compressor. While the energetic cost of compression is high, one of the larger hurdles is the economic cost of sour gas compressors. The compressor cost will likely carry significant consideration in the implementation of desublimation by expansion cooling.

One embodiment of CCC uses desublimation by expansion cooling for a portion of the CO_2 solids formation. In Compressed Flue Gas Cryogenic Carbon Capture (CCC CFG), the flue gas from a power plant is cleaned, compressed, and cooled to near its frost point. A first desublimating heat exchanger is used to remove a portion of CO_2 from the flue gas before expanding in a turbine to remove the remaining CO_2 from the flue gas. The flue gas then recuperatively warms against itself. While CCC CFG is more energetically favorable than CCC ECL, it has the technical challenge of unknown turbine operational performance, and thus is not expected for near-term CCC installations.

3.1.2 Desublimation by Indirect Contact Heat Exchange

CO_2 solids can also be formed from cooling the process stream in a fluidized bed or mechanically cleaning unit operation that removes solid CO_2 from the heat exchange surfaces. This indirect contacting method of using a contained refrigerant to provide cooling through a surface to the gas stream prevents any mass transfer between the flue gas and the refrigerant. Indirect contact heat exchange also has the major advantage of no separations of solid CO_2 from contact liquid. Indirect contact heat exchange has its own technical problems with unknown operational challenges. In early demonstrations, Sustainable Energy Solutions encountered

significant challenges with maintaining clean heat exchange surfaces. In the case of full-scale deployment, operational time between maintenance cycles is a critical metric.

3.1.3 Desublimation by Direct Contact Heat Exchange

Direct contact heat exchange is operationally simple. A cold liquid stream is mixed with the CO_2-process stream in a vessel, column, or spray tower. The cold liquid cools the process stream, forming solid CO_2 particles which are entrained in the liquid. The cold liquid is generally thought to be a hydrocarbon mixture, but can include any liquid that has a low vapor pressure, and low viscosity at low temperatures. Due to the direct contact of the cold liquid and the process stream, both hydrocarbon emissions and CO_2/contact liquid separations present significant technical challenges. In the case of hydrocarbon emissions, hydrocarbon 1, hydrocarbon 2, and hydrocarbon 3 have been identified, tested, and labeled as viable contact liquid components that will meet hydrocarbon emissions limits at temperatures for 90 % or higher carbon capture. In the case of lower carbon capture and thus warmer temperatures, hydrocarbon 3 would no longer meet the hydrocarbon emission limits, but many other readily available hydrocarbons would. Solid/liquid separations are also a major concern, but are more manageable technical developments because of existing process equipment that operates under similar principles.

3.2 Solid-CO_2 Vapor Pressure

All CO_2 removal predictions depend heavily on the solid-CO_2 vapor pressure. New parameters for the solid-CO_2 vapor pressure were regressed by minimizing the sum of squared errors from several literature sources (Table 3-1). Regression of these data with several empirical vapor pressure equations (Antoine, Riedel, Wagner, Span and Wagner[99]) produced mixed results, with the Riedel and Wagner equations having the lowest sum of squared errors. The 5 parameter Riedel equation with newly regressed parameters fits data at temperatures above 150 K well, but

has significant deviations at lower temperatures. Since the region of greatest interest to this work ranges from the triple point (216.6 K) to processing temperatures around 150 K, another term was added inside the exponential, $\frac{F}{T^2}$, with F as the 6th parameter. This improves the fit over the entire temperature range. The 6 parameter correlation (one of the 6 parameters, E, is assigned rather than correlated) is

$$\frac{P_{CO_2}^{sub}}{P_o} = \exp\left[\mathrm{A} + \frac{\mathrm{B}}{T} + \mathrm{C}\ \ln\left(\frac{T}{T_o}\right) + \mathrm{D}\ T^{\mathrm{E}} + \frac{\mathrm{F}}{T^2}\right] \qquad (1)$$

where T is temperature and $P_{CO_2}^{sub}$ is the solid-CO_2 vapor pressure. Table 3-2 indicates the parameters of the equation and the associated critical p-value. Statistical analysis of these coefficients indicates that each of them is significant. Figure 3-2 compares the improvement in prediction residuals with Design Institute for Physical Properties (DIPPR)[100] and National Institute of Standards and Technology (NIST)[101] correlations of the 3- and 5-parameter Riedel forms in the temperature region of interest and also indicates that the residual scatter in the data, as opposed to a lack of fit, dominates the residuals for the revised equation.

3.3 Equilibrium Predictions

All CCC processes require detailed understanding of solid-liquid-vapor phase behavior and gaseous absorption of CO_2 and related systems over broad temperature and pressure regimes, including cryogenic regimes. Since light gas absorption in liquids features prominently in these calculations, ideal mixtures provide poor approximations[102]. Equations of state (EOS) predict equilibrium compositions with Raoult's law being adequate for some solid-vapor equilibrium predictions. The Peng-Robinson (PR), Soave-Redlich-Kwong (SRK), and Predictive Soave-Redlich-Kwong (PSRK) EOS provide fugacity coefficients and related parameters to improve the Raoult's law assumption. The PR and SRK require experimentally measured interaction

Table 3-1 Summary of published solid-CO_2 vapor pressure data

# of Data	Temperature [K]	Pressure [Pa]	Reference
62	69 - 103	$7 \cdot 10^{-8}$ - 0.05	Bryson et al.[103]
11	106 - 154	0.1 - 1,334	Tickner & Lossing[104]
7	138 - 195	133 - 100,000	Stull[105]
8	140 - 195	200 - 101,000	Kaye & Laby[106]
20	153 - 204	1,333 - 200,000	Thermodynamic Research Center[107]
6	154 - 196	1,509 - 111,000	Giauque & Egan[108]
131	154 - 217	1,490 - 527,000	Bilkadi et al.[109]
16	178 - 198	23,700 - 131,000	Ambrose[110]
19	192 - 195	86,000 - 102,000	Heuse & Otto[111]
21	194 - 217	97,700 - 517,000	Fernandez-Fassnacht & Del Rio[112]
28	194 - 217	99,000 - 518,000	Meyers & Van Dusen[113]
1	195	101,325	Mullins et al.[114]
1	195	101,325	Marsh[115]
6	201 - 213	179,000 - 385,000	Baughman et al.[116]

Table 3-2 Parameters for solid-CO_2 vapor pressure correlation

	A	B [K]	C	D [K^{-6}]	E	F [K^2]	T_o [K]	P_o [Pa]
Value	57.52	-3992.84	-4.9003	2.415E-15	6	8125.6	1	1
P-Value	4E-18	9E-36	8E-12	9E-7	-	5E-12		

parameters. The PSRK predicts the liquid-phase activity coefficient from a modified universal quasichemical functional-group activity coefficients (UNIFAC) model. This predicted activity coefficient can be transformed to a fugacity coefficient. Predictions accounting for non-idealities include the PR, SRK, and PSRK EOS. The PR and SRK EOS have similar accuracies in literature analyses of similar conditions[117]. Investigators have proposed other methods, including an extended Peng-Robinson for CO_2[118] and new EOS[119-121], that are potentially applicable to this study, but these are not discussed here.

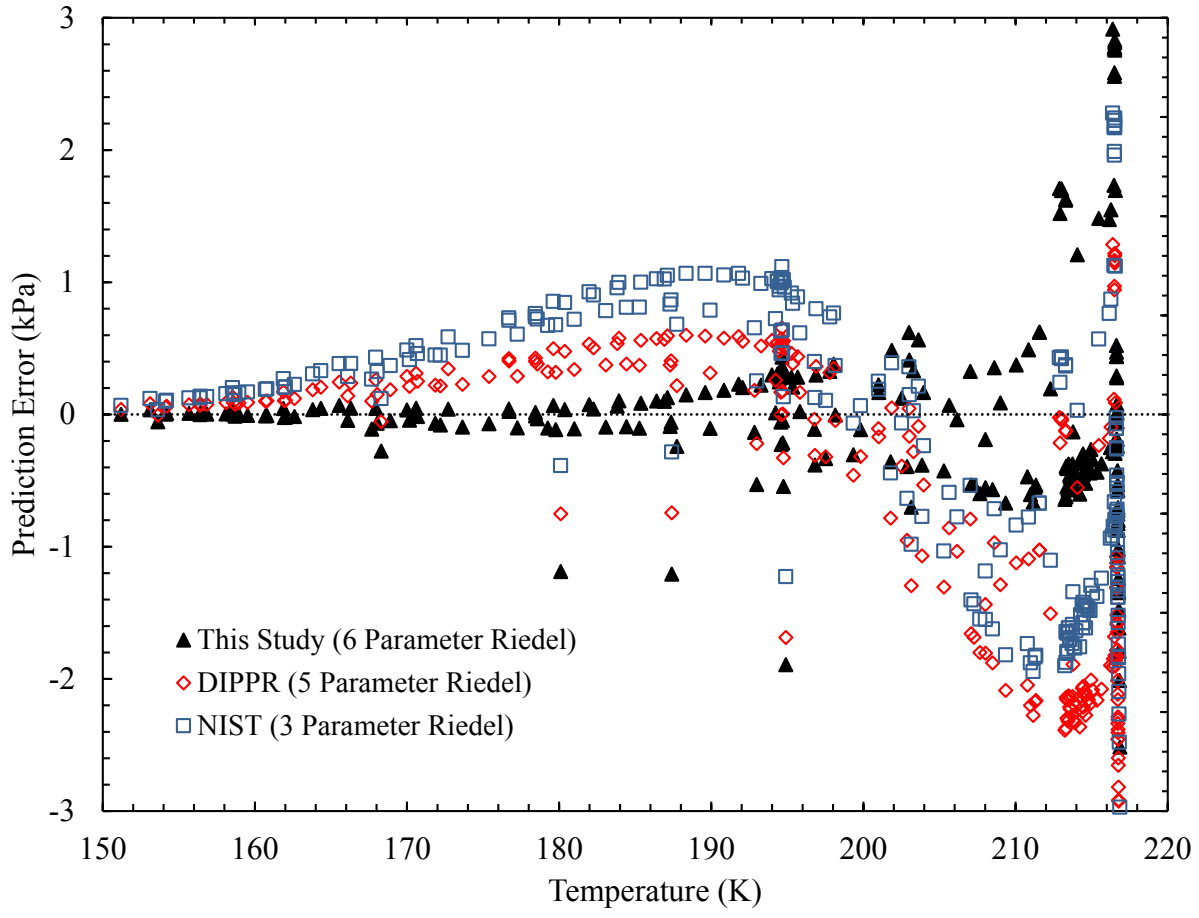

Figure 3-2 Residuals of solid-CO_2 vapor pressure with correlations from DIPPR & NIST

3.3.1 Raoult's Law

Raoult's law can be used as a starting point for estimating CO_2 phase equilibrium for vapor and solid phases. Raoult's law, applied to CO_2, is

$$x_{CO_2} P_{CO_2}^{sub} = y_{CO_2} P \qquad (2)$$

where x_{CO_2} and y_{CO_2} are mole fractions of CO_2 in the condensed and vapor phases, respectively, $P_{CO_2}^{sub}$ is solid-CO_2 vapor pressure, and P is total pressure. Donnelly and Katz reported that pure CO_2 melts at the same temperature as the solid found in equilibrium with vapors and liquids containing other hydrocarbons, signaling that the CO_2 forms an essentially pure solid phase[122], so the solid-phase activity coefficient is unity and $x_{CO_2} = 1$. Thus, Raoult's law predicts the mole fraction of CO_2 in the vapor phase as a function of temperature and total pressure (Eqn. 3).

$$y_{CO_2} = \frac{P_{CO_2}^{sub}(T)}{P} \qquad (3)$$

Significantly, the numerator in this expression is independent of the system composition as long as solid CO_2 is present.

Raoult's law can be applied to all species in the process stream. Figure 3-3 and Figure 3-4 illustrate Raoult's law predictions of vapor mole fractions of CO_2 and other components commonly found in natural gas as functions of temperature at a system pressure of 100 kPa and 4 MPa, respectively. In the case of 90 % CO_2 capture from a coal fired power plant, the outlet CO_2 concentration is slightly under 2 %. In the cases of specifications for natural gas in pipelines and typical LNG quality natural gas, CO_2 is removed down to 2 % and 50 ppm, respectively. Of particular importance is the trend that with higher pressures, much warmer processing

temperatures can be used. The warmer temperatures result in better refrigeration system performance and decrease the overall energy cost of removing the CO_2.

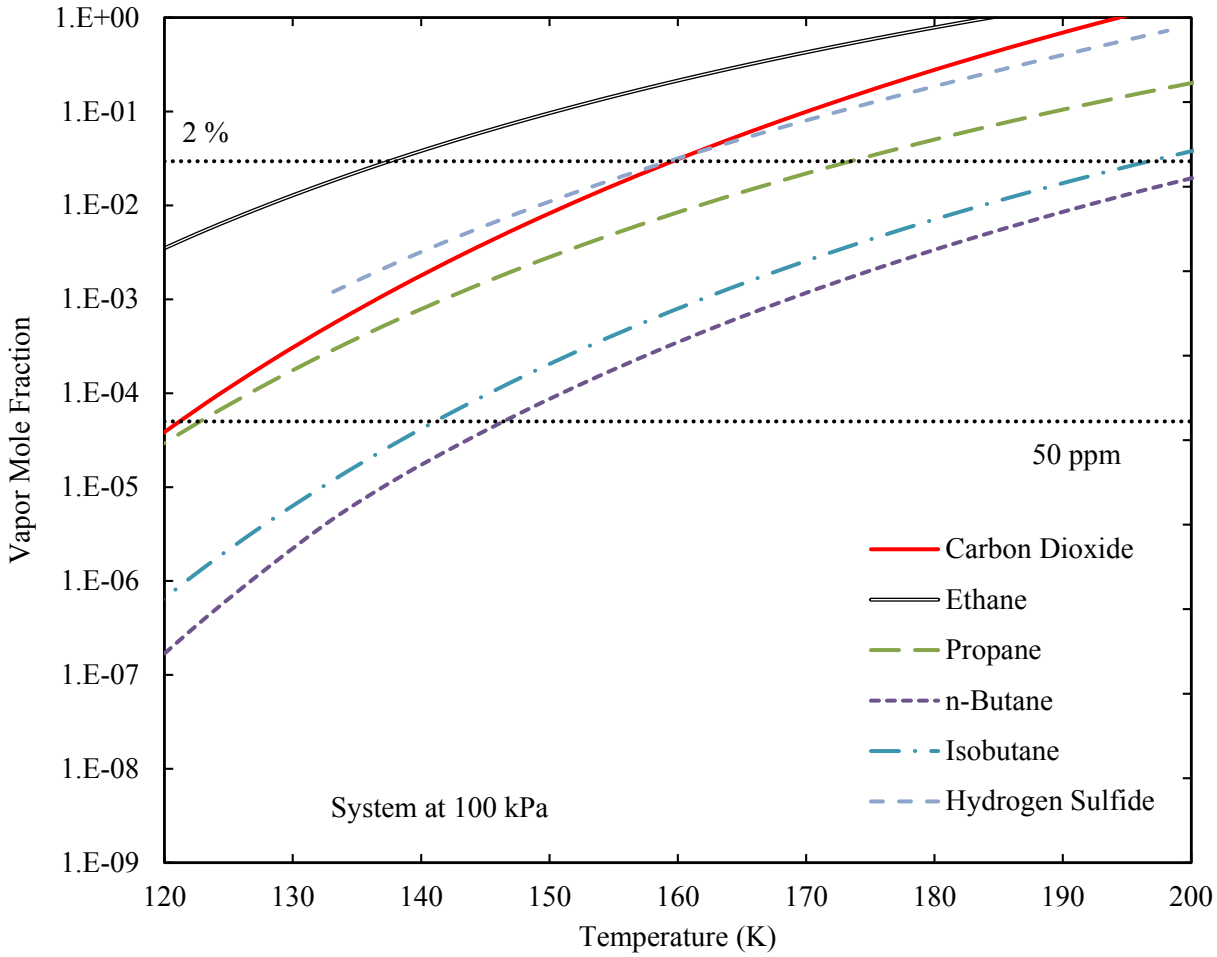

Figure 3-3 Raoult's law predictions of vapor phase for common natural gas components with a system pressure of 100 kPa

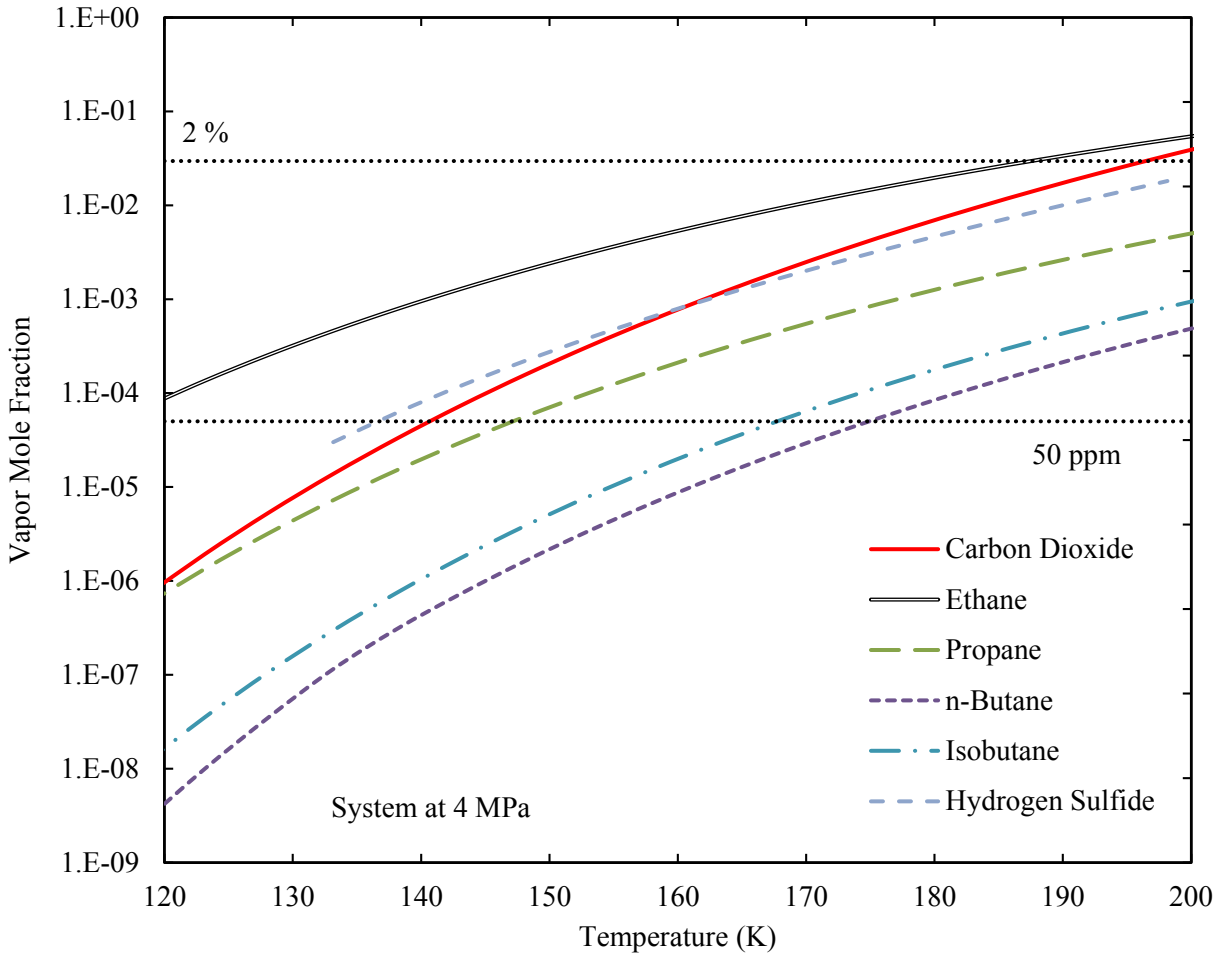

Figure 3-4 Raoult's law predictions of vapor phase for common natural gas components with a system pressure of 4 MPa

3.3.2 Peng-Robinson Equation of State (PR EOS)

Fugacity coefficients and a Poynting correction factor improve the estimation of fugacity, while still only considering the vapor and solid phases and assuming a pure solid CO_2 phase. The equilibrium equation in these terms is given by

$$\phi_{CO_2}^{sub} P_{CO_2}^{sub} e^{\frac{V_{CO_2}^{solid}(P-P_{CO_2}^{sub})}{RT}} = y_{CO_2} \bar{\phi}_{CO_2}^{vap} P \qquad (4)$$

where $\phi_{CO_2}^{sub}$ is the fugacity coefficient of pure CO_2 at the saturated pressure, $\bar{\phi}_{CO_2}^{vap}$ is the partial fugacity coefficient at total pressure, $V_{CO_2}^{solid}$ is the solid molar volume, and R is the universal gas constant. The fugacity coefficients depend on equations of state and approach unity at low pressure and high purity. For this study, both the PR and SRK EOS provide fugacity coefficients. Because the fugacity coefficients are functions of composition, the solutions are iterative.

In the case of CO_2 tolerant LNG, the estimation of liquid phase CO_2 can be predicted with a ϕ - ϕ method with a derivation described by De Guido et al[123]. This equilibrium is described with the equation

$$\phi_{CO_2}^{liq}\ exp\left[\frac{\Delta h_m}{RT_m}\left(1-\frac{T_m}{T}\right)+\frac{\Delta c_p}{R}\left(\frac{T_m}{T}-1-ln\frac{T_m}{T}\right)\right]=x_{CO_2}\,\bar{\phi}_{CO_2}^{liq} \qquad (5)$$

where $\phi_{CO_2}^{liq}$ is the liquid fugacity coefficient of pure CO_2 at the system temperature and pressure, Δh_m is the heat of fusion at the melting temperature, R is the universal gas constant, T_m is the melting temperature, T is the system temperature, Δc_p is the change in heat capacity from liquid to solid, x_{CO_2} is the liquid mole fraction of CO_2, and $\bar{\phi}_{CO_2}^{liq}$ is the partial liquid fugacity coefficient of CO_2 at the conditions of system temperature, pressure, and composition. Shen and Lin outline the equations and method to solve liquid fugacity coefficients for both the PR and SRK EOS[102].

The generalized form of the PR EOS[124] is

$$P=\frac{R\ T}{V_m-b}-\frac{a(T)}{V_m\,(V_m+b)+b\,(V_m-b)} \qquad (6)$$

$$a(T)=\ 0.45724\frac{R^2\ T_c^2}{P_c}\left[1+\kappa\left[1-\sqrt{\frac{T}{T_c}}\right]\right]^2 \qquad (7)$$

$$b=\ 0.07780\frac{R\ T_c}{P_c} \qquad (8)$$

$$\kappa = 0.37464 + 1.54226\omega - 0.26992\omega^2 \quad (9)$$

where R is the universal gas constant, V_m is the molar volume, T_c is the critical temperature, P_c is the critical pressure, and ω is the acentric factor. For the PR EOS, the partial fugacity coefficient (Eqn. 9) is best expressed in terms of compressibility (Eqns. 10-12) with classic mixing/combining rules (Eqns. 13-14).

$$\bar{\phi}_i = exp\left[Z - 1 - ln(Z - B) - \frac{A}{2\sqrt{2}B} ln\left(\frac{Z+(1+\sqrt{2})B}{Z+(1-\sqrt{2})B}\right)\right] \quad (10)$$

$$Z^3 - (1 - B)\, Z^2 + (A(T) - 3B^2 - 2B)Z - (A(T)B - B^2 - B^3) = 0 \quad (11)$$

$$A(T) = \frac{a(T)\ P}{R^2\ T^2} \quad (12)$$

$$B = \frac{b\ P}{R\ T} \quad (13)$$

$$a(T) = \sum_{i=1}^{N} \sum_{j=1}^{N} x_i x_j \sqrt{a(T)_i a(T)_j}\left(1 - k_{ij}\right) \quad (14)$$

$$b = \sum_{i=1}^{N} x_i b_i \quad (15)$$

where Z is the compressibility and k_{ij} is the binary interaction parameter. Interaction parameters are expressed with the functional form of

$$k_{ij} = A + \frac{B}{T} + \frac{C}{T^2} \quad (16)$$

where A, B, and C are fitted parameters for the particular system of components i and j.

3.3.3 Soave-Redlich-Kwong Equation of State (SRK EOS)

In the case of the SRK EOS, the cubic form with supporting functions[124] is

$$Z^3 - Z^2 + (A(T) - B - B^2)Z - (A(T)B) = 0 \quad (17)$$

$$a(T) = 0.42748 \frac{R^2 T_c^2}{P_c} \left[1 + \kappa \left[1 - \sqrt{\frac{T}{T_c}}\right]\right]^2 \quad (18)$$

$$b = 0.08664 \frac{R\ T_c}{P_c} \quad (19)$$

$$\kappa = 0.480 + 1.574\omega - 0.176\omega^2 \quad (20)$$

with classic mixing/combining rules (Eqns. 13-14) being applicable along with equations 10-12. However, the critical temperatures, pressures, acentric factors, and interaction parameters are typically independent of EOS parameters. Continuing on to solve for the SRK partial fugacity coefficient yields

$$\bar{\phi}_i = exp\left[Z - 1 - ln(Z - B) - \frac{A}{B} ln(1 + \frac{B}{Z})\right] \quad (21)$$

Reviews of experimental data estimate the thermodynamic parameters for the PR and SRK EOS. Available thermodynamic data from NIST and DIPPR are widely accepted, but are generally limited to pure-component vapor/liquid data. For the CO_2/CH_4 system with solid formation, proposed interaction parameter equations are available from Le[125], ZareNezhad[126], Shen et al[24,97], and De Guido[123]. The interaction parameter equations proposed have an effect of changing the predicted frost-point temperature less than 0.05 K in the temperature region of interest for natural gas processing, thus the non-temperature-dependent interaction parameter for CO_2/CH_4 from Aspen Plus' database was used.

3.3.4 Predictive Soave-Redlich-Kwong Equation of State (PSRK EOS)

The PSRK EOS allows predictions for systems that have no empirically measured interaction parameters. The PSRK uses the same general solid-liquid equilibrium (SLE) equations outlined previously, but a different method for calculating fugacity. Holderbaum and Gmehling

outline the equations for PSRK[127]. The volume parameter, r_i, represents the molecular-structure-weighted sum of the Van der Waals sub group volume properties, R_k, and, in combination with the composition, determines the volume fraction, V_i and modified volume fraction, V_i'. The surface area parameter, q_i, represents the molecular-structure-weighted sum of the Van der Waals sub group surface areas, Q_k, and determines the surface area fraction, F_i.

$$r_i = \sum_{j=1}^{n_{sub}} (\nu_{j,i}\, R_k) \quad (22)$$

$$V_i = \frac{r_i}{\sum_{j=1}^{n_{comp}} (x_j\, r_j)} \quad (23)$$

$$V_i' = \frac{(r_i)^{\frac{3}{4}}}{\sum_{j=1}^{n_{comp}} \left[x_j\, (r_j)^{\frac{3}{4}}\right]} \quad (24)$$

$$q_i = \sum_{j=1}^{n_{sub}} (\nu_{j,i}\, Q_k) \quad (25)$$

$$F_i = \frac{q_i}{\sum_{j=1}^{n_{comp}} (x_j\, q_j)} \quad (26)$$

where n_{sub} is the number of subgroups, n_{comp} is the number of components in the mixture, $\nu_{j,i}$ is the quantity of subgroup j in the species i, and x_j is the molar fraction of species j in the mixture. These parameters determine the combinatorial portion of the activity coefficient, γ_{comb_i}.

$$\ln \gamma_{comb_i} = 1 - V_i' + \ln V_i' - \frac{z}{2}\, q_i \left(1 - \frac{V_i}{F_i} + \ln \frac{V_i}{F_i}\right) \quad (27)$$

where z is the average number of molecules with which a given molecule interacts, or the coordination number, and usually assumes a value of ten[124].

The equations below determine the residual contribution to the activity coefficient of group j in a pure fluid of species i, $\Gamma_{j,i}$. They account for the mixture effects of the residual activity coefficient.

$$\psi_{i,j} = \exp\left(\frac{-\Delta u_{a_{i,j}} + \Delta u_{b_{i,j}} T + \Delta u_{c_{i,j}} T^2}{T}\right) \quad (28)$$

$$X_{j,i} = \frac{\nu_{j,i}}{\sum_{k=1}^{n_{sub}} \nu_{k,i}} \quad (29)$$

$$\Theta_{j,i} = \frac{Q_j \; X_{j,i}}{\sum_{k=1}^{n_{sub}} (Q_k \; X_{k,i})} \quad (30)$$

$$ln\Gamma_{j,i} = Q_j \left(1 - ln\left(\sum_{k=1}^{n_{sub}} \left(\Theta_{k,i} \; \psi_{s2m_k,s2m_j}\right)\right) - \sum_{k=1}^{n_{sub}} \frac{\Theta_{k,i} \; \psi_{s2m_l,s2m_k}}{\sum_{l=1}^{n_{sub}} \Theta_{l,i} \; \psi_{s2m_l,s2m_k}}\right) \quad (31)$$

The equations below determine Γ_{M_i}, the pure effects of individual components in the system for the residual activity coefficient.

$$X_{M_i} = \frac{\sum_{j=1}^{n_{comp}} (\nu_{i,j} \; x_j)}{\sum_{j=1}^{n_{comp}} \sum_{k=1}^{n_{sub}} (\nu_{k,j} \; x_j)} \quad (32)$$

$$\Theta_{M_i} = \frac{Q_i \; X_{M_i}}{\sum_{j=1}^{n_{sub}} (Q_j \; X_{M_j})} \quad (33)$$

$$ln\Gamma_{M_i} = Q_i \left(1 - ln\left(\sum_{j=1}^{n_{sub}} \left(\Theta_{M_j} \psi_{s2m_j,s2m_i}\right)\right) - \sum_{j=1}^{n_{sub}} \frac{\Theta_{M_j} \; \psi_{s2m_i,s2m_j}}{\sum_{k=1}^{n_{sub}} \Theta_{M_k} \; \psi_{s2m_k,s2m_j}}\right) \quad (34)$$

$$\ln \gamma_{res_i} = \sum_{j=1}^{n_{sub}} [\nu_{j,i} (\ln \Gamma_{M_j} - \ln \Gamma_{j,i})] \quad (35)$$

The overall activity coefficient for species i, γ_i, includes the combinatorial and residual portions of the activity coefficients calculated previously.

$$\gamma_i = \exp(\ln \gamma_{comb_i} + \ln \gamma_{res_i}) \quad (36)$$

The activity coefficient converts to a fugacity coefficient to use in the previous equilibrium equations. A temperature-dependent expression, f, is a factor in a_i to improve accuracy of the model.

$$f = \left[1 + c_{1_i}\left[1 - \left(\frac{T}{T_{c_i}}\right)^{0.5}\right] + c_{2_i}\left[1 - \left(\frac{T}{T_{c_i}}\right)^{0.5}\right]^2 + c_{3_i}\left[1 - \left(\frac{T}{T_{c_i}}\right)^{0.5}\right]^3\right]^2 \; if \; \frac{T}{T_{c_i}} < 1 \quad (37)$$

$$f = \left[1 + c_{1_i}\left[1 - \left(\frac{T}{T_{c_i}}\right)^{0.5}\right]\right]^2 \; if \; \frac{T}{T_{c_i}} > 1 \qquad (38)$$

The energy and volume parameters a and b, respectively, are factors in a dimensionless α, and $\bar{\alpha}$ that in turn partly determine the partial liquid and vapor fugacity coefficients.

$$a_i = 0.42748 \frac{R^2\left(T_{c_i}\right)^2}{P_{c_i}} f \qquad (39)$$

$$b_i = 0.08664 \frac{R\,T_{c,i}}{P_{c,i}} \qquad (40)$$

$$b_{mix} = \sum x_i\, b_i \qquad (41)$$

$$\alpha_i = \frac{a_i}{b_i\left(T_{c_i}\, P_{c_i}\right) R\, T} \qquad (42)$$

$$\bar{\alpha}_i = \frac{1}{-0.64663}\left(\ln \gamma_i + \ln \frac{b_{mix}}{b_i} + \frac{b_i}{b_{mix}} - 1\right) + \alpha_i \qquad (43)$$

$$\ln \bar{\phi}_i^{liq} = \frac{b_{srk}}{b_{mix}}\left(\frac{P\, v_{mix}}{R_g\, T} - 1\right) - \ln \frac{P\, v_{mix} - b_{mix_{srk}}}{R_g\; T} - \bar{\alpha}_i \ln \frac{v_{mix} + b_{mix}}{v_{mix}} \qquad (44)$$

$$\ln \bar{\phi}_i^{vap} = \frac{b_i}{b_{mix}}\left(\frac{P\, v_{mix}}{R_g\, T} - 1\right) - \ln \frac{P\, v_{mix} - b_{mix}}{R_g\; T} - \bar{\alpha}_i \ln \frac{v_{mix} + b_{mix}}{v_{mix}} \qquad (45)$$

Horstmann et al. tabulated all necessary parameters for the PSRK EOS for a variety of compounds (R_k, Q_k, group interaction, and basic pure component parameters)[128]. Table 3-3 and Table 3-4 list the parameters used in the PSRK EOS for the systems discussed in this dissertation.

Table 3-3 Sub group parameters for PSRK EOS

Sub Group	R_k	Q_k	c_1	c_2	c_3
CH_4	1.1292	1.124	0.49258	0	0
CH_3	0.9011	0.848	0.68638	-0.42475	0.72531
CH_2	0.6744	0.54	0.75108	-0.31941	0.59617
N_2	0.856	0.93	0.54268	0	0
CO_2	1.3	0.982	0.8255	0.16755	-1.7039
CH	0.4469	0.228	0.88771	-0.50468	0.94255

Table 3-4 Main group interaction parameters for PSRK EOS

		CH_4	CH_2	N_2	CO_2
CH_4	Δu_a	0	68.141	64.108	196.16
	Δu_b	0	-0.7386	0	0
	Δu_c	0	0	0	0
CH_2	Δu_a	-39.101	0	527.33	919.8
	Δu_b	0.84587	0	-2.1596	-3.9132
	Δu_c	0	0	0.43234	0.46309
N_2	Δu_a	11.865	-101.96	0	694.28
	Δu_b	0	0.68629	0	-3.0173
	Δu_c	0	-0.2066	0	0
CO_2	Δu_a	73.563	-38.672	-580.82	0
	Δu_b	0	0.86149	3.6997	0
	Δu_c	0	-0.17906	0	0

* Δu_a is in units K, Δu_b unitless, and Δu_c in units 1/K

3.3.5 Validation of Prediction Tools

Literature data are not available for equilibrium conditions of flue gas and solid CO_2. However, CO_2 frost-point temperatures are extremely important in the natural gas processing industry and multiple groups have published them. These data mostly involve binary mixtures of CO_2 with CH_4, with some ternary mixtures including C_2H_6 and N_2. The experimental frost-point temperature data provide a means to validate predictions of the previously discussed equilibrium methods. The vapor frost-point data appear in Table 3-5. The goodness of fit or correlation is reported by the bias, average absolute deviation (AAD) and mean square error (MSE), defined as

$$bias = \frac{1}{n}\sum_{i=1}^{n} T_{calc} - T_{exp} \quad (46)$$

$$AAD = \frac{1}{n}\sum_{i=1}^{n} \left|T_{calc} - T_{exp}\right| \quad (47)$$

$$MSE = \frac{1}{n}\sum_{i=1}^{n} \left(T_{calc} - T_{exp}\right)^2 \quad (48)$$

where n is the number of data in the data set, T_{calc} is the predicted frost-point temperature, and T_{exp} is the experimentally determined frost-point temperature. The new solid vapor pressure correlation makes a 0.2 K, 0.3 K, and 2.3 K^2 improvement in bias, AAD, and MSE, respectively, for predictions with the PR EOS compared to best published solid-vapor-pressure correlation of which we are aware, DIPPR[77].

Table 3-5 Summary of published CO_2 frost-point measurements with prediction goodness quantified by bias, AAD, and MSE for the PR EOS

Data	Temp [K]	Pressure [kPa]	Composition [%, balance CH_4]	Aspen Plus Bias [K]	Aspen Plus AAD [K]	Aspen Plus MSE [K^2]	DIPPR Bias [K]	DIPPR AAD [K]	DIPPR MSE [K^2]	New Bias [K]	New AAD [K]	New MSE [K^2]	Reference
Frost-Point Measurements of Binary Systems													
42	137-198	179-2785	0.1-10.7 CO_2	-1.4	2.0	5.5	-1.1	1.8	4.6	-0.8	1.6	3.8	Agrawal[129]
75	132-210	156-4790	0.03-59 CO_2	-0.6	0.7	1.0	-0.2	0.4	0.5	-0.1	0.4	0.2	Pikaar[130]
17	191-210	293-4446	10.8-54.2 CO_2	-0.2	0.7	0.6	-0.1	0.7	0.6	-0.1	0.7	0.6	Zhang[131]
39	170-200	689-2413	2-16 CO_2	-1.4	1.4	2.4	-1.2	1.2	1.7	-1.2	1.2	1.6	GPSA[75 A]
47	168-185	962-2464	1-2.9 CO_2	0.4	2.3	6.9	0.8	2.4	14.7	1.0	2.5	8.4	Le[132]
11	130-201	5000	0.2-20.5 CO_2	-5.0	5.0	57.5	3.7	3.7	39.9	5.3	5.3	39.6	Kurata[133 A]
Frost-Point Measurements of Ternary Systems													
19	154-172	172-2441	0.9 CO_2 & 0.7-2.9 N_2	-1.7	1.7	3.4	-1.3	1.4	2.4	-0.9	1.1	1.6	Agrawal[129]
24	174-184	1243-2262	1.9 CO_2 & 96-97 N_2	-0.4	1.7	3.7	-0.3	1.6	15.2	-0.1	1.6	3.4	Le[132]

[A]reported by ZareNezhad[126]

Figure 3-5 compares the frost-point predictions using Raoult's law with measurements. Pikaar's data highlights the poor assumption of Raoult's law for high pressure predictions. At low pressures fugacity coefficients approach unity, but for the case of high pressure measurements the fugacity coefficient of the vapor phase becomes a significant term. Figure 3-6 and Figure 3-7 show frost-point predictions with PR and SRK EOS, which account for the non-ideality at higher pressures and have improved correlation between predictions and measurements. Frost-point predictions generally fall within 3 K for both EOS, except for the measurements of Kurata, which

is the highest pressure data at 5 MPa. The residuals of Le's measurements in binary systems trend with pressure and are thus suspicious. Otherwise, for both the PR and SRK EOS the predictions are generally within ±3 K.

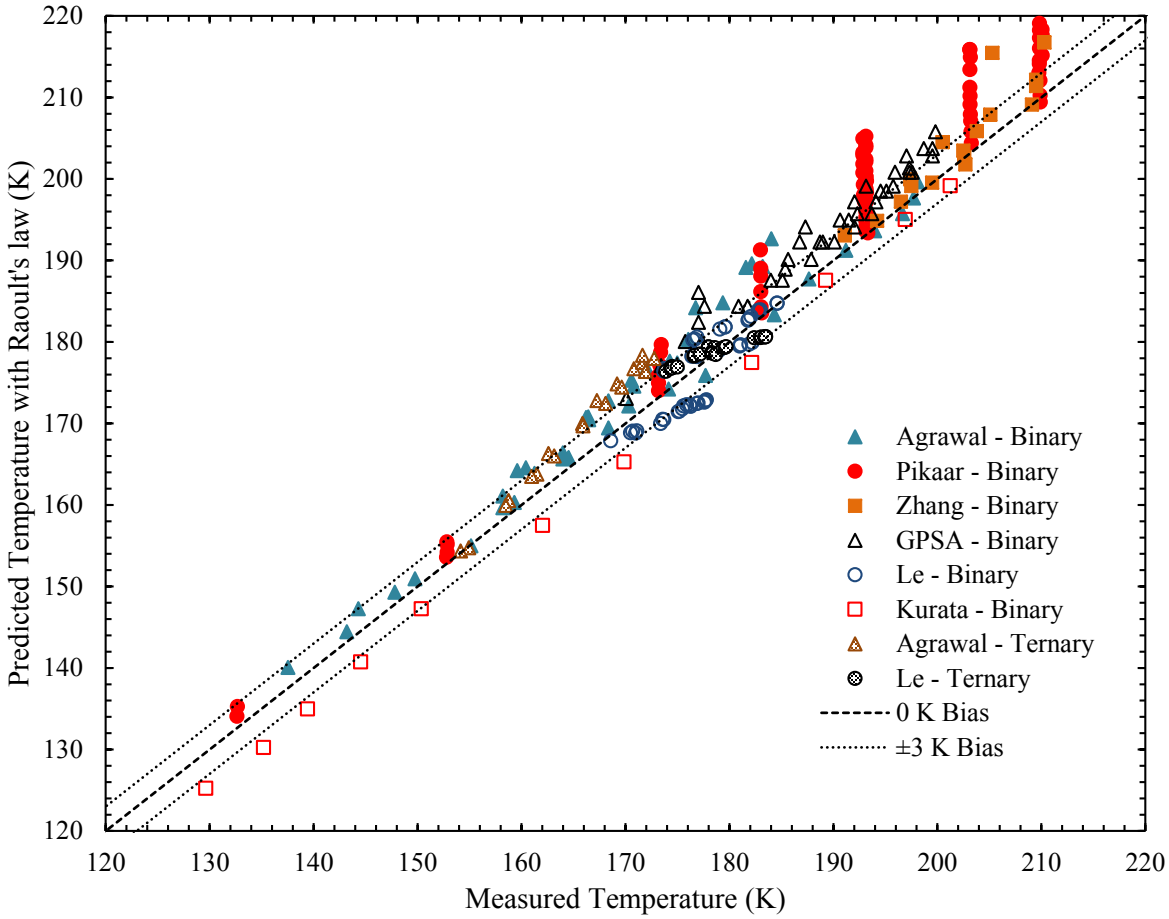

Figure 3-5 ***Frost-point temperature predictions with Raoult's law vs. measurements for binary and ternary systems***

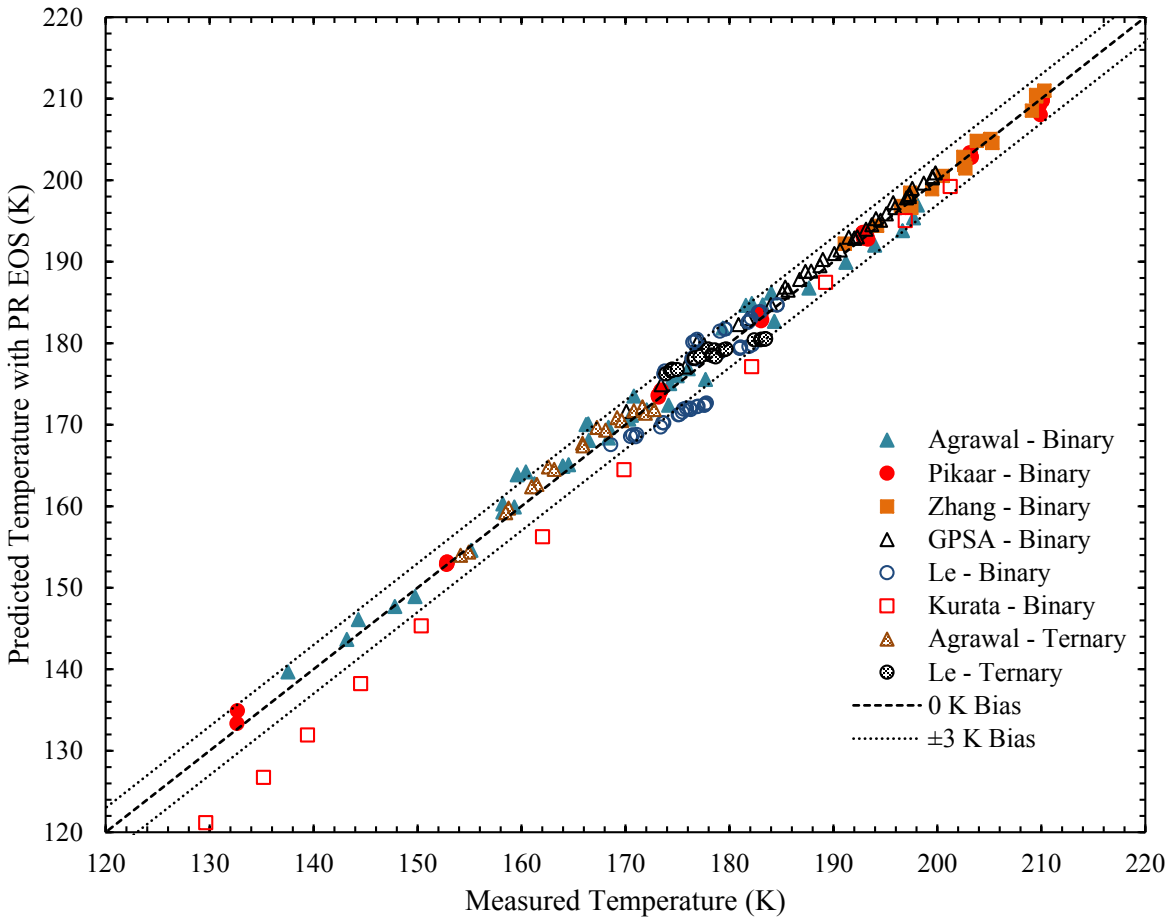

Figure 3-6 ***Frost-point temperature predictions with PR EOS vs. measurements for binary and ternary systems***

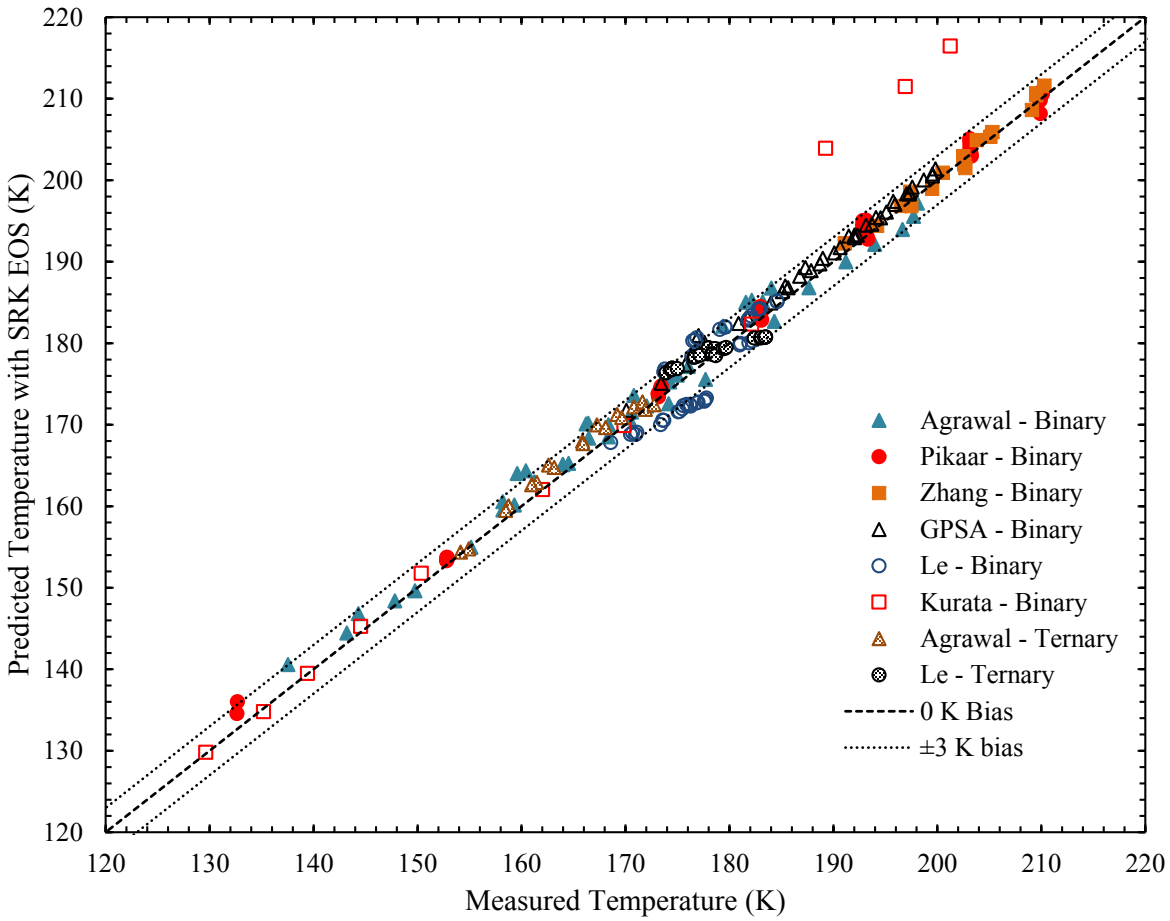

Figure 3-7 Frost-point temperature predictions with SRK EOS vs. measurements for binary and ternary systems

Measurements of CO_2 solubility in natural gas provide experimental validation of SLE computations. The data cover the temperature and pressure range of CCC LNG operation (112-190 K, 100-4000 kPa). Table 3-6 summarizes the data conditions and the goodness of the prediction methods. Figure 3-8, Figure 3-9, and Figure 3-10 show parity plots of predicted CO_2 vs. measured CO_2 for the PR, SRK, and PSRK EOS separately. The PR EOS provides marginally better predictions than the SRK EOS. The PSRK method is less accurate and overestimates the measured CO_2 concentration, but has the advantage of providing estimations without measured

species interaction parameters. Ternary system predictions exhibit the same nominal accuracy as binary systems.

Table 3-6 Summary of CO_2 solubility equilibrium data. Bias, AAD, and MSE in %

Data	Temp [K]	Pressure [kPa]	Composition [%, balance CH_4]	PR EOS Bias AAD MSE	SRK EOS Bias AAD MSE	PSRK EOS Bias AAD MSE	Reference
Binary Systems							
9	112-170	93-2315	0.02-2.9 CO_2	-0.02 0.02 0.00	-0.02 0.02 0.00	-0.52 0.52 0.00	Shen[97]
7	129-170	350-2315	0.16-2.9 CO_2	0.01 0.02 0.00	0.01 0.02 0.00	-1.21 1.21 0.02	Davis[134]
2	182-190	3306-3970	5.9-10.1 CO_2	1.06 1.06 0.02	1.12 1.12 0.02	-3.28 3.28 0.11	Davis[134]
Ternary Systems							
27	112-170	155-3150	0.02-2.8 CO_2 & 2-10 N_2	-0.04 0.05 0.00	-0.04 0.04 0.00	-0.54 0.54 0.00	Shen[97]
27	120-170	162-2228	0.05-3.3 CO_2 & 2-10 C_2H_6	-0.03 0.03 0.00	-0.03 0.03 0.00	-0.60 0.60 0.00	Shen[97]

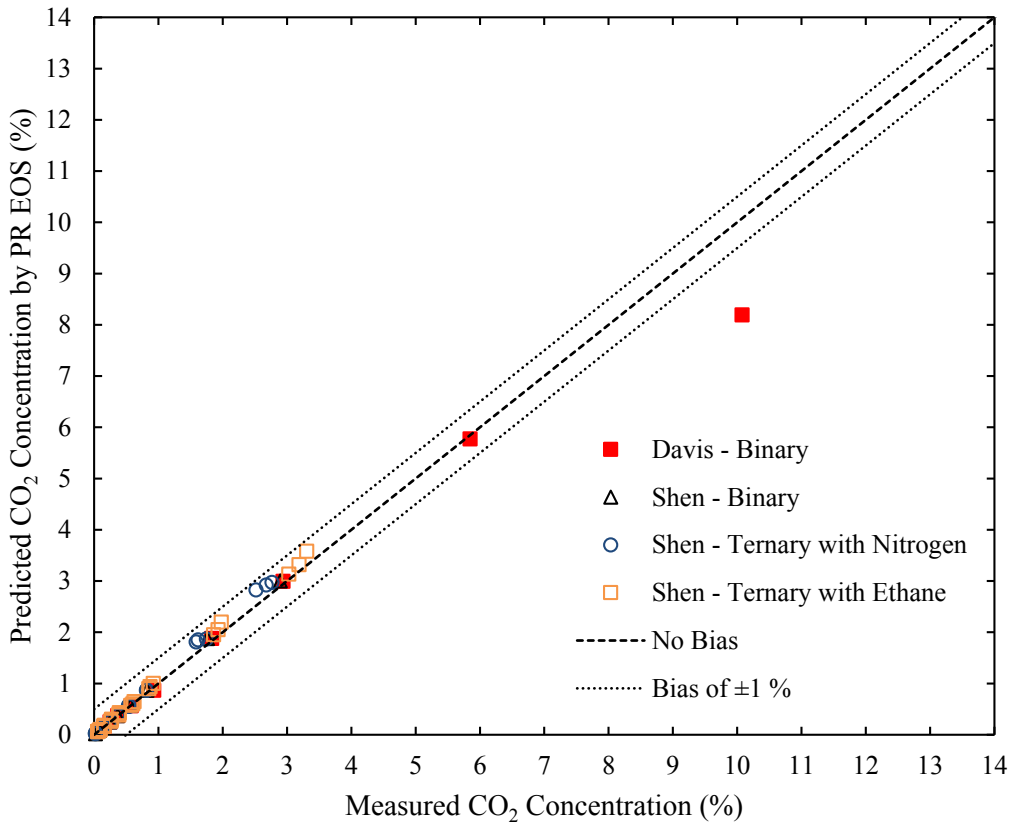

Figure 3-8 CO_2 solubility predictions from PR EOS vs. measurements for binary and ternary systems

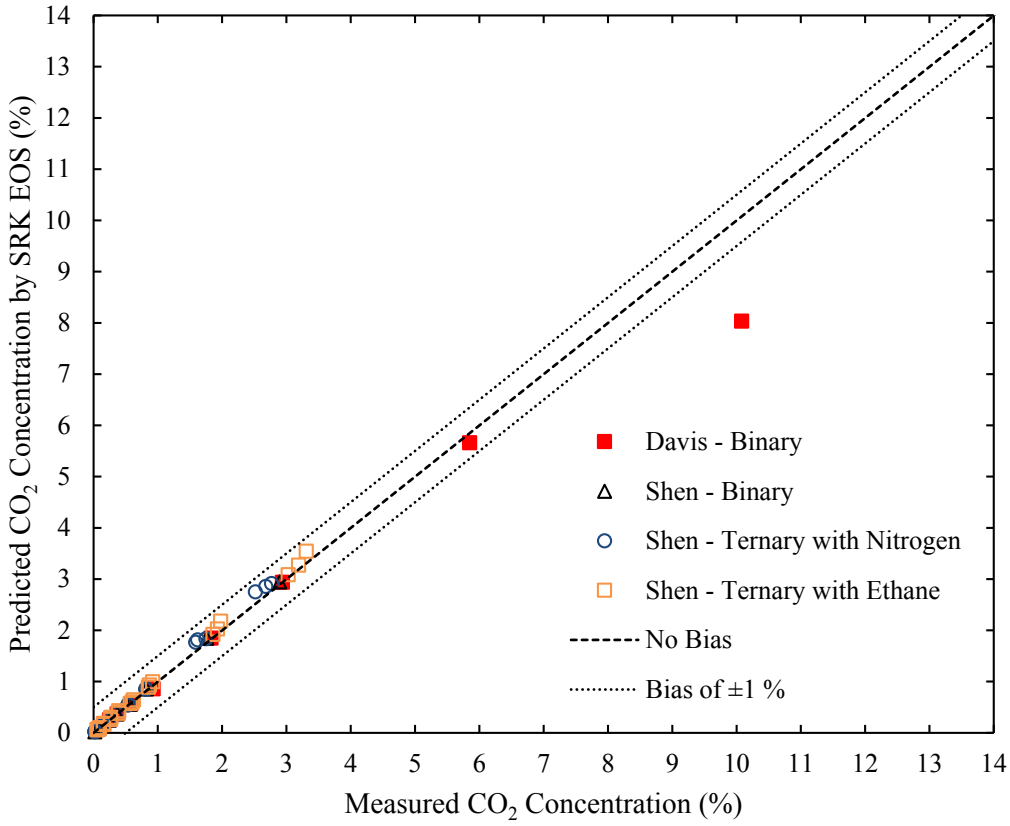

Figure 3-9 ***CO_2 solubility predictions from SRK EOS vs. measurements for binary and ternary systems***

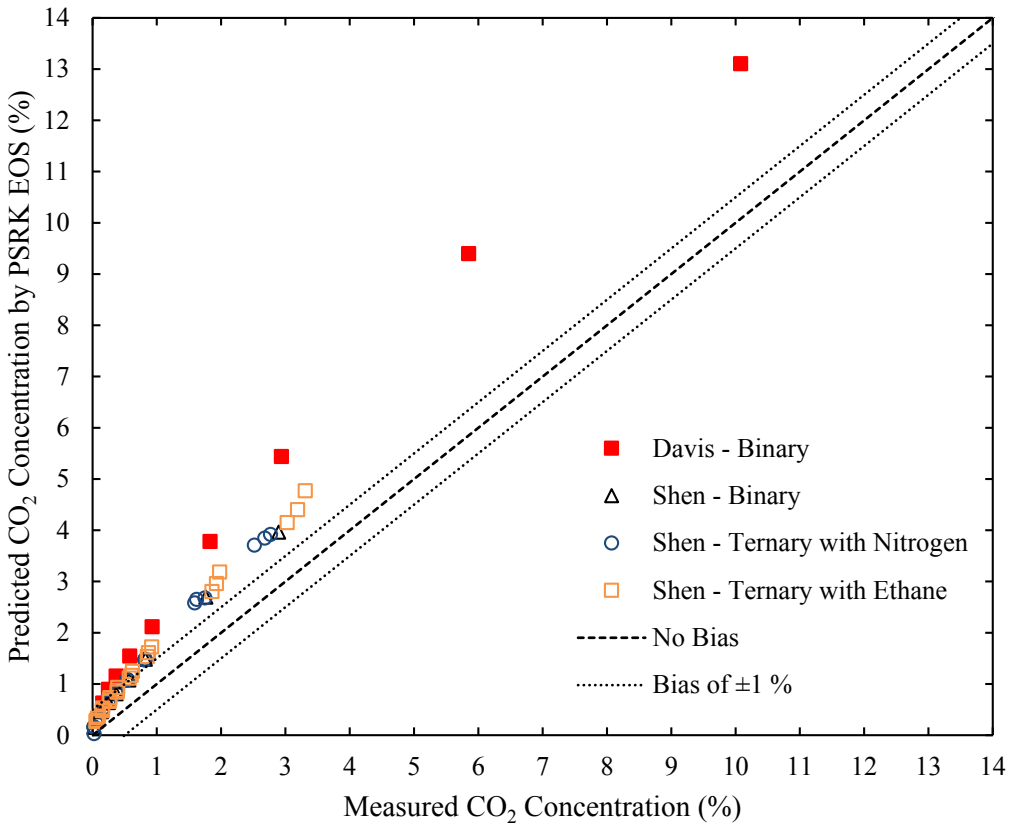

Figure 3-10 CO_2 solubility predictions from PSRK EOS vs. measurements for binary and ternary systems

The heat of fusion affects the predicted solubility and the optimal value is 8,485.9 and 8,481.1 J/mol for the PR and SRK EOS, respectively. These derived values for enthalpy of fusion are within 3 % of the value reported by De Guido et al. and well within the range of reported values in DIPPR. These values of heat of fusion improve the AAD by 0.04 % over the parameters of De Guido et al.

4 CCC EXPERIMENTAL APPARATUSES AND OPERATING PROCEDURE

Apparatuses of differing sophistication provide original experimental data for this exercise. The first generation apparatus allows visual verification of performance in the desublimating heat exchanger and had simpler materials for construction, facilitating multiple design iterations. The optical access provides highly useful qualitative information. However, the first generation apparatus provides a limited pressure operating range because of the optical access. The subsequent apparatuses provide increased flow rates and increased operating pressure (up to 4 MPa) at the expense of visual access.

All apparatuses are similar in process layout (Figure 4-1). Contacting liquid circulates through the desublimating heat exchanger and brazed-plate heat exchangers that are cooled with liquid nitrogen and/or an industrial cryogenic refrigeration system. A reservoir maintains liquid levels in all heat exchangers as density changed with operating temperature. Mass flow controllers introduce warm gas into the system. The system cools this gas in a brazed-plate heat exchanger before it enters the desublimating heat exchanger. The process gas exiting the desublimating heat exchanger warms against incoming streams. Various sampling ports provide composition analysis, troubleshooting and process monitoring access.

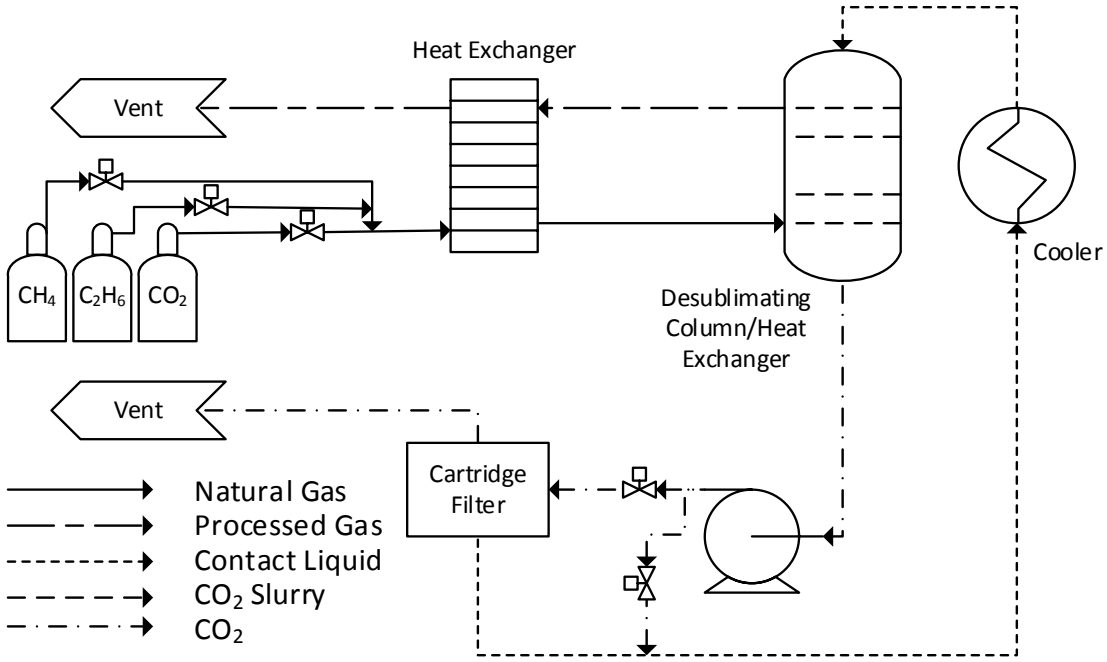

Figure 4-1 Simplified flow diagram of testing apparatus

All apparatuses use a staged bubbling heat exchanger column with direct contact between a cold liquid and the gas stream (Figure 4-2). Sieve plates create bubbles and high surface area between liquid and gas phases. As the gas cools in this column, CO_2 desublimates and entrains in the contact liquid for separation in subsequent units. The CO_2-lean process gas is the vapor product from the heat exchanger column. Froth was not seen in preliminary experiments, but is still considered since it can become a significant design factor if the conditions permitted froth formation (i.e. increased surface tension from low viscosity, stabilizing hydrocarbon composition, etc.).

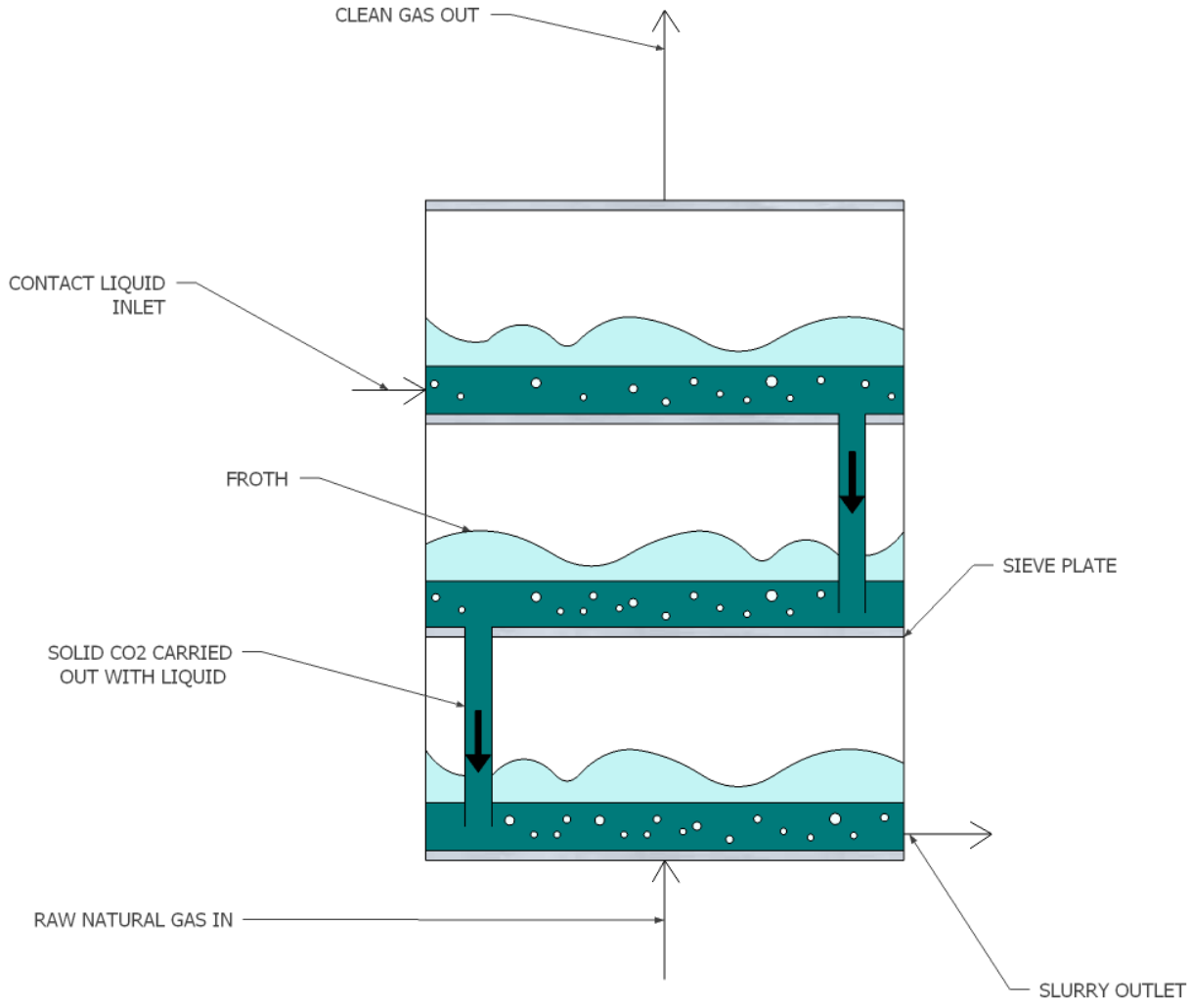

Figure 4-2 Multi-stage bubbling heat exchanger flow schematic

4.1 First Generation Apparatus

The visually accessible desublimating heat exchanger exterior surface includes two vacuum-separated concentric acrylic tubes. Internal stages of perforated Teflon sheeting create bubbles in a manner similar to sieve plates in conventional distillation. Stainless steel provides structural rigidity, a weir, and a downcomer. O-rings seal the stages against the exterior and the

steel frame provides stage separation and support, see Figure 4-3. The acrylic construction and vacuum-sealed walls are for experimental convenience.

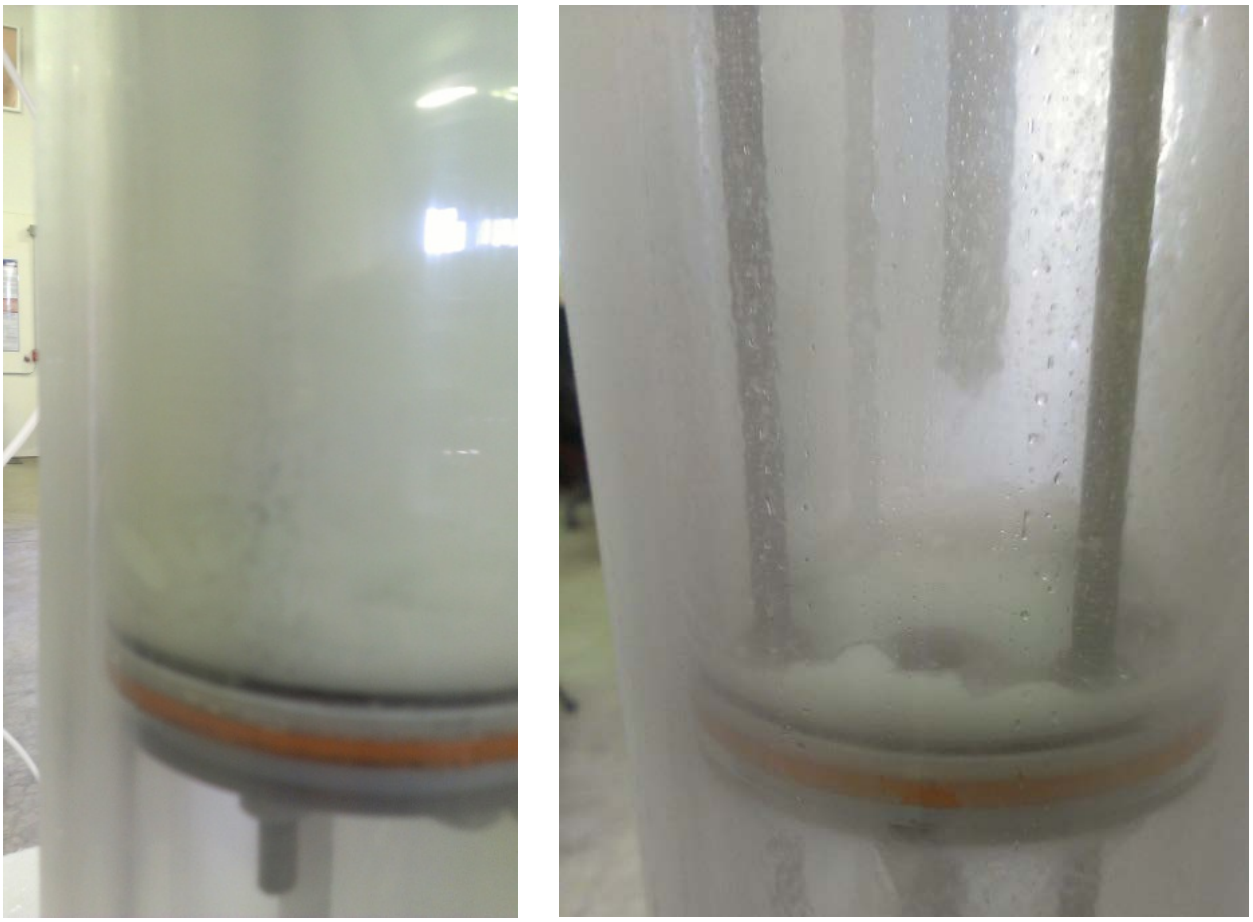

Figure 4-3 Single stage of heat exchanger during operation with solid CO_2 particles suspended in contacting liquid (left) and post-operation, drained, with solid CO_2 remaining (right)

Mass flow controllers provide an arbitrary gas composition. The low pressure apparatus had two mass flow controllers (Dakota) to provide an 85/15 mixture from cylinders (Airgas) containing 99.998 % pure N_2 and 99.5 % pure CO_2. An Enerac M-700 emissions analyzer initially provided a limited resolution of 0.1 %. Experiments in this system provided general feasibility

data and assisted in designing a new apparatus for larger flow rates for the CCC ES demonstration, and for a high-pressure apparatus capable of processing and liquefying natural gas.

4.2 CCC ES Apparatus

A larger skid-scale apparatus for CCC ES experiments was designed and built by Sustainable Energy Solutions to process larger gas flowrates. Data from the operation of this apparatus is used to validate the CCC ES models of this paper. This apparatus fills two 20' long standard high-C shipping containers. The first skid conditions the flue gas including a secondary deep flue gas desulfurization (FGD), two vessels of molecular sieve to dry the gas, a flue gas pressure booster, and the flue gas recuperative heat exchange (Figure 4-4). The molecular sieve dries the flue gas and operates as a semi-continuous batch operation. Most of the process control and instrumentation systems and the electrical drives are also in this skid.

Stainless steel brazed-plate heat exchangers (Pex Universe) provide process temperature changes and calibrated pressure transducers (Transducers Direct) with factory certification of 0.25 % accuracy monitor and control pressure. Type-K thermocouples (Omega) with certified uncertainty of ±1 K monitor temperature. A Simatics DCS (Siemens) records process parameters. The first skid also houses the industrial CO_2 analyzers (ABB EL3040). These analyzers have an increased resolution compared to the M-700 with a resolution of 0.006 %. The EL3040 analyzers work by non-dispersive infrared (NDIR) and are limited to the CO_2 concentration range of 0-30 % and 0-3 % for incoming and outgoing gases, respectively. Analyzers are calibrated with in-house calibration gases. In-house calibration gases are volumetrically made in a 1 L syringe (SGE). In some experiments, a 5975C quadrupole mass spectrometer (Agilent Technologies) provides additional analysis of the gas, specifically (1) verifying the adequacy of CO_2 measurements of ABB EL3040 and (2) quantifying the trace compounds (i.e. contacting liquid).

Figure 4-4 ***Flue gas conditioning skid for CCC ES with deep flue gas desulfurization (A), drier (B), blower (C), recuperative heat exchange (D), and electrical control area (E)***

The second skid contains the heart of the cryogenic carbon capture process. This skid contains two cryogenerators (Sterling Cryogenics SPC-4), the contact liquid cooling, the bubbling column, and solid CO_2 separations (Figure 4-5). Solid separation occurs in a continuous filter press adapted from similar commercial operation with sludges. An auger drives the continuous filter press, with special adaptations for the solid CO_2 particles.

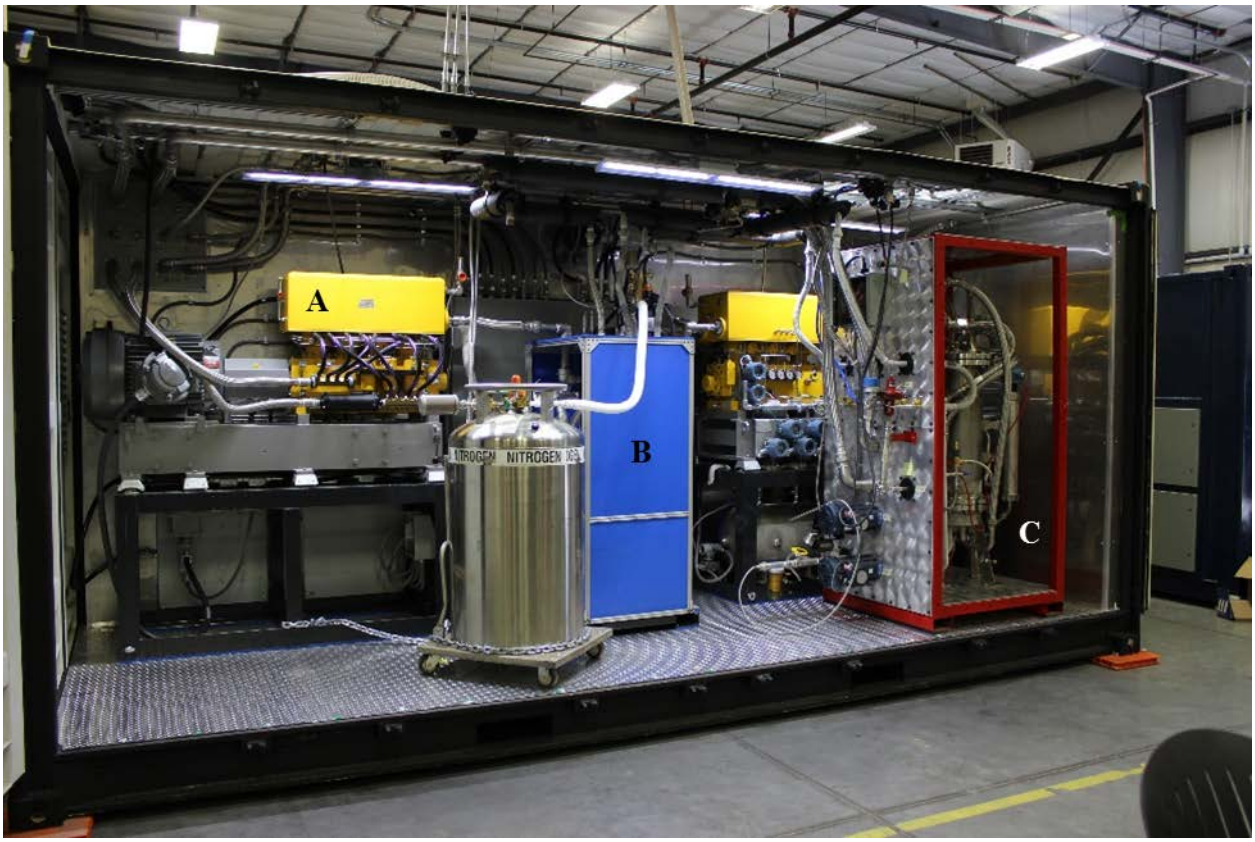

Figure 4-5 CCC skid for CCC ES with cryogenerators (A), contact liquid cooling (B), and bubbling CO_2 desublimating column (C)

4.3 Apparatus for Natural Gas Experimentation

A separate apparatus was designed and built for natural gas experiments with an operating pressure up to 4 MPa for realistic natural gas processing conditions, see Figure 4-6. Other improvements include a complete stainless steel construction to avoid deterioration and a 10 mm polycarbonate blast shield. Other safety considerations include a hydrocarbon sensor with interlock, an oxygen sensor, compliance with Class I, Division I national electric code (NEC) safety standards in the hydrocarbon-handling region, complete electrical isolation, and multiple pressure relief valves.

Figure 4-6 ***Natural gas capable apparatus with cylinder gas cabinet (A), FTIR (B), exhaust fume hood for flaring and venting (C), computer control interface (D), bubbler and separator cold box (E), reservoir cold box (F), data acquisition (G), mass flow controllers (H), heat exchange and pumping cold box (I), mass flow controller power supply (J), pump motor controller (K), pump motor (L), cryocooler (M)***

In these experiments, the process pressure ranges from local pressure (86 kPa absolute) to 4 MPa with an additional mass flow controller on the exhaust gas. Cylinders contain 99.5 % pure CO_2 (Airgas), 99.0 % pure CH_4 (Airgas), and 99.0 % pure C_2H_6 (Praxair). The limitation of the apparatus is the total flow rate of gas and was designed for 3.7 L/min based on four mass flow controllers (Brooks 5850). A Sensidyne Gilibrator bubble chamber provides flow calibration with gas analyzers verifying the composition of mixed gases. The uncertainty of the flow measurements is not significant because experiments reach phase equilibrium.

The cryogenic portion of the process occurs inside the cold boxes with cooling by liquid nitrogen or an industrial refrigeration system (Telemark TVP-2000), see Figure 4-7. Heat exchangers are stainless-steel, brazed-plate styles (GEA-PHE). A pump (Micropump EW-73005-06) circulates contacting liquid through the desublimating heat exchanger and brazed-plate heat exchangers. A cartridge filter removes solid CO_2 particles to extend experiment run times and to prevent CO_2 concentrations in the liquid from exceeding the solubility limit. The cartridge filter uses a stainless-steel, 30 x 30 mm mesh with 0.53 mm openings, and could regenerate by isolating, draining, and introducing warm nitrogen with manually operated valves. During the time the filter is not in operation for regeneration, particles continue to build up within the system. However, measurements are not reported during regeneration because the contacting liquid could have CO_2 concentrations greater than the liquid phase equilibrium.

The desublimating heat exchanger comprises a single stage stainless steel column with five 3.2 mm diameter holes for gas bubbling and a 13 mm diameter tube or downcomer, see Figure 4-8. The top of the downcomer is 25 mm above the bubbling plate, causing liquid to build up on the stage. The column rests on the inside of a stainless steel pressure vessel. Liquid at the bottom of the vessel ensures that entering gas progress up through the liquid on the tray and exchanges heat rather than passing the stage. At least 6 inches of perlite in every direction insulate the cold portions of the apparatus. In high-pressure experiments with complete liquefaction of natural gas, there is no vapor stream from the desublimating column, and the natural gas enters the desublimating column as a warm gas.

Figure 4-7 ***Inside view of cold boxes with perlite insulation removed. From left to right: heat exchange and pumping cold box, reservoir cold box, and bubbling heat exchanger and separations cold box***

Pressure and temperature strongly affect desublimating heat exchanger performance. The apparatus contains 16, K-type thermocouples (Omega) with uncertainties of ± 0.5 K in the range of 93-153 K. Four of the thermocouples measure the temperatures of the fluid streams immediately entering and exiting the desublimating heat exchanger. These thermocouples are calibrated by boiling pure nitrogen, pure methane, and pure ethane at known room pressures and comparing measured temperatures with theoretical boiling points at these pressures. The experimental apparatus also contains two pressure transducers (Transducers Direct) with uncertainties of ± 0.25 % over the range of 0-6.9 MPa. One of the pressure transducers is built into the desublimating heat exchanger, while the other monitors contact liquid pressure drop over the CO_2 solids filter. LabView DAQ (National Instruments) provide data acquisition and process control.

Figure 4-8 Stainless steel single stage column

A Horiba PG-250 initially provided gas composition analyses with a resolution of 0.01 %. The instrument operates with NDIR. Eventually, the Horiba was replaced with a MKS MultiGas 2030 FTIR spectrum-based gas analyzer to measure product composition. The MKS was calibrated for CO_2, CH_4, C_2H_6, and hydrocarbon 3 over the concentration ranges of the experiment with volumetrically and gravimetrically measured sample gases. Volumetrically measured sample gases were made in a 1 L syringe (SGE). Gravimetrically measured sample gases were made in a 40 cm^3 stainless steel cylinder with needle valves at either end. First, the cylinder was purged with nitrogen before pulling a vacuum (< 6 Pa) on the cylinder. The empty weight was measured with an analytical balance (Scientech SA310), with 0.1 mg resolution. Subsequently, sample gases were added up to 10 MPa with appropriate weight measurements. Calibration summaries are available in the appendix.

4.4 Experimental Procedure

Nitrogen purges the system prior to introducing the contact fluid, typically hydrocarbon 1, hydrocarbon 2, hydrocarbon 3, and/or C_2H_6. The system then cools by circulating the contact liquid through the system while a cryogenic refrigerator and/or liquid nitrogen cools the contacting fluid in brazed-plate heat exchangers to temperatures generally between 123 and 183 K. The volume of the contact liquid in the system is typically 2-3 L. The contact liquid circulates through the system at a rate of 2 L/min. When the contact liquid and process equipment are sufficiently cool, gas flow starts through the mass flow controllers at the desired composition. After starting the inlet gas flow, the exhaust valve or mass flow controller maintains a steady-state pressure as the system equilibrates.

5 ENERGY-STORING CRYOGENIC CARBON CAPTURE (CCC ES)

Cryogenic carbon capture with direct contact heat exchange enables a novel energy storage system by using an open loop natural gas refrigeration system. This energy-storing process replaces optimized refrigerants that might have been used in the CCC ECL process with natural gas. Energy is stored during non-peak times by liquefying more natural gas than the process demands, storing the excess in a cryogenic liquid storage tank. During peak demand, the stored liquefied natural gas provides most of the refrigerant to carry out the cryogenic separation process, relieving the parasitic load on the power plant. Once the natural gas vaporizes and warms, it combusts in a simple natural gas turbine, increasing power output of the power plant during peak demand, or is placed back in a pipeline for other uses. Flue gas from the turbine flows into the coal boiler to provide an effective combined-cycle system and ensure CO_2 removal from both natural gas and coal combustion products (Figure 5-1).

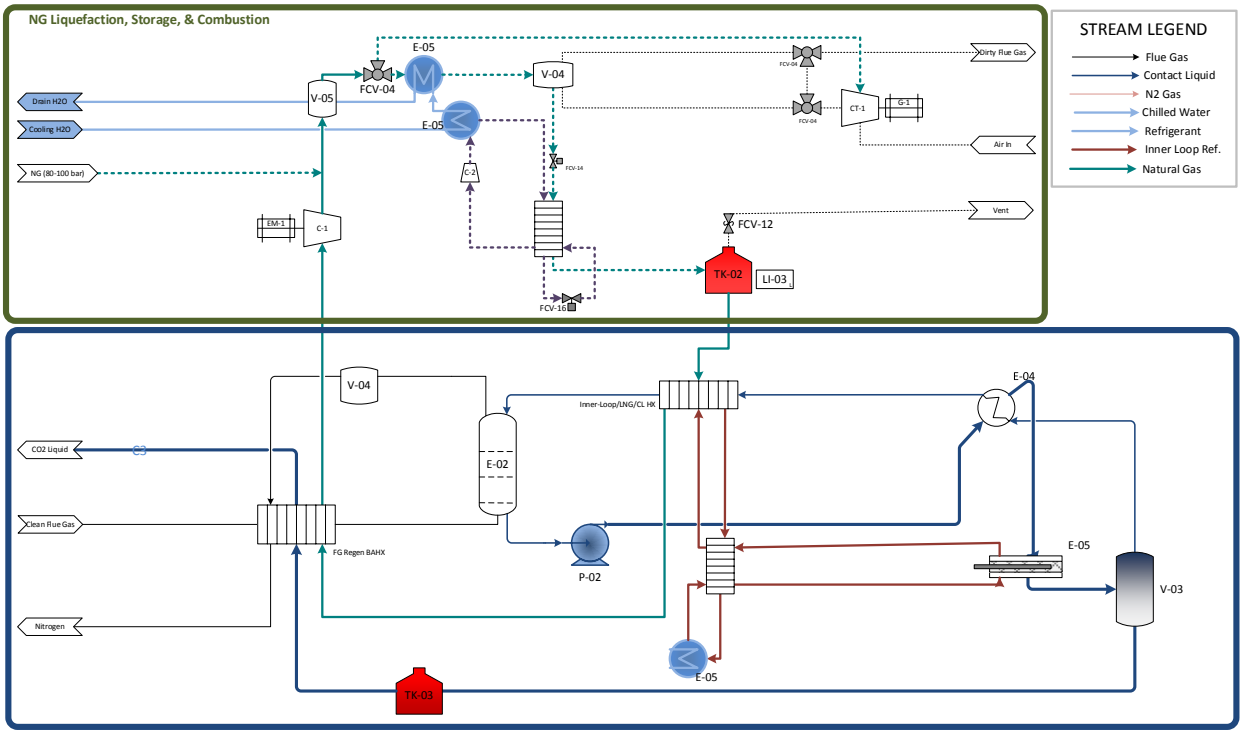

Figure 5-1 CCC ES flow diagram. Upper system is natural gas liquefaction and combustion. Lower system is CCC using LNG as refrigerant

This is a retrofit, bolt-on system that allows existing coal-fired power plants to reduce CO_2 emissions by up to 99 %, increases peak load capacity thru added natural gas combustion and by temporarily eliminates most of the parasitic loss of the CCC system, and increases load following ability by introducing a large intermittent refrigeration system and natural gas combustion cycle that can quickly change loads to produce or consume energy as needed.

The energy storage system design maintains peak generation capacity and levels energy demand from swings during a 24 hour period with a combustion. An extreme example of production variation can be seen in Denmark, where wind power can provide 100 % of energy demand when efficient winds are available. However, coal power plants are not able to turn off/on with the same time constant as the wind power and thus must remain on even during wind

production times. Coal-fired plants do not respond quickly in part due to the thermal stresses in the super-heater headers. To increase the timeliness of response, CCC ES integrates a fast-reacting LNG system that can consume the excess energy produced from the coal-fired boiler when wind satisfies primary demand.

Another contributing factor to the responsiveness of the new system is that energy is stored by liquefying natural gas with excess generation capacity during non-peak demand. The stored liquid natural gas is used as a refrigerant during peak demand, thus not consuming the energy produced during peak demand while still permitting the CO_2 removal process to proceed. Once the LNG vaporizes and warms in the refrigeration process, it combusts in a natural gas turbine or returns to the pipeline. In the case of combustion, the hot flue gas flows to the coal boiler, thus creating an effective combined cycle system for the cost of a simple cycle. The operational regimes of the process are depicted in Figure 5-2.

Overall, the proposed energy storage system (1) allows existing coal-fired plants to maintain and/or exceed current peak capacity while removing more than 90 % of CO_2, (2) allow existing coal-fired plants to efficiently integrate with intermittent power sources to reduce electricity waste, and (3) capture CO_2 from not only coal combustion, but from natural gas combustion as well. This innovative system could make the existing trillion dollar coal-fired electricity generation industry the most important strategic asset for balancing intermittent renewables and stabilizing the grid[135, 136] as well increase energy storage with no geological or limitations, such as mountains and water for pumped hydro storage. The grid stabilization and economic benefits of this energy system are under investigation separately. This work focuses on the technical details of liquid natural gas formation.

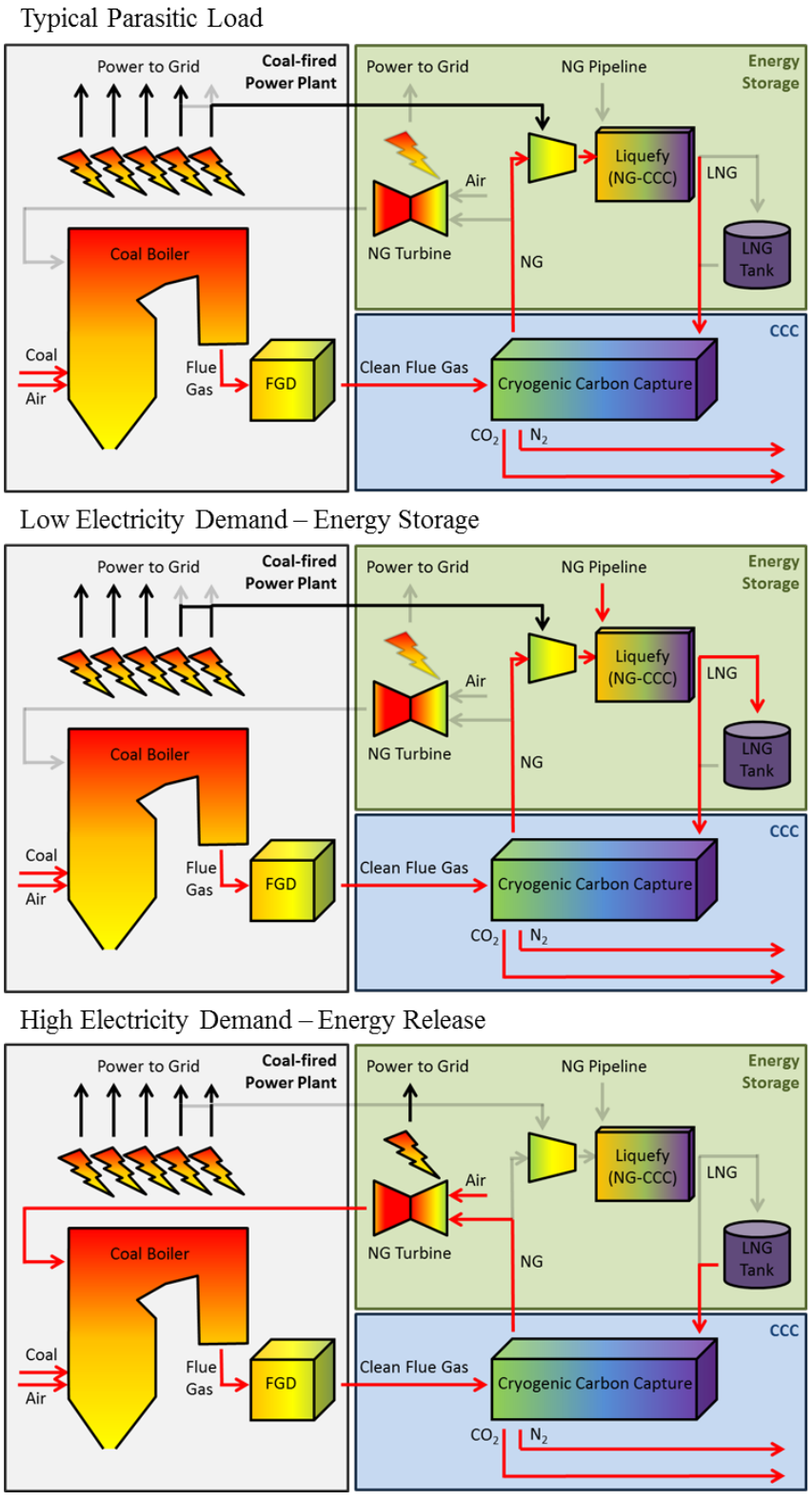

Figure 5-2 ***Operational regimes of CCC ES in conjunction with a coal-fired power plant for typical base parasitic load, energy storage, and energy release***

5.1 Natural Gas Thermal Storage

The open loop refrigeration system uses natural gas partly because of its widespread domestic availability, and proven energy production efficiency, and partly because it is possibly the only refrigerant that is inexpensive enough to be burned or returned to a pipeline rather than stored at the high-temperature end of the refrigeration cycle. Because of the large refrigeration load needed for cryogenic CO_2 separation, new delivery pipelines may be required. This research assumes that such network expansion is well understood and available.

Liquefied natural gas (LNG) requires refrigeration rather than pressurization because of methane's low critical temperature (190.45 K). The most common commercial process employed for natural gas liquefaction uses a combination of refrigeration cycles. The method chosen by most companies involves a propane precooler and a mixed refrigerant system (C_3MR)[137]. LNG facilities have existed and been under development for many years and the underlying process efficiency is approaching its practical limits[138]. Hence, we start with a practical LNG system such as the C_3MR process, Figure 5-3, but then optimize the liquefaction process for use in conjunction with the CCC system.

Natural gas enters the C_3MR process and cools to 235.15 K in a 4-staged compression/expansion refrigeration cycle that accounts for a linear portion of the natural gas cooling curve. Then a mixed refrigerant of methane, ethane, propane, and nitrogen further cools and condenses the natural gas[139]. Natural gas liquefaction occurs at high pressures (20-50 bar) with corresponding condensation temperatures at or near the critical temperature. The normal boiling point of LNG is about 109.15 K, which is the temperature at which it is commonly stored.

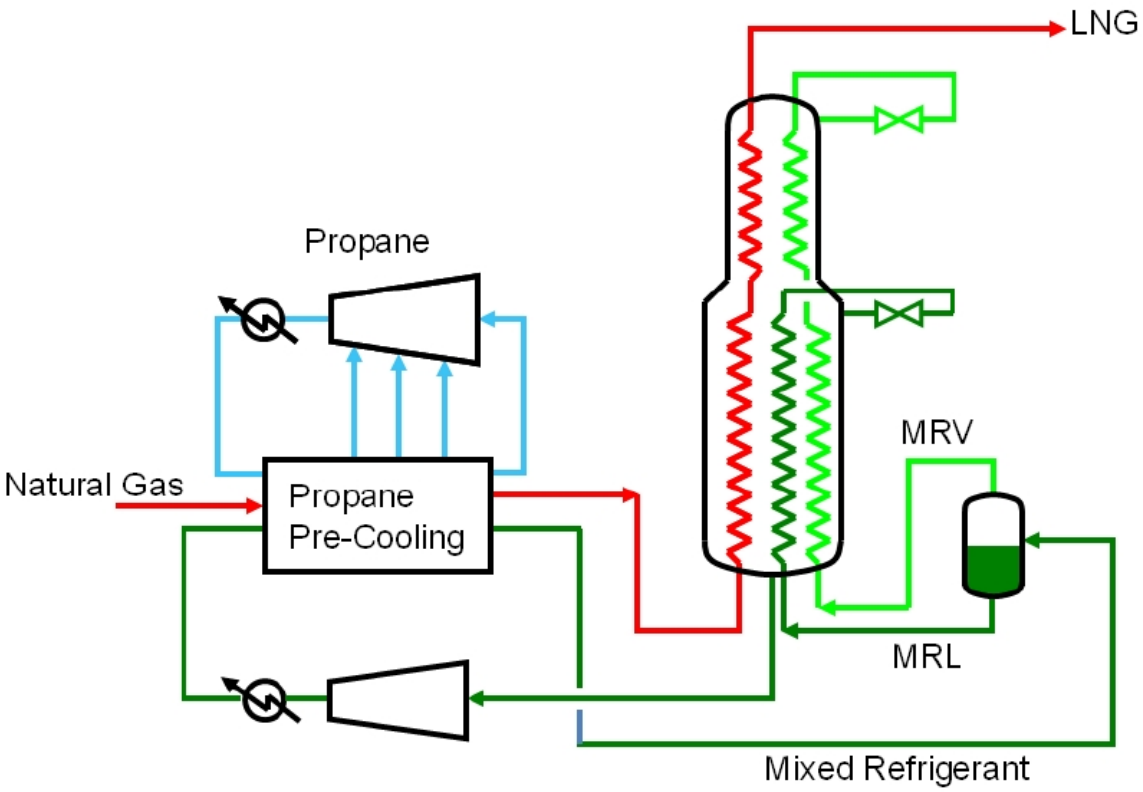

Figure 5-3 Air Products AP-C_3MR™ LNG process[140]

LNG will be generated and stored during low demand. Since commercial liquefaction and storage of natural gas occurs at stationary, land-based locations, LNG storage for CCC ES will use existing LNG tank technology. Storing at higher pressure, such as is done on shipping vessels, would be thermodynamically advantageous. Tanks used in shipping generally have a maximum allowable working pressure (MAWP) of 10-14 bar and a capacity of 36,250 m^3, which is on the order of magnitude of desired capacity. However, standard practice is to transport LNG at slightly above atmospheric pressure[141]. If necessary, a smaller, Kaptiza refrigeration cycle can be employed, using nitrogen as the refrigerant, to maintain the temperature in the storage vessel[142]. The nitrogen-based refrigeration system will employ a turbo-expander for energy recovery, unlike the liquefaction process which uses simple valves to expand the refrigerant with no energy

recovery. This nitrogen refrigeration process is similar to the AP-X™ process employed by Air Products.

Large land-based LNG containers are currently used near shipping ports for receiving and preparing LNG for shipment. Since these containers have been operated by the electric power industry for many years, the technology efficiencies are well developed and understood. Currently, the world's largest above-ground LNG storage tank is serving the world's largest LNG Importer, Korea Gas Corporation. The company's largest storage tank serves the Tongyoung and Pyeongtaek LNG receiving terminals and has a capacity of 200,000 m^3 with a boil-off rate of 0.05 % by volume per day[143]. A typical installation of the proposed energy storage system for a 550 MW plant would require a much smaller vessel, on the order of 100-1,000 m^3 with an effective liquid volume storage efficiency of 99.85 % over a 3 day period. Less than 1 % of the total CCC ES energy losses will be from evaporation during storage[144].

One of the concerns with any multi-component refrigerant system is the change of refrigerant composition with time causing performance variations due to changing thermodynamic properties. While this concern must be continually addressed, the natural gas is removed and replaced with operation and thus will not suffer from unequal refrigerant losses seen in a closed-loop refrigeration process. Also, due to the range of acceptable natural gas compositions that are produced and can be supplied, the design of the natural gas systems must be tailored to compositions that can be supplied on a long-term contract.

5.2 Experimental Results & Discussion

The critical process units for CCC ES demonstration are the CO_2 desublimating heat exchanger and subsequent separations. The CCC ES apparatus discussed earlier (see Figure 4-4

and Figure 4-5) provides a demonstration with a synthetic flue gas flow rate of 1.4 m^3/min. Experimental runs lasting several hours demonstrate both the desublimating column and separations.

During experimental demonstration, the system allows samples to be taken prior and post filter press for imaging solid CO_2 particles, see Figure 5-4. The solid CO_2 particles that form are porous, filamentary structures. However, during the filter press, the solid CO_2 particle density increases. Bench-scale experiments achieve separation with 2.6 % of the contact liquid remaining in the solid CO_2. To achieve the separation necessary for 99.94 % recovery of contact liquid, a standard flash drum is used after the solid CO_2 stream melts and warms. With the addition of the flash drum, less than 0.1 % of the contact liquid is lost, and the CO_2 meets specifications for EOR and sequestration.

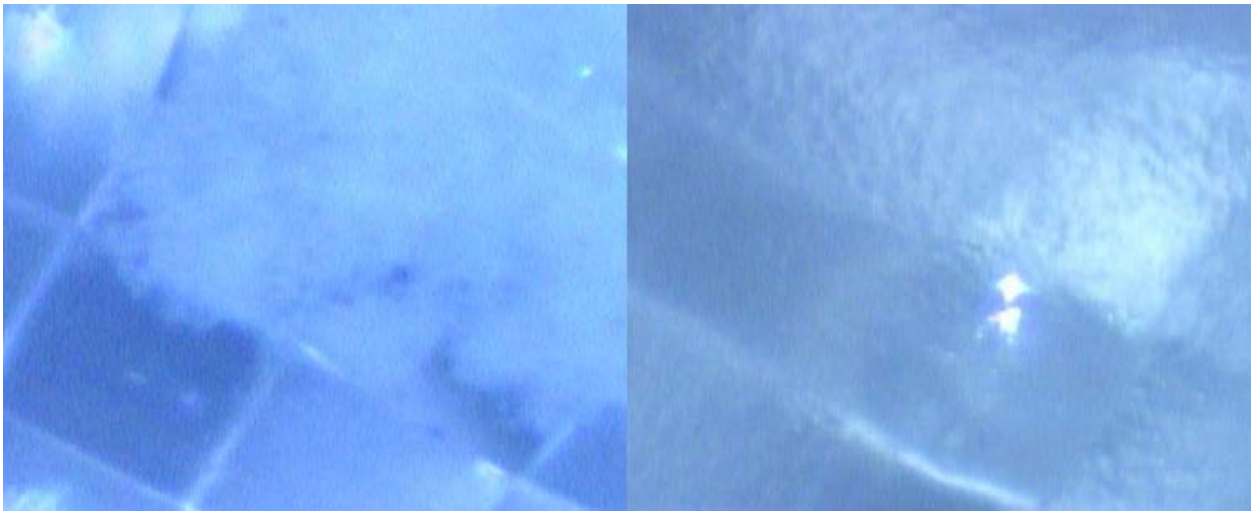

Figure 5-4 Solid CO_2 particle pre- and post-filter press (165 µm mesh wire diameter)

The operability and thermodynamic predictions of solid CO_2 formation draw on experiments with synthetic flue gas flow rates ranging from 0.02-1.4 m^3/min (i.e. up to a 20 kW_e equivalent retrofit plant). Figure 5-5 shows the experimental measurements of an hour-long run at 1.4 m^3/min with hydrocarbon 3 as a contact liquid. The prediction uses the PR-EOS with uncertainties from temperature and pressure measurements. The CO_2 concentration was measured with the EL3040, and the target 0.2 % CO_2 in the exit gas represents 98.7 % CO_2 capture. While the prediction adequately describes the CO_2 measured for the first 85 minutes, there is a departure after 85 minutes due to heat losses and other experimental design features that have since been corrected. Longer runs have been performed on the same equipment, meeting target capture of 90+ % for over 4 hours continuously. The experimental results from this and many other runs validate the ability of the PR-EOS to describe the conditions necessary for full-scale demonstration of solid CO_2 formation in the CCC ECL process.

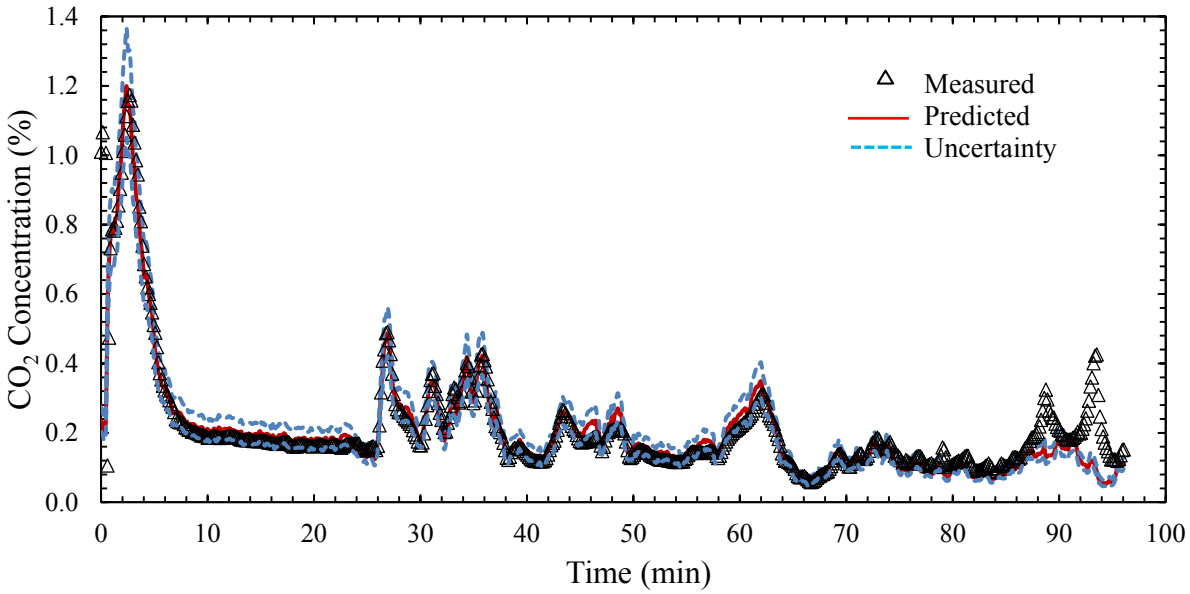

Figure 5-5 ***Experimental results of CO_2 concentration in exiting flue gas while operating near atmospheric pressure and 133-153 K with inlet composition of 15 % CO_2, balance N_2***

5.3 Full-scale Process Simulation

This embodiment of the CCC process presents a retrofit option to remove 90 % of the CO_2 from the flue gas of a coal-fired power plant with 550 MW_e net output prior to addition of CO_2 capture. The cryogenic carbon capture begins with cooling the power plant's flue gas, post desulfurization, to 175 K. The CO_2 in the flue gas forms into solid particles as the flue gas cools to 154 K in a staged column with hydrocarbon 3 acting as a contacting liquid. The clean flue gas warms against the incoming flue gas and vents to the atmosphere. The CO_2/hydrocarbon 3 slurry undergoes filtration and subsequently the nearly pure solid warms to 233 K and flashes to provide a CO_2 rich product. The CO_2 liquefies and is pressurized for enhanced oil recovery (EOR) or sequestration. All hydrocarbon 3 streams cool and recycle back to the staged column. An internal refrigeration cycle with CF_4 transfers heat from melting CO_2 to desublimating CO_2. An external cooling loop of natural gas provides the additional heat duty to operate the cryogenic process. The streams and equipment discussions appear separately below. A full process flow diagram and stream table are available in the appendix. Figure 5-6 shows a simplified process flow schematic.

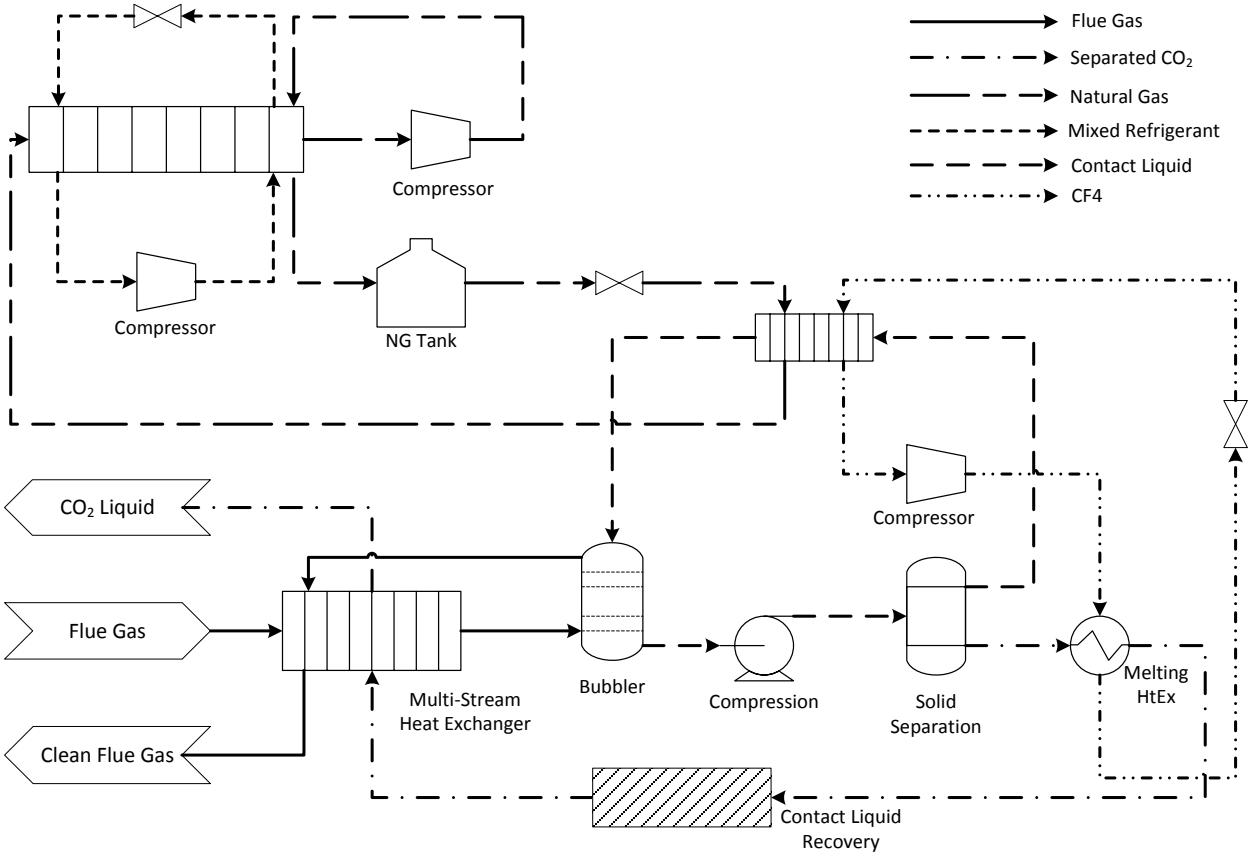

Figure 5-6 Simplified schematic of CCC ECL process flow

5.3.1 Flue Gas

Due to the potential formation of sulfuric acid and solid sulfur products, the CCC process uses gas after the power plant's flue gas desulfurization unit (FGD). The CCC process has great potential as a sulfur removal device as well as a CO_2 mitigation system, and sulfur removal has been demonstrated many times to be very efficient, but the focus here is on CO_2. The flue gas from the FGD is composed of 2.4 % O_2, 68.08 % N_2, 13.53 % CO_2, 15.17 % H_2O, and 0.82 % Ar at 330.15 K and 102.042 kPa. By first cooling the gas down to 290 K, approximately 90 % of the water content is condensed and removed. To overcome subsequent pressure drops, a blower pressurizes the flue gas to 127.6 kPa. The flue gas cools to near 273 K and regenerating mol sieve

beds remove the residual water to ensure no ice formation as the flue gas cools in a multi-stream heat exchanger down to 175 K. The cooled flue gas enters the bottom of a 10-stage desublimating heat exchanger and bubbles up through the tower, cooling to 154 K by direct contact with hydrocarbon 3. The cleaned flue gas leaves the top of the heat exchanger with less than 10 % of the incoming CO_2. It is possible to capture 99+ % CO_2 with colder temperatures (144 K), and this has been demonstrated many times. However, in this simulation, the DOE benchmark of 90 % CO_2 capture is used. The cleaned gas recuperatively warms against incoming flue gas. Before the stream is rejected in the stack, it augments an evaporative cooler to cool process water to near freezing temperatures.

5.3.2 Contact Liquid

The contact liquid is in a closed loop with minor losses into the CO_2 byproduct and the cleaned flue gas. In this simulation, hydrocarbon 3 was selected as the contacting liquid due to its low cost and low freezing point of 113.25 K[100]. However, other contact liquids have been used experimentally with lower vapor pressures to decrease losses through evaporation. The contact liquid is primarily used to prevent CO_2 solids from forming on surfaces, thus preventing process freeze up. At its coldest temperature of 154 K, the contact liquid enters at the top stage of a desublimating heat exchanger and cools the flue gas through direct contact, leaving the bottom stage as a slurry with solid CO_2 entrained in the flow. The slurry pressure increases in a pump prior to entering a solid-liquid separator. The separator consists of an auger-driven continuous filter press. The bulk contact liquid, now free of solids, recools against a closed-loop refrigeration system in preparation to reenter the desublimating column. Contact liquid is recovered from the CO_2-rich stream in a flash drum at 233 K and 550 kPa. Minor losses of hydrocarbon 3 are predicted to be 0.027 and 1.49 kg/s or 0.0025 and 0.8 % in the flue gas and CO_2 byproduct streams

respectively. To counter the minor losses, a makeup stream of hydrocarbon 3 cools and pressurizes from ambient temperature and pressure to maintain the necessary flow rate of contact liquid.

Vapor pressure data for hydrocarbon 3 is not available at the expected operation temperatures. Due to uncertainty in vapor pressure extrapolation necessary to predict the temperature required for 90 % CO_2 capture, measurements must be made to ensure compliance with hydrocarbon emission standards. In the event that hydrocarbon 3 levels are deemed too high in the N_2-rich exhaust gas, an alternative of hydrocarbon 1 and/or hydrocarbon 2 will achieve reduced hydrocarbon emissions by two orders of magnitude. Hydrocarbon 1 and hydrocarbon 2 are not simulated as the contact liquid due to their cost and viscosity disadvantages compared to hydrocarbon 3.

5.3.3 CF_4 Refrigeration

The CF_4 is included in the process as a refrigeration loop to move the cooling duty of CO_2 melting to the colder temperature of CO_2 desublimation. After condensing against the melting CO_2, and some sub cooling, it is split into five streams, each expanded by a valve to a different pressure defined by the stage of the CF_4 compressor it will be entering. This produces a stepping effect in the heat exchanger to overcome entropy losses against contact liquid and other streams undergoing sensible heating.

5.3.4 CO_2-Rich Product

The CO_2 slurry removed from the bottom of the desublimation column undergoes a separation process featuring a hydrocyclone and continuous press filter. After filtration the CO_2-rich product is 93.3 % CO_2 and is melted against condensing CF_4. After warming against the flue gas to 233 K, the CO_2-rich stream enters a flash unit for final separation (99.2 % purity). The CO_2

vapor then further warms against flue gas and compressed CO_2 before being liquefied. After liquefaction, it is pressurized with a liquid pump to 100 bar with cooling duty once again recovered before leaving the process for EOR or sequestration. Some studies suggest that a higher discharge pressure may be necessary[145-147], which case is investigated in the sensitivity analysis.

5.3.5 External Cooling

Even with the cooling duty being recovered to a high degree, further refrigeration cooling is required to operate CCC ECL. Natural gas was selected as a refrigerant due to its reasonable pressure/temperature refrigeration capability, high maturity and availability of compression, and its potential to enable energy storage. It is nominally composed of 95 % CH_4, 3 % C_2H_6, and 2 % C_3H_8. The natural gas liquefies and cools to 179 K before expanding in a turbine to 1,145 kPa resulting in a temperature of 153 K. The expansion vaporizes a significant fraction, 25.4 %, with the remaining natural gas being vaporized to cool contact liquid for subsequent CO_2 desublimation. This expanded natural gas is the coldest temperature achieved in the CCC ECL process. The natural gas then recuperatively warms against incoming natural gas before it compresses to initial conditions. A mixed refrigerant refrigeration loop is used to support the liquefaction of natural gas, and is composed nominally of 4.2 % CH_4, 84.5 % C_2H_6, 2.8 % C_4H_{10}, and 8.5 % hydrocarbon 3. Because of the heavier hydrocarbons in the mixed refrigerant, the compressor intercoolers must have a phase separator, and the liquid is removed and pressurized with a pump. Alternatively, the recirculating natural gas stream could be conditioned such that no liquids condense to simplify the compressor operation.

5.3.6 Pressurization

The flue gas blower is a single-stage compressor in Aspen Plus. The CF_4, natural gas, and mixed refrigerant compressors are 8-stage compressors with intercoolers after each stage of

compression. The CO_2 vapor compressor is modeled as a single-stage compressor with no after-cooler. Compressor intercoolers have a 5 kPa pressure drop per pass, greatly affecting the efficiency of the lowest-pressure stages. Compressors are assumed to operate with 90 % polytropic efficiency, respectively, typical of commercial guarantees for such equipment at this scale. Compressor energy consumption is the primary driver of energy penalty, and thus under great scrutiny.

5.3.7 Heat Exchange

Brazed plate heat exchangers are the primary heat exchange in the CCC ECL system. They are designed to operate with a 1 K minimum internal temperature approach. The primary CCC heat exchanger includes the flue gas sensible heating/cooling, cooling water sensible heating, CO_2-rich condensing and sensible heating/cooling, CF_4 refrigeration vaporization and sensible heating/cooling, the LNG vaporization, and the contact liquid sensible heating/cooling. This heat exchanger also handles the coldest temperatures in the process. In the heat exchanger profile, the first 80 MW are the contact liquid cooling against LNG and CF_4 vaporizing, see Figure 5-7. The LNG is a multi-component system and has a curved temperature profile, while the CF_4 is a pure component system with flat temperature profiles as it vaporizes and is thus staged. The flat portion of the profile from 120 to 170 MW is dominated by CO_2 condensing and vaporizing with some assistance from the CF_4.

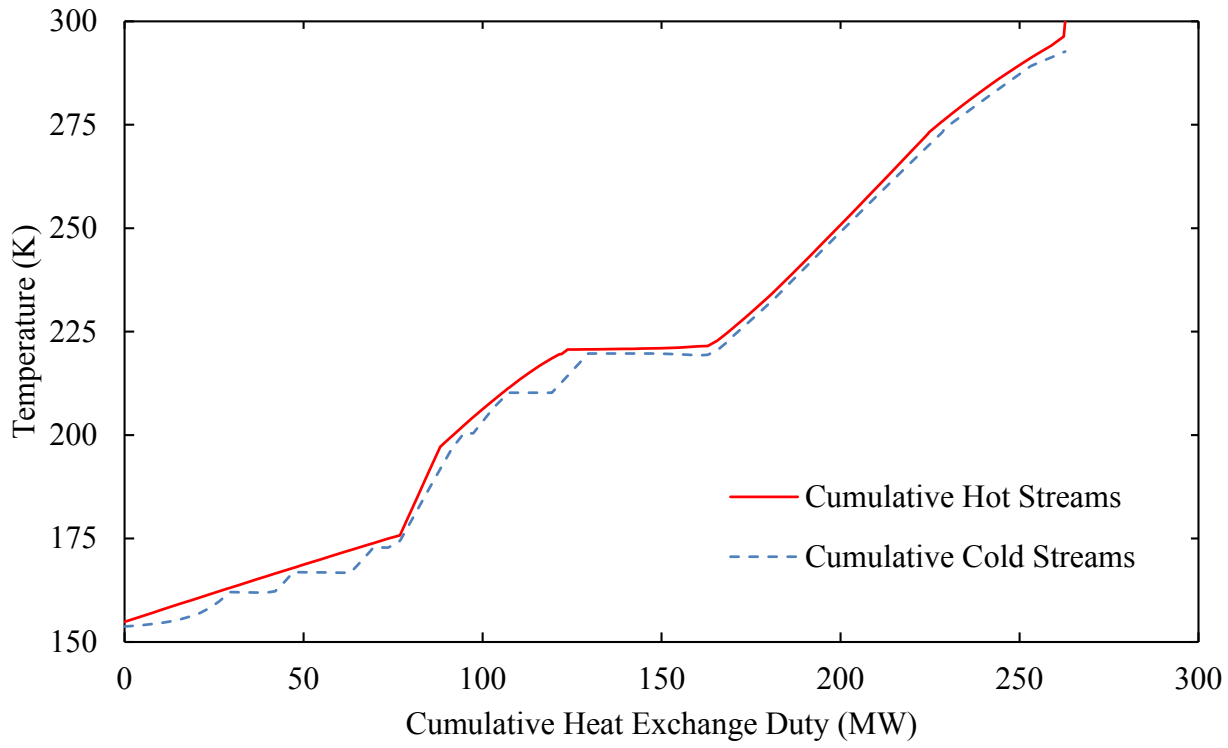

Figure 5-7 Primary CCC heat exchanger temperature (K) as a function of cumulative heat exchange duty (MW)

The natural gas liquefaction heat exchanger is a simpler heat exchanger compared to the primary CCC heat exchanger. This heat exchanger only includes the natural gas, mixed refrigerant, and cooling water. Because both the natural gas and mixed refrigerant are multi-component systems there are not the completely flat areas in the temperature profile. However, the first region of the heat exchanger from 5 to 30 MW is dominated by CH_4 condensing in the natural gas and ethane vaporizing in the mixed refrigerant, see Figure 5-8. The accompanying LNG vaporization occurs in the primary CCC heat exchanger and the mixed refrigerant condensation occurs at warmer temperatures against cooling water. The mixed refrigerant composition was chosen to best match the profiles of the hot and cold streams.

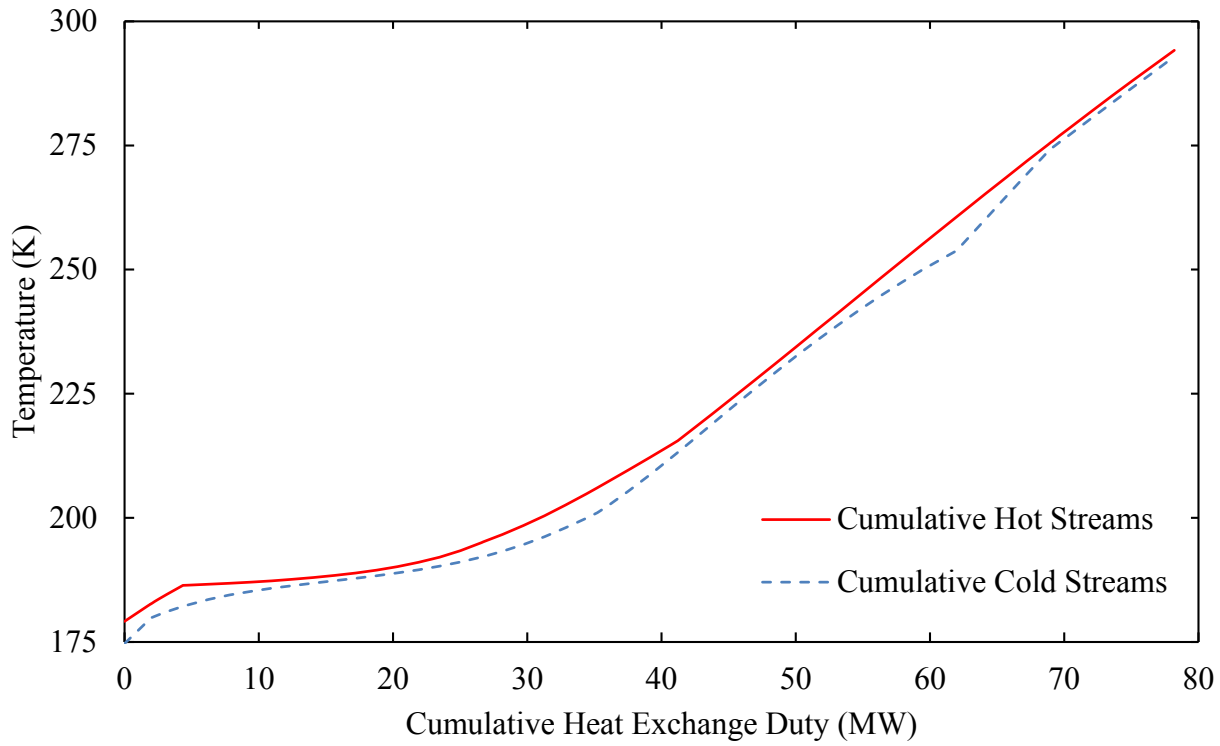

Figure 5-8 ***Natural gas liquefaction heat exchanger temperature (K) as a function of cumulative heat exchange duty (MW)***

The melting CO_2 heat exchanger is similar in design to a jacketed, stirred tank with the CF_4 condensing in the jacketing tubes while the solid melts and is stirred on the inside of the tank. A conservative approach is taken by simulating this as a co-current heat exchanger with 1 K approach temperature on the exiting streams. It is anticipated that a full-scale implementation of the melting heat exchanger would be designed for counter-current heat exchange, and thus higher efficiency.

Other, more traditional heat exchangers are used for compression inter-stage cooling and water cooling. Basic compressor inter-stage coolers are anticipated to be shell and tube heat exchangers with a minimum internal approach temperature of 5 K, though efficiency would increase and cost decrease if brazed-plate systems were used. The evaporative cooler is expected to be designed as a 10 stage cooling column. All heat exchangers have at least a 5 kPa pressure

drop per pass. Designs from Chart Energy and Chemicals suggest pressure drops ranging from 2 kPa to 19 kPa, which are included in the sensitivity analysis.

A 10 stage desublimation column was simulated with a series of Gibbs reactors, allowing solids formation at each stage. The desublimation column is anticipated to have 5 cm of liquid height per stage, resulting in a 0.37 kPa pressure drop per stage. As an alternative to a desublimation column, experimental results on a desublimation spray tower has improved efficiencies for heat and mass transfer. Up to 96 % CO_2 capture has been demonstrated and predictions of performance are within 2.3 %[148]. Pending future research and development, the desublimation spray tower may provide opportunities for lowering the total energy penalty of the CCC ECL process.

5.3.8 Solid Separation

The CO_2 solids separator is a combination of a hydrocyclone, to concentrate the solid CO_2 particles, followed by a continuous press filter, removing contact liquid down to 6.7 %. It is assumed that the press filter is capable of capturing 100 % of the solid CO_2 particles. This does not take solubility into account which may increase the concentration of CO_2 in the recycled contact liquid, but balances in a steady state mass balance.

5.3.9 Turbines

The two expansion turbines are both modeled with vapor-liquid phases. Turbines are simulated with 92 % isentropic efficiency. The turbines operate at temperatures ranging from 154-195 K and expand the hydrocarbon liquids with a portion of the stream vaporizing. LNG operations employ cryogenic hydraulic turbines that operate at nearly the same conditions and on the same

scale[149]. The turbines could be replaced by valves to reduce CAPEX with only a 2.4% increase in energy demand.

5.4 Full-Scale Modeling Results & Discussion

CCC ECL is capable of 90 % CO_2 capture with a simulated energy penalty of 0.74 MJ_e/kg CO_2. The breakdown of energy consumption is reported in Table 5-1. Three compressors drive the refrigeration and account for 80.9 % of the total energy penalty. The majority of the remaining energy penalty is due to the flue gas blower. The flue gas blower overcomes pressure drop and accounts for 16.7 % of the total energy penalty. The energy consumption of the blower may be reduced by taking advantage of lower discharge pressures in some installations. Lower discharge pressure may be achieved with improved cooling towers. The remaining power consumption is 2.4 % of the total energy penalty and thus less significant potential for improvement from an energy penalty perspective.

Table 5-1 Unit operation energy requirements

Unit	**Energy Required** [MW_e]
Blower	13.76
CF_4 Compressor	27.93
CO_2 Compressor	0.70
Natural Gas Compressor	18.55
Mixed Refrigerant Compressor	20.37
Contact Liquid and Slurry Pumps	2.21
Liquid CO_2 Pump	0.98
Mixed Refrigerant Liquid Pumps	0.11
Natural Gas Turbine	-1.38
Mixed Refrigerant Turbine	-0.63
Total	**82.59**

During electricity peak demand, stored LNG can be used as the refrigerant to drive the CCC process. The natural gas compressor, mixed refrigerant compressor, mixed refrigerant liquid pumps, and mixed refrigerant turbine can be turned down or even off to reduce the parasitic energy losses. Additionally, after the LNG vaporizes and warms it can be combusted and directed through a turbine to produce power to offset the remaining parasitic load of the CCC process.

Results from a sensitivity analysis show variations from the current base model, Table 5-2. The numerical values of these variation were chosen based on industry review of common shortcomings, available technologies, and expected technological improvements. The 4 % CO_2 inlet variation refers to a natural gas combined cycle power plant that has less CO_2 emissions per power produced. Excluding the natural gas case, the energy penalty ranges from 0.71-0.92 MJ_e/kg CO_2 captured, which is extremely competitive with other technologies.

Table 5-2 Energy penalties from sensitivity analysis. Amine case from NETL[150]

Variable	Units	Value				Energy Penalty [MJ_e/kg]		
		Base	1	2	3	1	2	3
Base Case of CCC ECL						0.738		
Amine CO_2 Capture						1.379		
CO_2 Inlet Percent	%	16	12	14	4	0.920	0.819	1.669
CO_2 Capture Percentage	%	90	89	91	99	0.711	0.740	0.846
Cooling Water Temp	K	289	281	303		0.717	0.772	
Turbine Efficiencies	isen%	92	89	94		0.738	0.737	
Approach Temperatures	K	1	2	4		0.772	0.863	
Pressure Drop	kPa	5	Per Quote			0.832		
CF_4 Compressor Efficiency	poly%	90	85	92		0.752	0.732	
NG Compressor Efficiency	poly%	90	85	92		0.747	0.734	
MR Compressor Efficiency	poly%	90	85	92		0.748	0.733	
Blower	poly%	90	85	92		0.745	0.734	

If a higher pressure is required for EOR or sequestration as suggested by some studies[145, 147], the energy penalty would increase by 0.004 MJ_e/kg CO_2. Without the turbines on the liquid natural gas and mixed refrigerant streams, the process loses 2.1 MW_e, the energy penalty would increase by 0.016 MJ_e/kg CO_2.

Table 5-3 details the total energy balance, including the previously discussed 82.6 MW_e of power consumed by process equipment. Process losses match the heat in/out of the plant and are less than 0.27 % of total heat, as benchmarked by NETL[150].

Table 5-3 Energy balance of full-scale CCC ECL simulation

	Sensible + Latent	**Power**	**Total**
Heat In	**[MW]**	**[MW]**	**[MW]**
Flue Gas	-1860.4		-1860.4
Makeup Contact Liquid	-3.8		-3.8
Cooling Water	-13426.4		-13426.4
Process Units		82.6	82.6
Totals	**-15290.6**	**82.6**	**-15208.0**
Heat Out			
Cooling Water	-14252.9		-14252.9
N_2-Rich Gas	-178.7		-178.7
CO_2-Rich Liquid	-1037.1		-1037.1
Water Condensate 991	157.0		157.0
E416A	-28.2		-28.2
E416B	29.2		29.2
E416C	-0.9		-0.9
C306 Cooling Water	32.7		32.7
C570 Cooling Water	21.4		21.4
C700 Cooling Water	44.2		44.2
Process Losses*	5.4		5.4
Totals	**-15208.0**	**0.0**	**-15208.0**
Difference			**0.0**

Table 5-4 breaks down the mass balance based on the full-scale simulation. The total mass balance closes within 0.01 %.

Table 5-4 Mass balance of full-Scale CCC ECL simulation (flow rates in kg/hr)

In	**O_2**	**N_2**	**CO_2**	**H_2O**	**HC3**	**Ar**	**Total**
Flue Gas	57726	1433810	447670	205464	0	24608	2169278
Makeup HC3	0	0	0	0	5483	0	5483
Water	0	28	44	3020154	0	0	3020226
Total	**57726**	**1433838**	**447714**	**3225618**	**5483**	**24608**	**5194987**
Out	**O_2**	**N_2**	**CO_2**	**H_2O**	**HC3**	**Ar**	**Total**
N_2-Rich Gas	57726	1433782	43834	17439	72	24608	1577461
CO_2-Rich Liquid	0	0	403836	0	5339	0	409175
Water	0	56	88	3208179	0	0	3208323
Total	**57726**	**1433838**	**447758**	**3225618**	**5411**	**24608**	**5194959**
Rel. Difference	**0.000**	**0.000**	**0.000**	**0.000**	**0.003**	**0.000**	**0.000**

Some hydrocarbon 3 in the system is lost during direct contact with the flue gas and during CO_2 separation in a flash drum. The concerns are primarily the environmental and economic impact of the combined losses. As simulated, the hydrocarbon 3 present in the exhausted N_2-rich gas is acceptable by EPA source guidelines for hydrocarbon emissions. Hydrocarbon 3 in the CO_2-rich stream is of lesser environmental concern since hydrocarbon 3 exists in the ground where the CO_2 will be used for EOR or sequestration. The economic impact of the hydrocarbon 3 losses are not fully known as the full-scale implementation of CCC ECL will likely change the economics of supply and demand for hydrocarbon 3. However, hydrocarbon 3 is sourced from oil and gas fractionation, with potential supplies greatly outweighing any potential need. If economic losses are significant, other hydrocarbons such as hydrocarbon 1 and hydrocarbon 2, have been tested as alternative contacting liquids that have lower vapor pressures and thus result in much smaller losses.

An economic analysis on the process used the same scenarios as the energy sensitivity analysis. All equipment prices came from Aspen Plus' built in economic analysis, excluding multi-stream heat exchangers. General pricing for compressors was confirmed with quotes from Elliott Group. A price quote from Chart Energy and Chemicals provides the basis for the multi-stream heat exchangers in the model. Deviations from the base scenario were assumed to have a price difference equal to 86 $/m^2 multiplied by the change in heat transfer area. The change in heat transfer area assumed that U and ΔT were constant in the equation

$$Q = UA\Delta T \qquad (49)$$

where U is the heat transfer coefficient, A is the heat transfer area, ΔT is a correlation for the temperature difference inside a plate and frame heat exchanger, and Q is the heat duty. $U\Delta T$ is the quotient of the heat duty calculated by Aspen Plus for the base case and the area for the heat exchanger as determined by Chart. This value determined the new area with heat duties calculated by Aspen Plus for each scenario. Table 5-5 shows the capital expenditure (CAPEX) attributed to carbon capture, energy penalty, and cost of electricity (COE). It is important to note that the 4 % CO_2 inlet case refers to a natural gas power plant and is the cheapest scenario in the analysis, but has the highest energy penalty because 90 % of CO_2 is being removed from a 4 % CO_2 inlet.

Table 5-5 Economic analysis of process variations and resulting cost of electricity (COE) for full-scale CCC ECL with 90 % CO_2 capture

Case / Variable	Base Case	Variation	CAPEX [$x10^6$]	Energy Penalty [MJ_e/kg CO_2]	COE [cents/kWh]
Base CCC ECL Case			361	0.738	8.96
CO_2 Inlet	16 %	4 %	217	1.669	6.67
		12 %	345	0.920	8.74
		14 %	357	0.819	8.89
CO_2 Capture	90 %	89 %	359	0.711	8.93
		91 %	365	0.740	9.03
		99 %	391	0.846	9.45
Cooling Water Temp	289 K	281 K	362	0.717	8.97
		303 K	367	0.772	9.06
Efficient Turbines[A]	92 %	89 %	364	0.738	9.00
		94 %	366	0.737	9.07
HX Temp Approach	1 K	2 K	318	0.772	8.88
		4 K	299	0.863	8.95
Pressure Drop	5 kPa	Mfg Quote	369	0.832	9.16
Compressor Efficiency[B]	90 %	85 % CF_4	363	0.752	9.02
		92 % CF_4	362	0.732	8.99
		85 % NG	363	0.747	9.01
		92 % NG	362	0.734	8.99
		85 % MR	363	0.748	9.01
		92 % MR	362	0.733	8.99
Blower Efficiency[B]	90 %	85 %	363	0.745	9.01
		92 %	362	0.734	8.99

*Without CO_2 capture the COE is 5.89 cents/kWh.

**Amine based CO_2 capture has a CAPEX of $469 $x10^6$, energy penalty of 1.379 MJ_e/kg CO_2, and COE of 10.65 cents/kWh[10].

[A]Turbine efficiencies are isentropic.

[B]Compressor and Blower efficiencies are polytropic.

5.5 Summary

Cryogenic carbon capture can be modified to yield a superior integrated energy storage and carbon capture for a coal fired power plant. CCC ES has the ideal attributes of (1) stores and releases energy with high efficiency and reasonable cost, (2) installation size on order of 100 MW,

(3) no geographical constraints, (4) absorbs demand/production intermittency, and (5) bolt-on energy storage for new or existing power plants.

Steady state CCC ES has been simulated for retrofit of a 550 MW_e coal-fired power plant. Equilibrium predictions of solid CO_2 formation have been experimentally validated on both lab- and skid-scales. Basic operation has been demonstrated with 90 % CO_2 capture on flue gas streams as high as 1.4 m^3/min. The CO_2 stream produced by the CCC ES process has a relatively high purity of 99.2 % CO_2. The emissions of volatile hydrocarbons from CCC ES meets current EPA source emission guidelines and total contact liquid losses should not be economically constraining.

The energy penalty for 90 % CO_2 capture is estimated at 0.74 MJ_e/kg CO_2 captured. Reasonable best and worst case scenarios are between 0.71-0.92 MJ_e/kg CO_2 captured. The energy penalty is estimated at 1.67 MJ_e/kg CO_2 captured in the case of CCC ECL implementation for a natural gas combined cycle power plant (4 % CO_2 inlet concentration). The cost of the CCC ES process is estimated at $361 MM Capex. The financial result is an increased cost of electricity in the range of 2.85-3.56 cents/kWh. The energy and cost numbers compare very favorably with alternative systems, and the energy efficiency is within compressor and heat exchanger efficiencies and line losses of being the minimum energy for separation. Additionally, it is anticipated that the entire energy storage system can operate on a timescale of minutes and directly offset the problems associated with renewable energy intermittency.

6 NATURAL GAS PROCESSING WITH CCC (CCC NG)

Natural Gas Processing by Cryogenic Carbon Capture (CCC NG) is a derivative of the typical embodiment of cryogenic carbon capture that is used for CO_2 removal from flue gases and other oxidizing sources. The process for natural gas treatment removes CO_2 and other impurities in a more energy and cost efficient process than currently existing technologies and eliminates many of the safety, logistical, and operational issues[151]. This patent-pending technology from Sustainable Energy Solutions includes desublimating heat exchangers and heating/cooling recovery heat exchangers that efficiently remove CO_2 from gaseous streams[98, 152-157]. The process is capable of economically processing high CO_2 concentration streams and generating arbitrarily low outlet CO_2 concentration. The process economics and performance have been explored in detail both theoretically and experimentally for applications to flue gas treatment, where it exhibits substantial economic and energy advantages relative to alternatives. Theoretical analyses of the process have also been completed for producer gas and natural gas treatments. This paper reports the validity of three prediction models and presents the experimental investigations of the process for natural gas treatment in preparation for natural gas entering pipelines.

Natural Gas Cryogenic Carbon Capture (CCC NG) differs from other cryogenic processes in that it employs patented desublimating heat exchangers that operate indefinitely without fouling or slagging. CCC NG involves desublimating CO_2 from raw natural gas streams without

distillation, absorption, or stripping columns and with cooling provided by a sub-cooled liquid stream rather than a Joule-Thomson expansion of the natural gas stream. CCC NG can be operated from near ambient to typical natural gas processing pressures.

6.1 CCC NG Process Description

A simplified CCC NG process flow schematic appears in Figure 6-1. Pressurized, dried, raw natural gas cools to near its frost-point temperature (typically 193 K or cooler, depending on CO_2 content) in a conventional heat exchanger, warming the products as it cools. This heat exchanger also removes some natural gas liquids as a separate stream. The cool natural gas stream flows into the base of a desublimating heat exchanger. Several possible desublimating heat exchanger options are available, including a column with one or more stages, a spray tower, and a fluidized bed. For this project, a multi-stage heat exchanging column with a contacting liquid flowing countercurrent is proposed. Sieve plates create bubbles and high surface area between liquid and gas phases. As the gas cools in this column, CO_2 and other impurities (H_2S, HCl, SO_2, Hg, etc.) desublimate and are removed from the column as a slurry with the contacting liquid. The contacting liquid comprises C_2H_6 and other natural gas liquids. The slurry passes through hydrocyclones, filters, or other devices to separate the solids from the liquid. The regenerated contacting liquid cools against an external refrigeration loop heat exchanger and flows back into the top of the desublimating heat exchanger. The solid CO_2 product is vaporized for venting or pressurized and melted for enhanced oil recovery (EOR) or sequestration. To the extent practical and possible, the cold products warm against the incoming stream to minimize the amount of refrigeration needed in the process. One or more refrigeration cycles provide the cooling duty necessary to desublimate the CO_2 and account for the duty mismatch of various process streams.

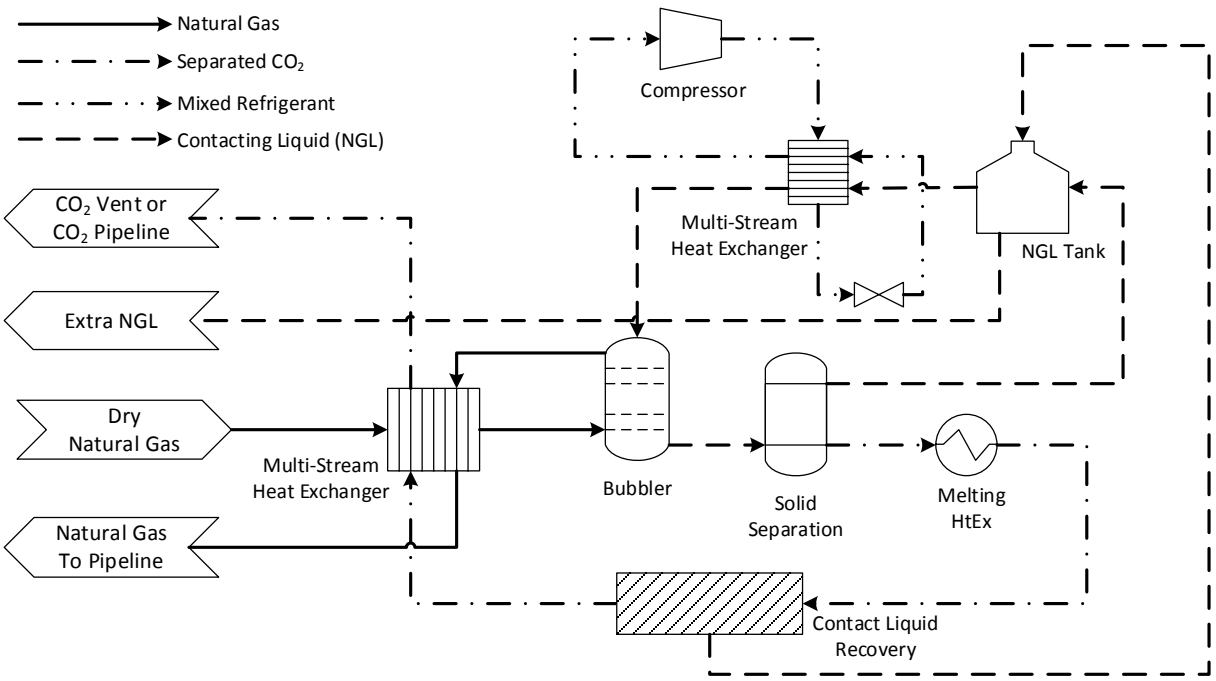

Figure 6-1 Schematic of CCC NG process flow for producing pipeline quality natural gas (2-4 % CO_2)

The process operates at plant inlet pressures with only minor pressure losses. For typical wellhead compositions, CO_2 concentration reaches the target 2-4 % pipeline specification before methane forms a liquid. If high pressures are necessary or preferred, such that the desublimation temperature of CO_2 drops to or below the condensation temperature of methane, subsequent heat transfer systems must accommodate methane evaporation in addition to solid CO_2 melting and vaporization. This process decouples heat exchange from separation, increasing the range of operating conditions in the desublimating heat exchanger. Compared to conventional CO_2 removal processes, this process does not require changes in process pressure and does not involve condensation or reboiling in a distillation column. It also combines what currently are several separation processes into a single process. These features decrease overall energy losses, capital and operating costs, and complication.

6.2 Experimental Results & Discussion

Results from a two-hour run demonstrate CO_2 separation from a 50 % CH_4, 50 % CO_2 gas mixture. The flow rate of mixed gas was 0.85 m^3/hr and the operating pressure was near atmospheric pressure (< 200 kPa). Some solid CO_2 remained in the contacting liquid with increasing concentration over time, helping to establish flow behaviors over a range of solids loadings. The contacting liquid was 67 % hydrocarbon 1 and 33 % hydrocarbon 2 and the temperature varied between 140 and 145 K. The gas sampling of the post treated gas showed that the stream contained between 0.3 to 0.4 % CO_2. Pure CH_4 commenced flowing into the system at 12 minutes, Figure 6-2, which produced an initial temperature spike in the heat exchanger fluid associated with sensible cooling of the methane flow. The cooler adjusted to this load and the temperatures stabilized over the following 8 minutes. The 50/50 mixture entered the system 32 minutes into the run, producing another temperature spike. In this case, both the sensible heat of the CO_2 stream and CO_2 desublimation increased the contact fluid temperature, the second being a much larger influence. The larger heat load in the fluid caused a correspondingly larger and especially longer change in contact fluid temperature (Figure 6-3). The temperature spike at 94 minutes occurred during inlet gas resampling to verify mixture concentrations. The temperature data are somewhat smoothed to remove thermocouple noise.

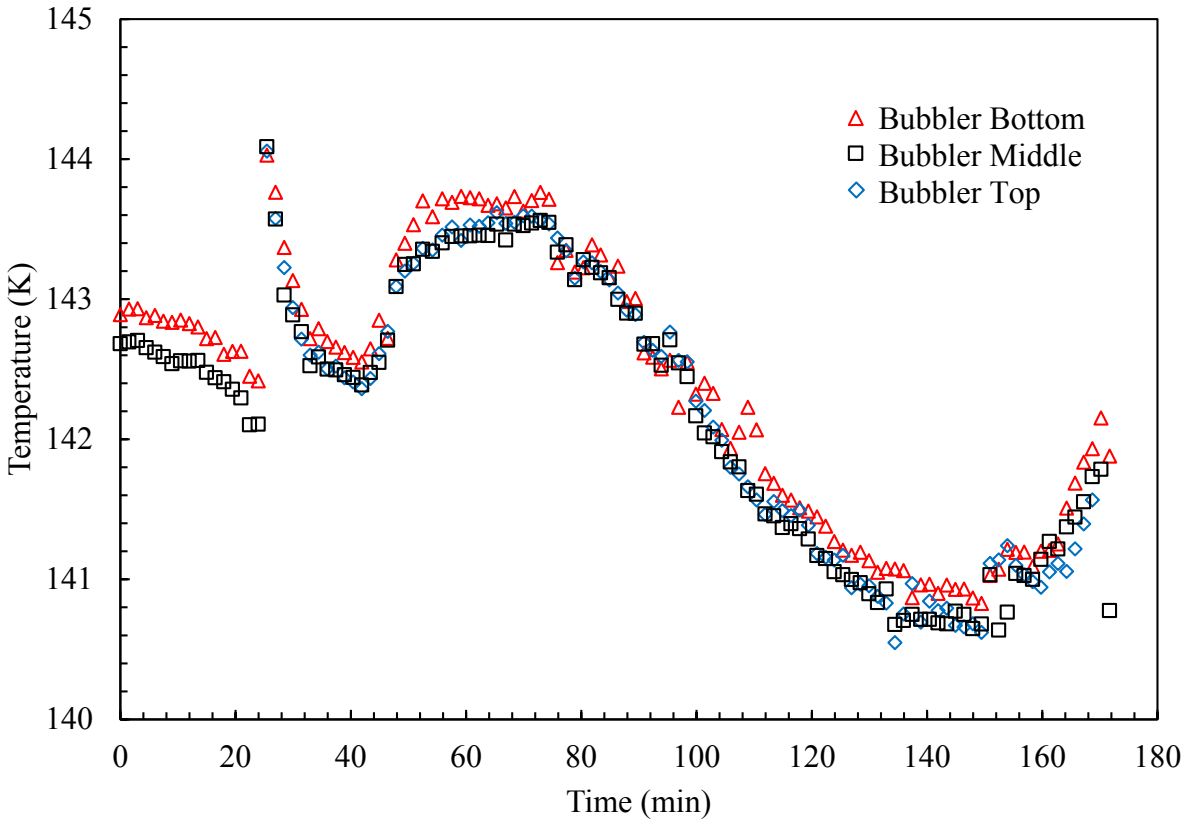

Figure 6-2 ***Temperature (K) vs. time (min) in exit stream with visually accessible desublimating column***

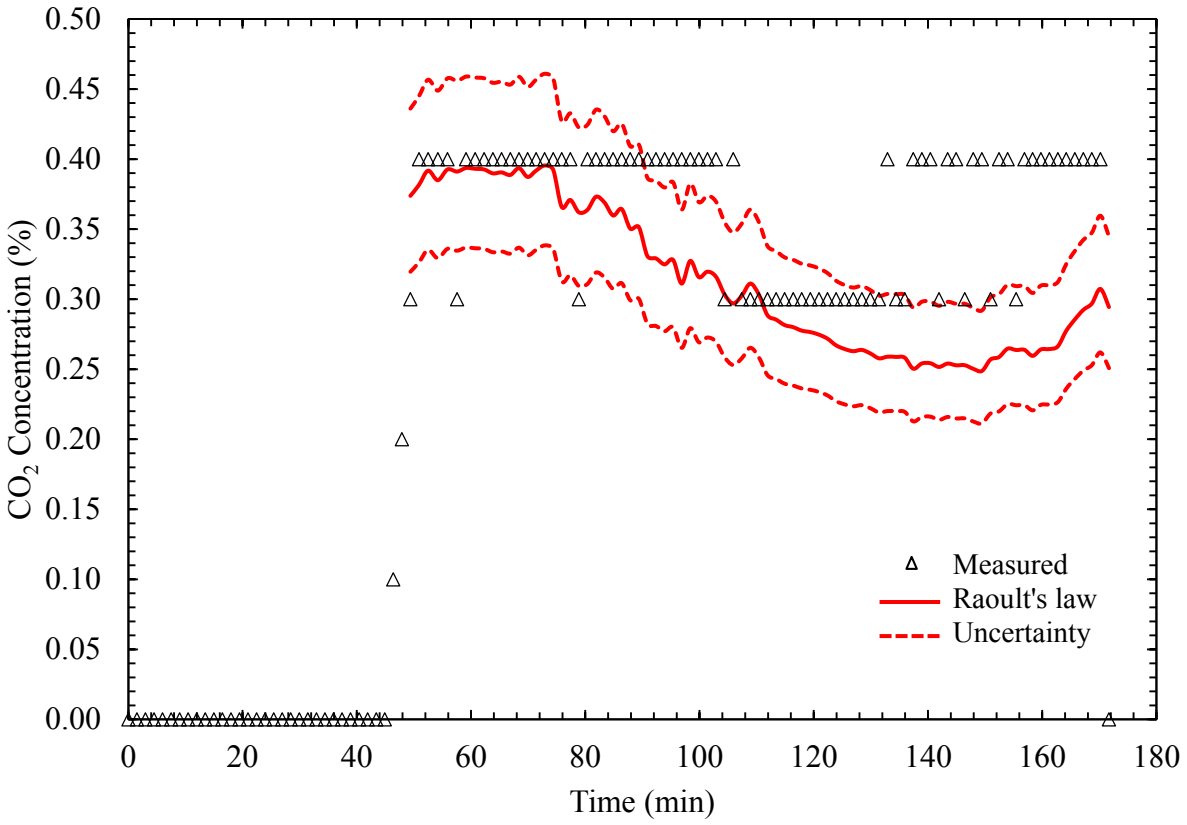

Figure 6-3 ***CO_2 concentration (%) vs. time (min) in exit stream with visually accessible desublimating column as measured with the Enerac M-700 operating at 100 kPa and 141-144 K with inlet composition of 50 % CO_2, balance CH_4. The quantized measurements result from instrument limitations***

The measured exit gas CO_2 concentrations (as percent) also appear in the graph. The illustrated data represent one measurement about every 20 seconds, which is an undersampling of the actual measurements. The raw data collection rate (60 Hz) exceeds the process and gas analyzer response times. The data over the first 30 minutes indicate zero, since only pure CH_4 was flowing through the system at that time. Beginning at about 32 minutes, when the CO_2/CH_4 mixture began to flow, the data show between 0.3 and 0.4 % residual CO_2 in the exit gas. As evident in the data,

the analyzer results of the Enerac M-700 are approaching its resolution and detection limits as it is reporting a single digit of precision.

The model predictions appear only over the range in which the process was capturing CO_2, that is, from about 30 minutes on. The predictions are based on Raoult's law. The model predictions lie within the range of data with sufficient precision to validate the experiment. Given how close these results are to the detection limit, the agreement between the experimental data and the predictions is better than expected.

Further experimental runs were carried out with the high-pressure-capable apparatus. More low pressure (< 200 kPa) runs were performed to validate performance, as seen for 2 experimental runs in Figure 6-4. The inlet composition of the gas was 45.5 % CO_2 with the balance CH_4. The CO_2 concentration was measured with the Horiba PG-250. Each run was cooled down to near 153.5 K (resulting in 1 % CO_2 in the outlet gas). The contacting liquid in these experiments was hydrocarbon 3. The change in contacting liquid did not cause any significant disturbance.

To validate the effect of an additional component, C_2H_6 was added to the inlet of an additional low-pressure run. The combined inlet gas composition was 35.1 % CO_2, 12.3 % C_2H_6, and the balance CH_4. Even with the additional component, Raoult's law is able to adequately predict the CO_2 concentration over the range of 160 to 190 K (3 to 18 % CO_2 concentration) as seen in Figure 6-5. Similar to the previous two runs, the contacting liquid was hydrocarbon 3.

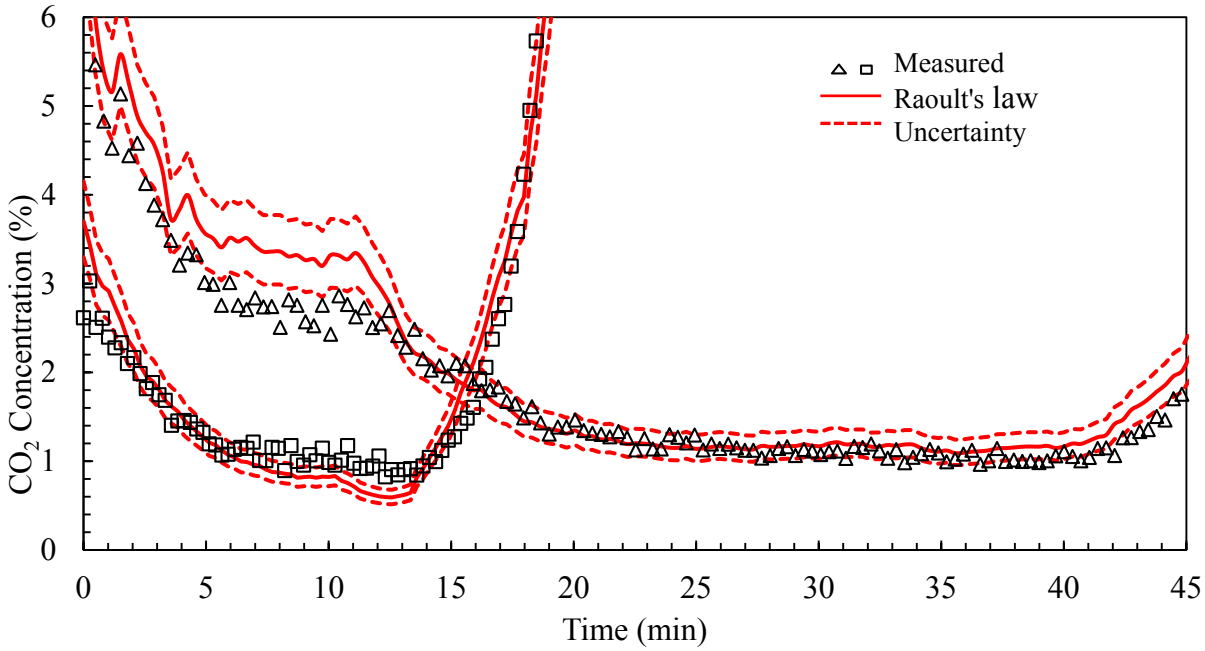

Figure 6-4 ***Exit CO_2 concentrations (%) vs. time (min) in the natural gas from two low-pressure experimental runs operating at 153-171 K and 152 kPa with inlet composition of 45.5 % CO_2, balance CH_4***

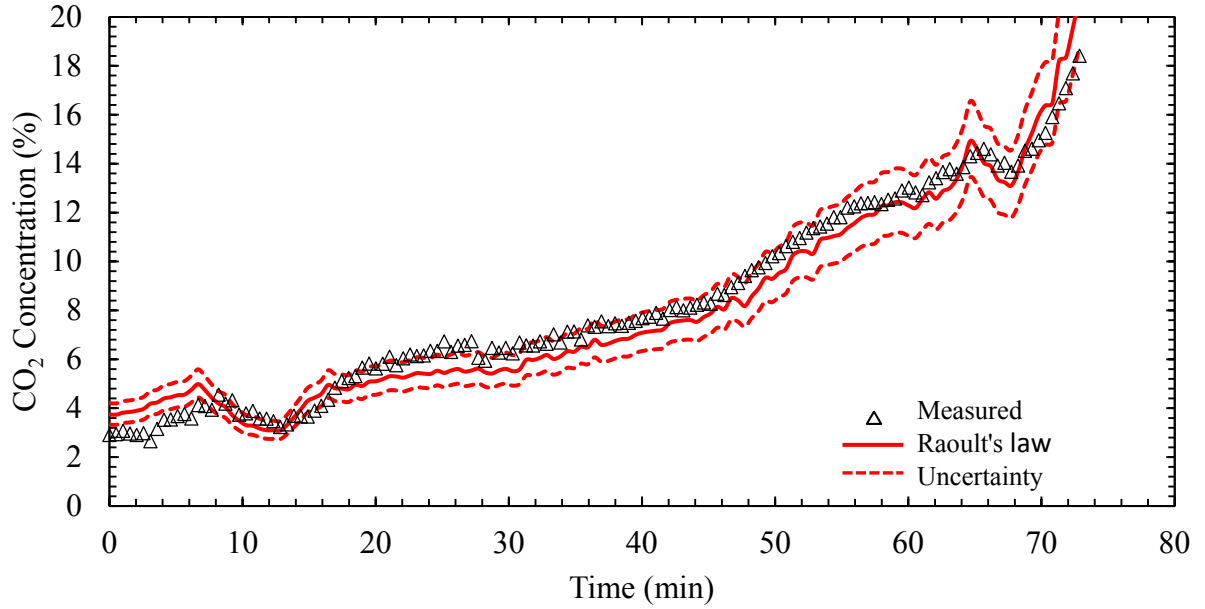

Figure 6-5 ***Exit CO_2 concentration (%) vs. time (min) in the natural gas operating at 159-175 K and 100 kPa with inlet composition of 35.1 % CO_2, 12.3 % C_2H_6, and balance CH_4***

To determine the applicability of the predictions at more elevated pressures, an additional experimental run was performed with an average pressure during the experiment of 2.19 MPa. The inlet gas was 28.6 % CO_2 with the balance CH_4. The start of the run required time for the CO_2 to equilibrate. The deviation of the measurements around 60 minutes was caused by taking the FTIR offline for an additional N_2-purge/background. Raoult's law is able to adequately predict the CO_2 concentration as seen in Figure 6-6 (medium pressure).

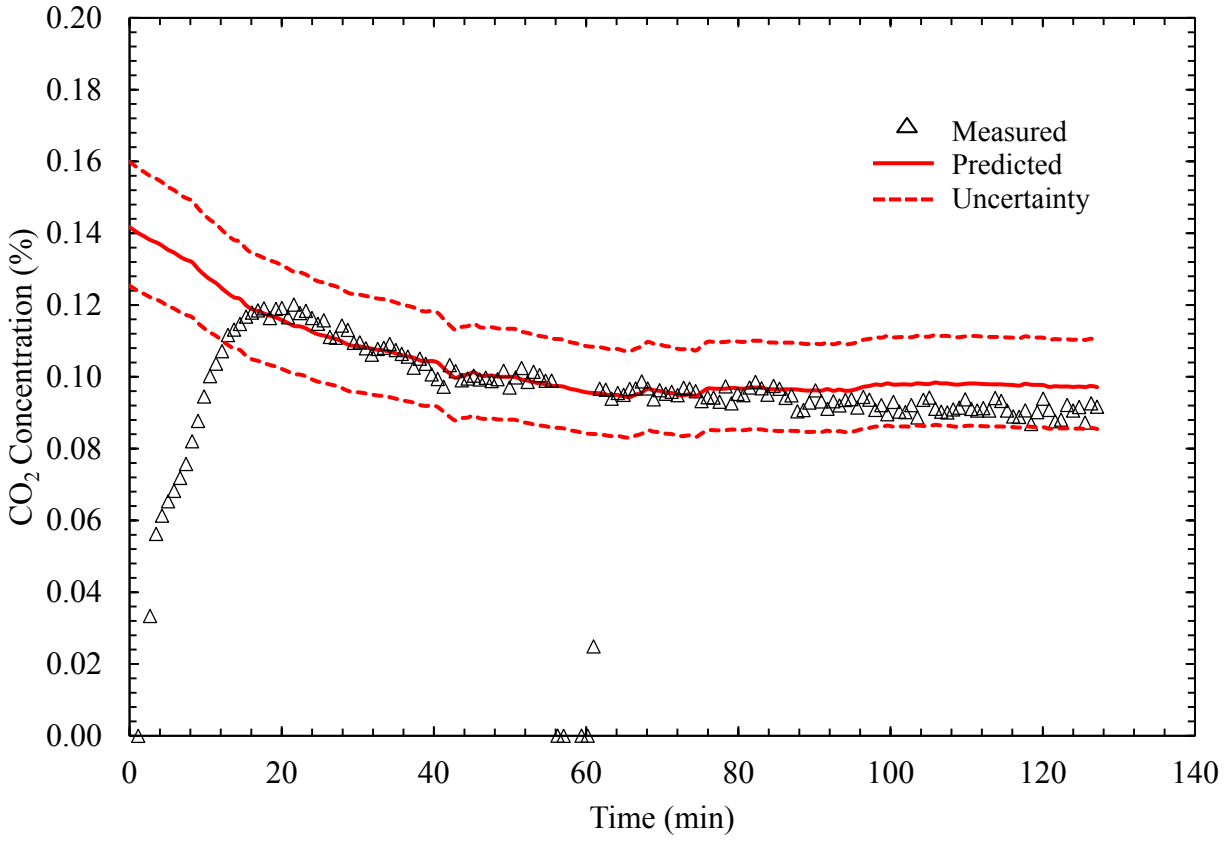

Figure 6-6 ***Exit CO_2 concentration (%) vs time (min) in the natural gas operating at 157 K and 2.19 MPa with inlet composition of 28.6 % CO_2, balance CH_4. CO_2 concentration measured with Horiba PG-250***

Natural gas treatment may be performed at even higher pressures. An experimental run was performed with an average pressure during the experiment of 3.8 MPa. This pressure is near the operating limit of the apparatus and is similar to pilot-scale demonstrations by ExxonMobil[158]. The inlet gas was 14.2 % CO_2 with the balance CH_4. The contacting liquid was hydrocarbon 2. Raoult's law is unable to adequately predict the CO_2 concentration, as seen in Figure 6-7. The number of data points was reduced to one point every 3.9 minutes. Predictions were likewise smoothed by taking an average of the temperature over the same interval. The CO_2 concentration was slow to equilibrate due to the solubility of CO_2 in the contacting liquid at high pressures. Also, the response is slow due to the constraint of mass flow rates being relatively small compared to the increased density operating at 3.8 MPa.

Another high-pressure experiment alters the pressure setpoint half way through the experiment from 3.8 to 3.1 MPa (Figure 6-8). The gas inlet conditions and temperatures of the previous high-pressure experiment are maintained, but with this reduction in pressure the CO_2 was reduced to 2 %, which is a more conservative CO_2 specification for pipelines. From the high-pressure experiments we conclude that the estimation method using Raoult's law is insufficient, while the methods using the PR and SRK EOS are adequate.

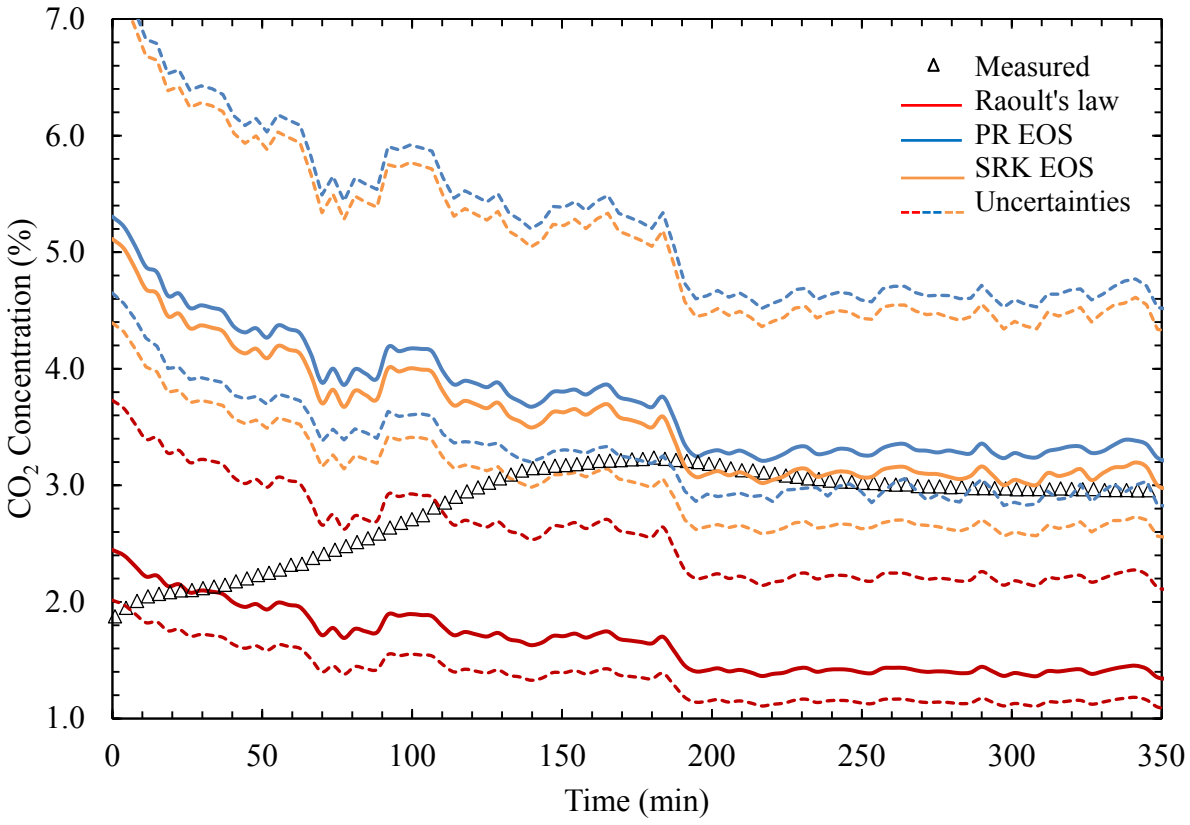

Figure 6-7 ***Exit CO_2 concentration (%) vs. time (min) in the natural gas operating at 189 K and 3.8 MPa (high pressure) with inlet composition of 14.2 % CO_2, balance CH_4. CO_2 concentration measured with FTIR***

The range of pressures between the medium- and high-pressure runs cover the operating conditions of cryogenic natural gas liquids recovery. There is a potential synergy of the cryogenic processing for natural gas liquids recovery and CCC. In the case of CO_2 concentrations presenting a potential problem with freezing out and plugging the system, the desublimating columns of this study could act as replacements for the absorbers and demethanizers used in natural gas liquids recovery. Potentially, the change to desublimating columns would be a minor incremental cost compared to the incremental cost of adding an amine absorption unit prior to natural gas liquids recovery.

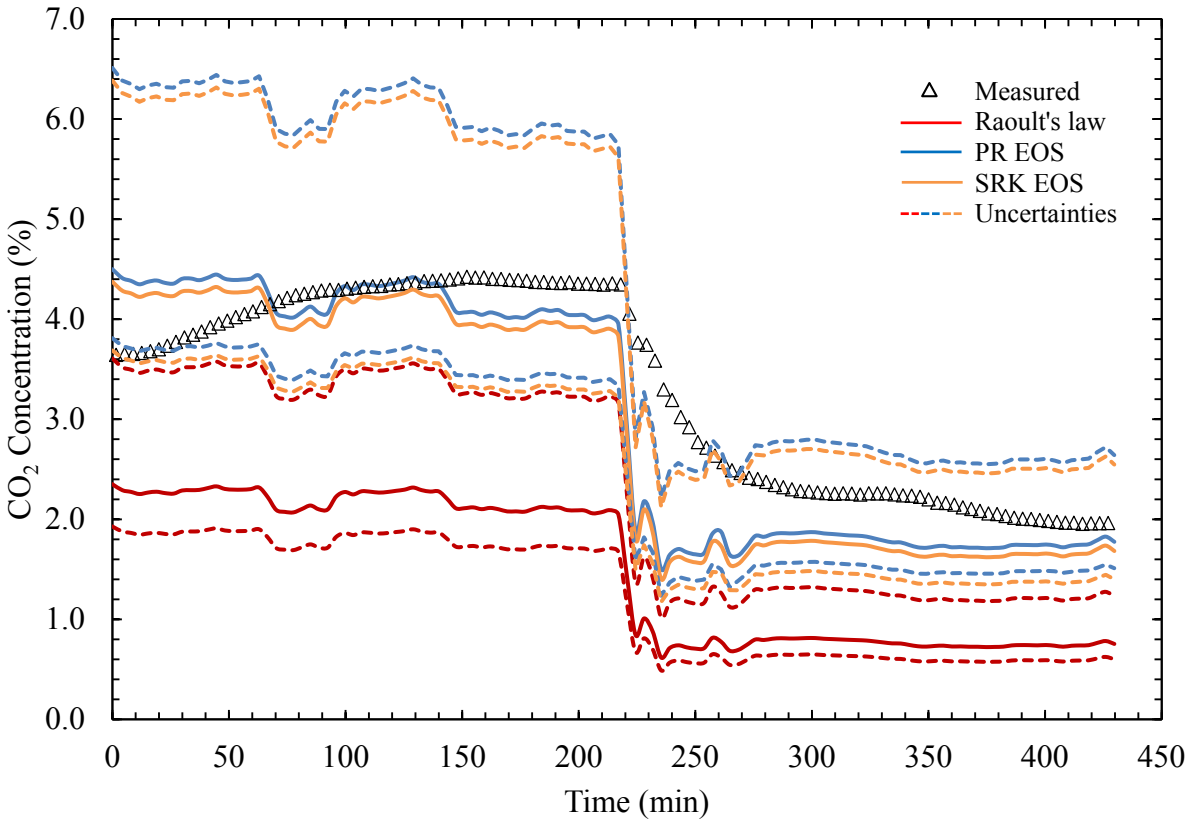

Figure 6-8 ***Exit CO_2 concentration (%) vs. time (min) in the natural gas operating at 3.8 MPa for first 220 minutes and remaining 210 minutes at 3.1 MPa. Temperature consistent during experiment at 192 K with inlet composition of 14.2 % CO_2, balance CH_4***

Additionally, the consistency of predictions and measurements suggests that CCC NG could be used for CO_2 removal down to LNG specifications (50 ppm). However, much colder temperatures would be necessary and at normal operating pressures of natural gas liquefaction, the methane component would liquefy before achieving the 50 ppm specification. Therefore, two different processing systems could be employed depending on the desired operating pressure and the liquefaction of methane. For low pressure systems (< 0.3 MPa), a typical embodiment of CCC NG could be used. For higher pressure systems (> 0.3 MPa), methane would liquefy before CO_2

could be removed below 50 ppm, with the actual amount being constrained by solubility and operating pressure.

6.3 Summary

CCC NG removes CO_2 from natural gas using processes and equipment similar to those for flue gas treatments and cryogenic natural gas liquids recovery. This process does not require pressurization or distillation of the gas stream, saving capital and operating costs and energy. It also does not involve stripping and absorption towers, though it does involve a desublimating heat exchanger. Finally, it combines several separation processes into one, simplifying the overall treatment system.

Data from the application of CCC to raw natural gas treatment indicate that the process behaves as predicted by a theoretical model based on process temperature, pressure, and gas composition and should provide a cost-effective and energy-efficient alternative to traditional gas treatments. Further, CCC NG performance is adequately predicted by PR and SRK EOS with various hydrocarbons used as contacting liquids (hydrocarbon 2, hydrocarbon 3, and C_2H_6) and the addition of a third component to the gas stream (C_2H_6). Raoult's law is adequate for low pressure predictions. CCC NG has potential application to natural gas liquids recovery and natural gas liquefaction when treating natural gas with high CO_2 concentrations.

7 NATURAL GAS LIQUEFACTION WITH CRYOGENIC CARBON CAPTURE (CCC LNG)

Globally, natural gas is an important source of energy and is becoming increasingly transportable as liquefied natural gas (LNG). For LNG processes, CO_2 concentration limits in natural gas feedstocks generally are about 50 ppm to avoid operational problems during liquefaction. In particular, CO_2 can cause conventional heat exchanger fouling by freezing and plugging the heat exchanger. Several technologies reduce natural gas CO_2 contents to these levels. Generally, these technologies pretreat natural gas streams rather than removing CO_2 during cooling and liquefaction.

Conventional CO_2 reduction processing for natural gas commonly involve amine-based solvents in absorption and stripping columns[73]. CCC LNG represents a derivative of the flue-gas-based embodiment of cryogenic carbon capture™ applied to liquefaction of natural gas. This technology has the potential to remove CO_2 and other impurities in a more energy and cost efficient process than current technologies. This technology includes desublimating heat exchangers that efficiently remove CO_2 from gaseous and liquid streams[156, 157]. The process economics and performance for flue gas applications exhibit substantial advantages relative to alternatives[8, 51]. A more recent application to natural gas processing has been explored with the Peng Robison (PR) and Soave Redlich Kwong (SRK) equations of state (EOS) used to adequately predict

performance. However, due to the potentially complex mixtures, this discussion also reviews the Predictive Soave Redlich Kwong (PSRK) EOS as a prediction tool.

This chapter details the method of producing LNG with CO_2 removal in two pressure regimes. The 50 ppm CO_2 specification, achieved in the low-pressure regime has CO_2 freeze out of the natural gas before liquefaction. For an LNG product containing more than 50 ppm CO_2, operation can occur at medium and high pressures and include freeze out from the vapor and/or liquid phases. First, the limitations of CO_2 concentration in LNG process technologies are discussed with some of the more applicable technologies to resolve these limitations. Secondly, the CCC LNG process is described in more detail with a discussion of the thermodynamics of solid CO_2 formation in natural gas over a wide range of temperature and pressure. The Peng-Robinson (PR), Soave-Redlich-Kwong (SRK), and Predictive-Soave-Redlich-Kwong (PSRK) equations of state (EOS) predict CO_2 phase behavior in the presence of natural gas. Predictions are validated with literature and original data regarding CO_2 solubility in natural gas components. Experiments are then outlined with results and discussion of the predictions and the impact on future CCC LNG development.

7.1 CCC LNG Process Description

CCC LNG involves desublimating CO_2 without distillation, absorption, or stripping columns and with cooling for desublimation provided by a direct contact desublimating heat exchanger rather than a Joule-Thomson expansion. A simplified process flow schematic is presented in Figure 7-1 for CCC LNG to remove CO_2 down to LNG standards (50 ppm CO_2). Depending on the composition of the natural gas to be liquefied, some pretreatment may be necessary to remove water and pollutants. The clean natural gas cools in a conventional heat exchanger and then expands to achieve a temperature near its CO_2 frost point in a conventional

heat exchanger and expander with any condensates being removed. The cold, low-pressure gas enters a desublimating heat exchanger. Several possible desublimating heat exchanger options are available, including a staged bubbling column, a spray tower, and a fluidized bed. This research uses a multi-stage heat exchanging column with sub-cooled natural gas liquids (NGL) flowing countercurrent as the direct contact fluid. Sieve plates create bubbles and high surface area between liquid and gas phases. As the gas cools in this column, CO_2 desublimates and forms a slurry with the NGL, eventually being removed from the column. The cold, CO_2-lean natural gas liquefies in a conventional heat exchanger.

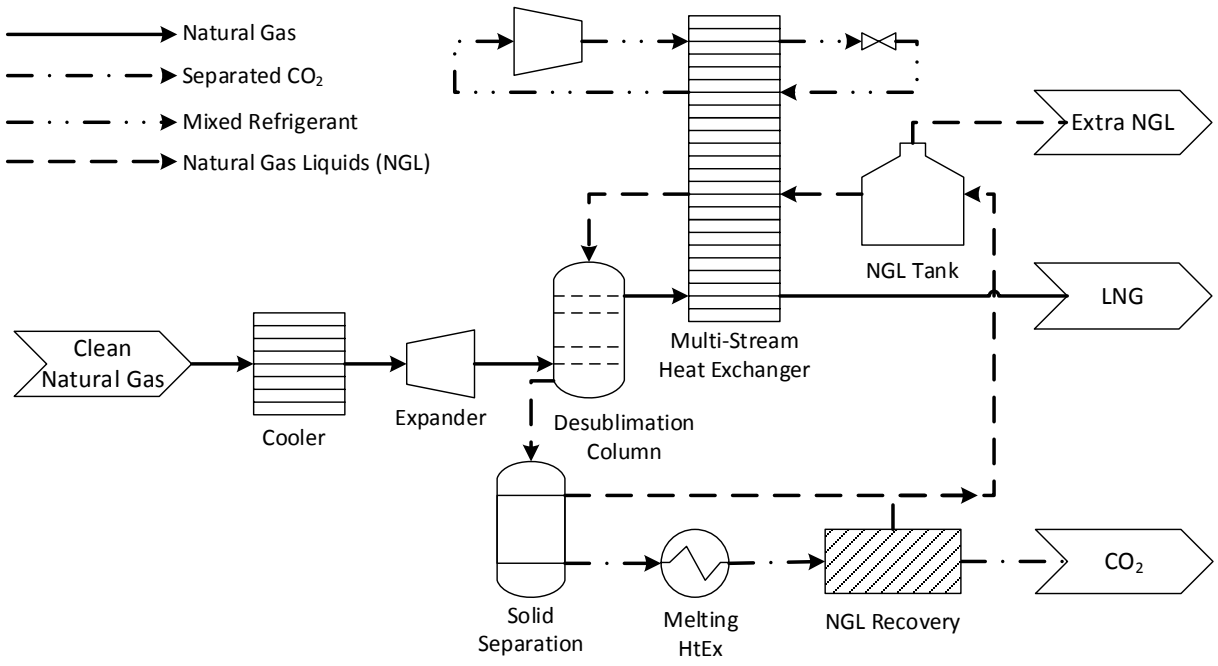

Figure 7-1 Simplified process flow diagram for CCC LNG process achieving LNG with 50 ppm CO_2

The NGL slurry with solid CO_2 is primarily composed of C_2H_6 and other light hydrocarbons in the liquid phase. Subsequent solid/liquid phase separation by hydrocyclones,

filters, or other appropriate means regenerates the contact liquid, which then cools before entering back into the top of the desublimating heat exchanger. Additional NGL forms in the desublimating heat exchanger, providing highly efficient NGL recovery as this excess flows to NGL storage or treatment. Meanwhile, the solid CO_2 product warms, with disposal options including venting, sequestration, or enhanced oil recovery. One or more refrigeration cycles are incorporated to provide the cooling duty necessary to desublimate the CO_2 and account for the available duty of CO_2 melting.

A modified process produces CO_2 concentrations greater than 50 ppm in the LNG with considerable energy savings. The primary change is expanding the natural gas after liquefaction, rather than before, as seen in Figure 7-2. By maintaining the majority of the process at high pressures, the energy intensive refrigeration can be performed at warmer temperatures. Performing the liquefaction at warmer temperatures greatly reduces the energy required. A secondary benefit is that the size of equipment decreases because of the increased density of the natural gas. The final LNG product is still generally expanded to near atmospheric pressure for storage.

Both the high- and low-pressure versions of the CCC LNG process replace an amine absorption plant in a conventional process with a desublimating heat exchanger, solid separator, melting heat exchanger, and NGL recovery flash drum. Energetically, the tradeoff is a pressure or temperature swing absorption process against the incremental refrigeration for desublimating CO_2. However, the incremental refrigeration for desublimating CO_2 is offset almost entirely in the case of venting the CO_2 by melting and vaporizing. The penalty is even further reduced in the case of LNG with 50+ ppm CO_2 because less CO_2 must be removed.

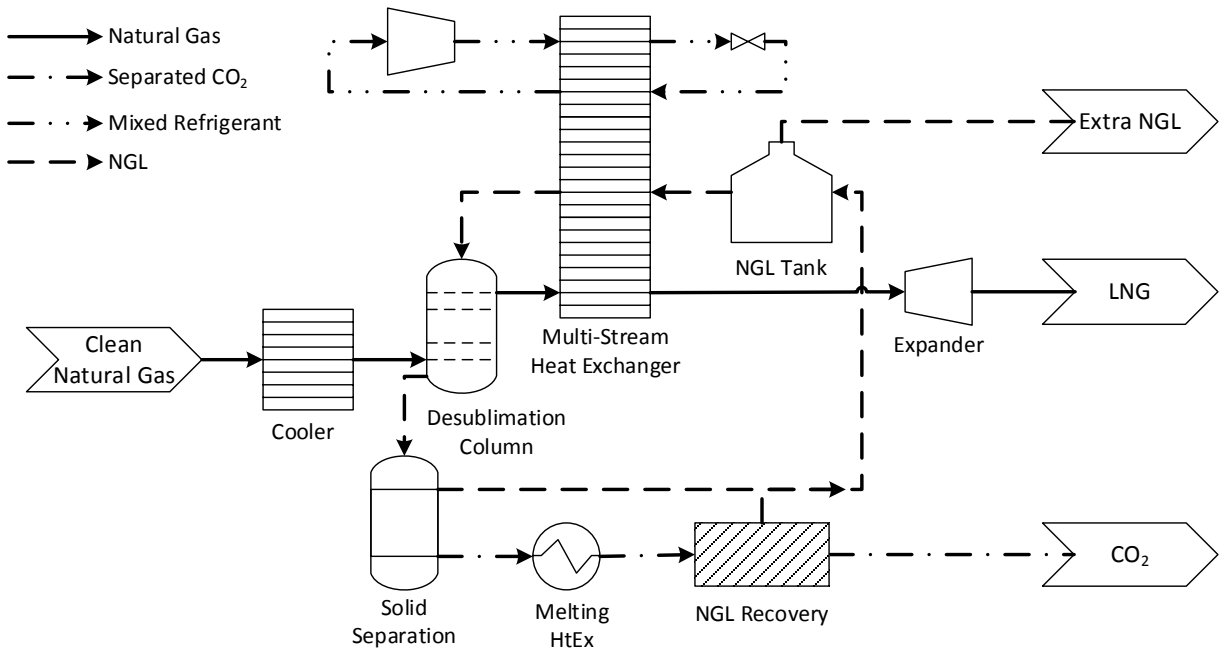

Figure 7-2 Simplified process flow diagram of CCC LNG for LNG with 50+ ppm CO_2

Both versions of CCC LNG decouple heat exchange from separation, increasing the range of operating conditions in the desublimating heat exchanger. Compared to conventional CO_2 removal processes, this process does not require changes in process pressure and does not involve condensation or reboiling in a distillation column. These features have the potential to decrease overall energy losses as well as capital and operating expenses.

7.2 Experimental Results & Discussion

Multiple runs at low pressure demonstrate CCC LNG producing natural gas near 50 ppm CO_2. All low-pressure runs had inlet natural gas containing 9.1 % CO_2 with the balance CH_4. The initial charge of contacting liquid was hydrocarbon 3. The average difference between Raoult's law and PR EOS methods is 4 ppm CO_2 near the 50 ppm CO_2 target. The 4 ppm difference is less than the average uncertainty of 7 ppm CO_2 due to uncertainty in pressure and temperature. Figure 7-3 shows the measured and predicted CO_2 concentration as predicted by the PR EOS. Almost all

CO_2 measurements fall within the uncertainty as determined from accuracies of the temperature and pressure measurements. The pressure for this experiment ranged from 266-305 kPa and is just below the threshold before CH_4 liquefies. Liquid nitrogen cools the process for experiments achieving 50 ppm CO_2. A manually operated valve controls the flow of liquid nitrogen and adjusting the valve accounts for some of the perturbations is process temperature. The pressure decrease in this and other runs is caused by gases in the apparatus condensing as the temperature decreases. However, no recorded process parameter was found to have a trend that could explain the deviation of the measurements from the prediction in the interval of 40-70 minutes.

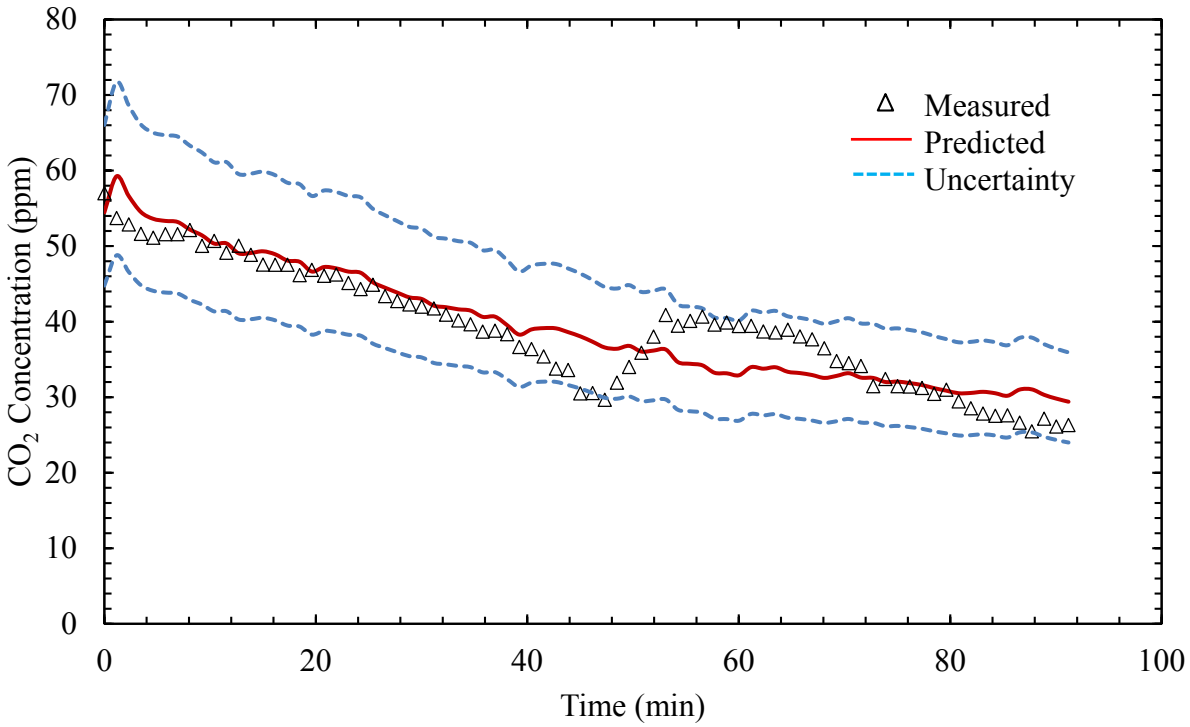

Figure 7-3 Measured and predicted CO_2 concentration (ppm) vs. time (min) at 259-293 kPa and 121.3-124.7 K with inlet composition of 9.1 % CO_2, balance CH_4

Figure 7-4 illustrates results from an experiment at 116-149 kPa, but otherwise the same conditions as the previous experiment. The lower pressure produces higher CO_2 concentrations. Once again, most of the measurements are within the uncertainty of the prediction by the PR EOS. From 20-30 minutes the gas inlet flow rate increases, causing the perturbation in the system pressure. Figure 7-5 shows results from an experiment with the same conditions as Figure 7-4 with a target of 50 ppm final CO_2 concentration. The higher pressure compensates for the warmer temperature to achieve the 50 ppm target. The cool-down period validates the PR EOS predictions at higher CO_2 concentrations. From 17-35 minutes, the contact liquid undergoes two periods of warming, see Figure 7-6. The CO_2 concentration responds slowly to the contact liquid temperature change. The slow response may result from the desublimating column maintaining its cold temperature despite the contact liquid warming or from transport effects of CO_2 bubbles leaving the viscous contact liquid. These experiments show the adequacy of the PR EOS for predicting performance when achieving the 50 ppm CO_2 target.

Higher pressure experiments involve complete liquefaction of the natural gas. The LNG samples came from the stream immediately leaving the desublimating column. Although the solid separating cartridge filter was after the sampling point, the CO_2 content in the LNG differed by less than 0.1 % from that in the liquid after the filter. Figure 7-7 shows measurements and predictions for a 7 hour experiment. During the first hour of the experiment, the CO_2 reaches saturation in the LNG. For the bulk of the experiment, the predictions by PR EOS provide the best correlation. The predictions by SRK and PSRK EOS provide reasonable estimations, with predictions of PSRK EOS being the worst. In general, the CO_2 content in this system remains quite high since the solid CO_2 dissolves in the contacting liquid to a significant extent.

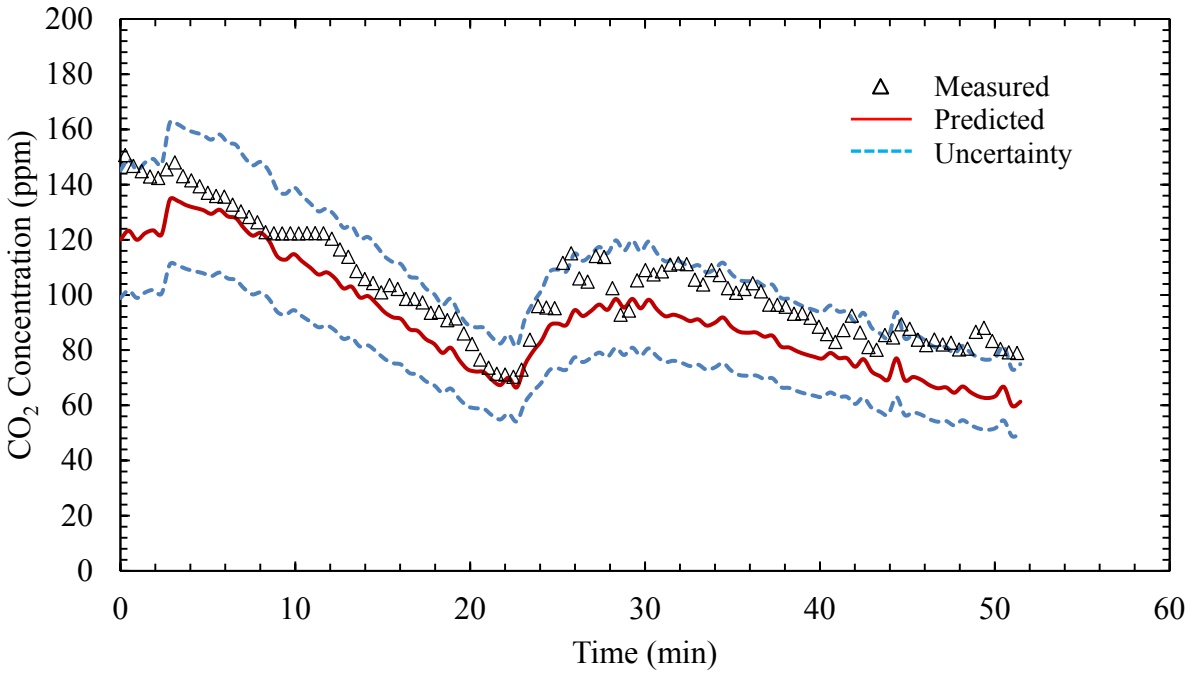

Figure 7-4 ***Measured and predicted CO_2 concentration (ppm) vs. time (min) at 116 to 149 kPa and 121.1 to 125.8 K with inlet composition of 9.1 % CO_2, balance CH_4***

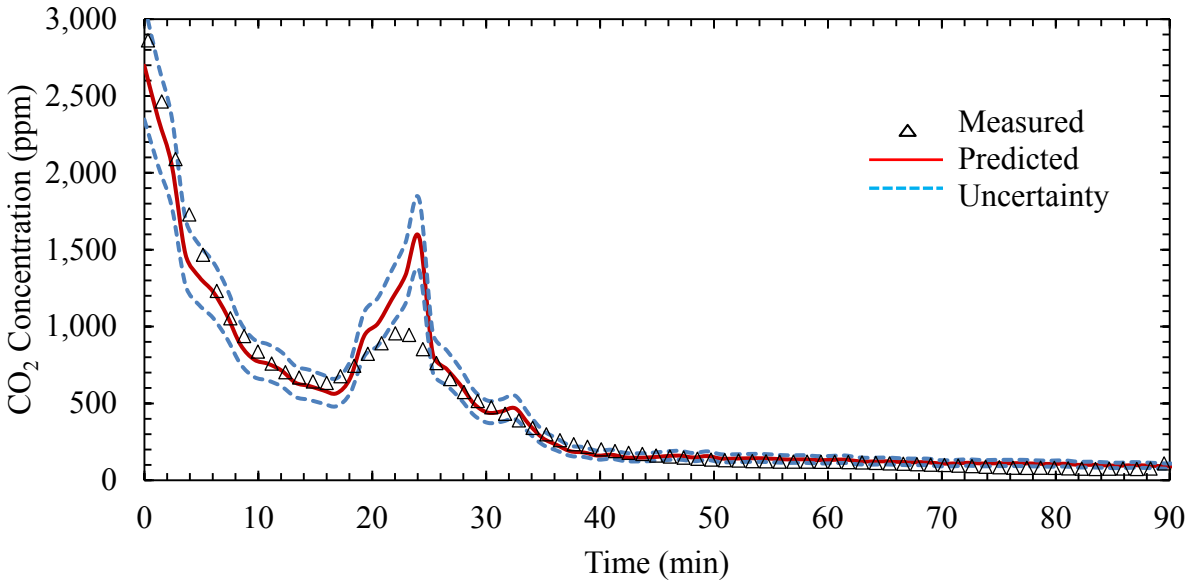

Figure 7-5 ***Measured and predicted CO_2 concentration (ppm) vs. time (min) with a 50 ppm CO_2 target showing initial cool down period from 148.8 to 126.4 K, operating at 277 to 302 kPa with inlet composition of 9.1 % CO_2, balance CH_4***

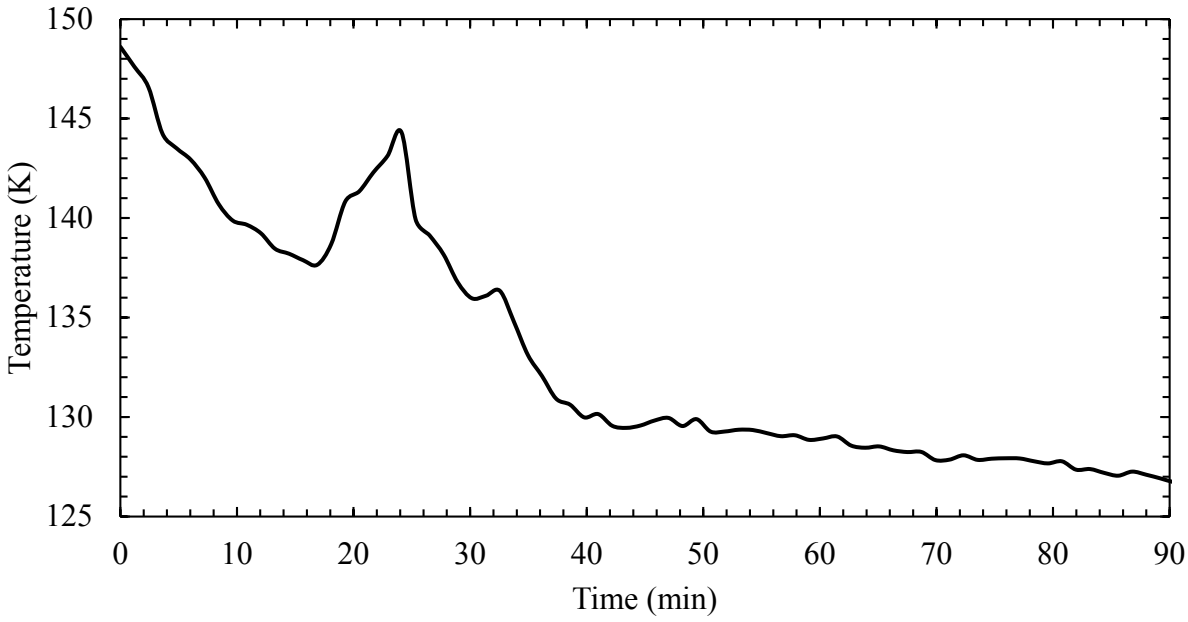

Figure 7-6 Temperature (K) vs. time (min) showing cool down period to achieve 50 ppm CO_2

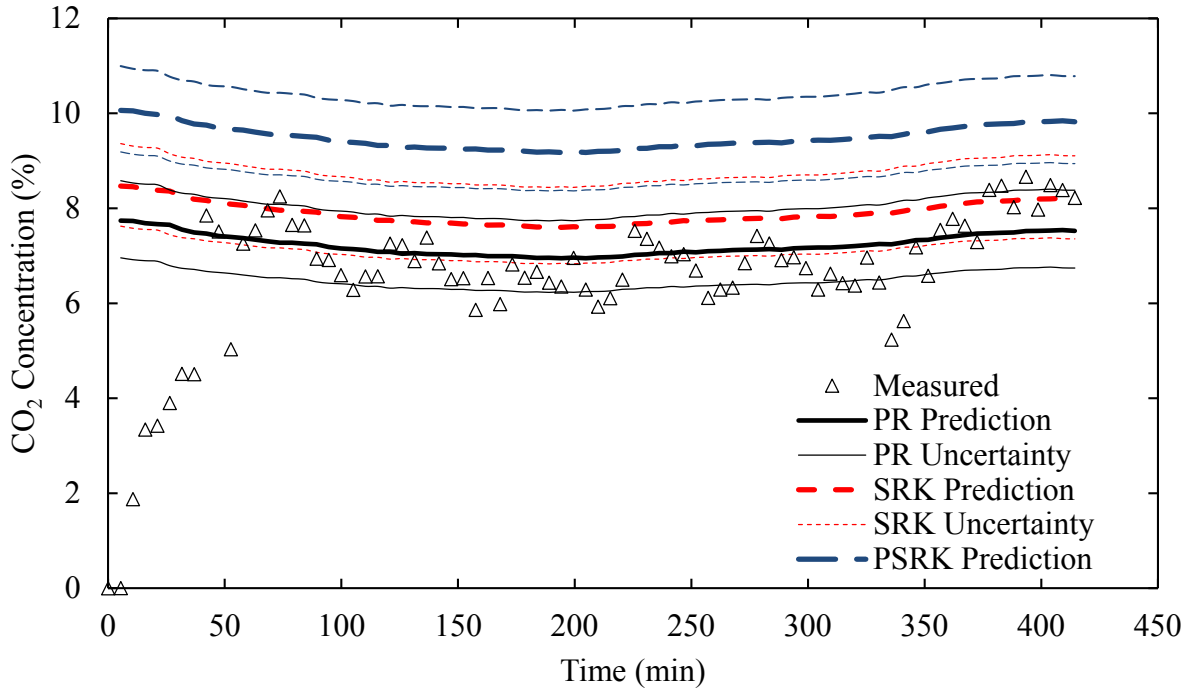

Figure 7-7 CO_2 concentration (%) results of LNG produced at high pressure (3.9 MPa) and 177 K with inlet composition of 13.5 % CO_2, 5.4 % C_2H_6, and balance CH_4

To achieve low CO_2 in condensed LNG, the LNG must be cooled to lower temperatures. Figure 7-8 shows the experimental results of CO_2 concentration in the final LNG product which meets the CO_2 specifications of less than 2 % CO_2. The apparatus only permitted cooling the LNG in a traditional brazed-plate heat exchanger. As the LNG cooled, CO_2 froze out and plugged the heat exchanger, leading to very short run durations. A future apparatus should have the potential for an alternate method of cooling CO_2-saturated LNG. This problem can be potentially overcome through a host of processing techniques, and is not the focus of this paper, but does provide a limitation of the applicability of this apparatus for low-CO_2, high-pressure CCC LNG operation.

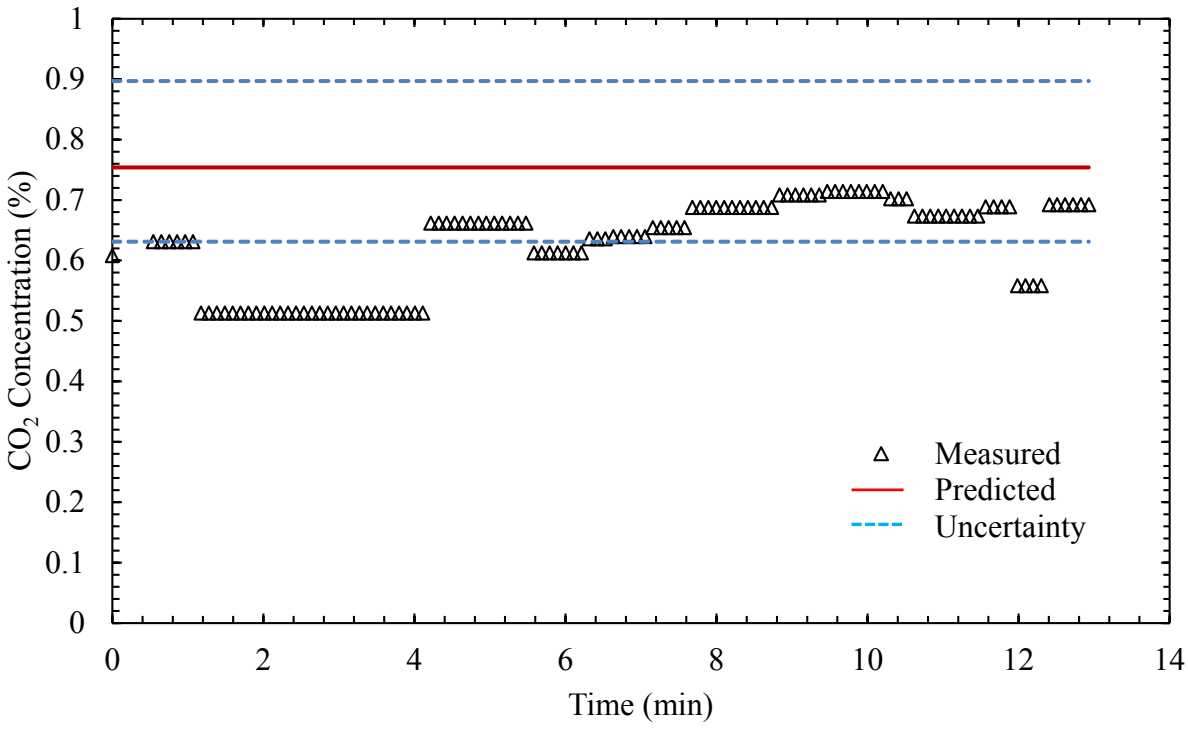

Figure 7-8 ***Experimental results of CO_2 concentration (%) in LNG operating at 425 kPa and 147 K with inlet composition of 5.9 % CO_2, 5.9 % C_2H_6, and balance CH_4***

7.3 Summary

A novel method for natural gas treatment in liquefied natural gas systems removes CO_2 to 50 ppm, removes NGLs, and cools the NG to or below liquefaction temperatures in a single process and without amine-based pretreatment. This greatly simplifies LNG processing, reduces the amount and size of equipment needed, and should greatly reduce capital and energy demands at commercial scale. Desublimating heat exchangers first developed and demonstrated for cryogenic carbon capture™ (CCC) represent some of the most novel components of this process, which is therefore referred to as CCC LNG.

Literature data provide validations of fundamental thermodynamic models used to describe this process, with a focus on the PR, SRK, and PSRK EOS. The scatter in the literature data is large compared to the difference between the literature data and the EOS predictions. At low pressures, non-idealities are less significant and Raoult's law provides reasonable predictions. At high pressure and cold temperatures, the PR EOS provides the most accurate predictions, while the PSRK EOS provides reasonable estimates and does not require empirical component interaction parameters.

A laboratory-scale version of this new process demonstrates CO_2 removal to 50 ppm and lower using artificial natural gas. At high pressures, where natural gas liquefies in the process, CO_2 solubility in the liquid phase limits the amount of CO_2 removal. In all cases, the process provides a simpler and likely more efficient and economical method of NG preparation for liquefaction than current systems.

8 CONCLUSIONS

This research theoretically and experimentally demonstrates the potential for cryogenic carbon capture and closely related processes to provide energy storage, natural gas processing, and liquefied natural gas production as up to bench scale. Detailed analyses and highly instrumented bench-scale equipment demonstrate that these processes can meet any reasonable standard for product purity in steady-state, efficient operations. Process analyses required improving several thermodynamic models and reported quantities.

A new correlation for solid-CO_2 vapor pressure improves CO_2 freezing predictions compared to established estimates by 0.3 K, 0.2 K, and 2.3 K^2 in average absolute deviation, bias, and mean square error (MSE), respectively, over using other respected vapor pressure correlations. The performance of desublimating staged-column heat exchangers in CCC ES, CCC NG, and CCC LNG is adequately predicted by Raoult's law when operating at low pressures. At higher pressures, the prediction method using Raoult's law has very reasonable estimates generally within ±5 K and is significantly easier to solve. Both the PR and SRK EOS methods are more accurate than Raoult's law as demonstrated within experimental error. Using published and accepted parameters, the PR EOS is more accurate than the SRK EOS. For systems with unknown interaction parameters between components, the PSRK EOS provides a reasonable estimate of desublimating heat exchanger performance.

Cryogenic carbon capture can be modified to yield a superior integrated energy storage and carbon capture for a coal fired power plant. CCC ES has the ideal attributes of (1) stores and releases energy with high efficiency and reasonable cost, (2) installation size on order of 100 MW, (3) no geographical constraints, (4) absorbs demand/production intermittency, and (5) bolt-on energy storage for new or existing power plants.

Steady state CCC ES has been simulated for retrofit of a 550 MW_e coal-fired power plant with the lowest steady state energy penalty. Equilibrium predictions of solid CO_2 formation have been experimentally validated on both lab- and skid-scales. Basic operation has been demonstrated with 90 % CO_2 capture on flue gas streams as high as 1.4 m^3/min. The CO_2 stream produced by the CCC ES process has a relatively high purity of 99.2 % CO_2. The emissions of volatile hydrocarbons from CCC ES meets current EPA source emission guidelines and total contact liquid losses should not be economically constraining.

The energy penalty for 90 % CO_2 capture is estimated at 0.74 MJ_e/kg CO_2 captured. Reasonable best and worst case scenarios are between 0.71-0.92 MJ_e/kg CO_2 captured. The energy penalty is estimated at 1.67 MJ_e/kg CO_2 captured in the case of CCC ECL implementation for a natural gas combined cycle power plant (4 % CO_2 inlet concentration). The cost of the CCC ES process is estimated at $361 MM Capex. The financial result is an increased cost of electricity in the range of 2.85-3.56 cents/kWh. The energy and cost numbers compare very favorably with amine-based alternative systems (1.379 MJ_e/kg CO_2 captured and cost increase of 4.76 cents/kWh), and the energy efficiency is within compressor and heat exchanger efficiencies and line losses of being the minimum energy for separation. Additionally, it is anticipated that the entire energy storage system can operate on a timescale of minutes and directly offset the problems associated with intermittent renewable energy sources such as wind and solar.

CCC ES skid-scale experiments have demonstrated feasibility of the critical CO_2 desublimation in a novel direct contact heat exchanger. Additionally, experiments performed for CCC LNG have demonstrated that a stored refrigerant can be used to drive the CCC process.

CCC NG removes CO_2 from natural gas using processes and equipment similar to those for flue gas treatments and cryogenic natural gas liquids recovery. This process does not require pressurization or distillation of the gas stream, saving capital and operating costs and energy. It also does not involve stripping and absorption towers, though it does involve a desublimating heat exchanger. Finally, it combines several separation processes into one, simplifying the overall treatment system. Data from experimental demonstrations of CCC NG up to 4 MPa indicate that the process behaves as predicted by a theoretical model based on process temperature, pressure, and gas composition and should provide a cost-effective and energy-efficient alternative to traditional gas treatments.

First-ever experimental measurements of CCC LNG performance indicate natural gas can be liquefied with high CO_2 concentrations and without pretreatment to remove CO_2. The CO_2 desublimates in a desublimating heat exchanger as it contacts cooled natural gas liquids. Pure CO_2 particles entrain in the natural gas liquids and can be removed with simple solid/liquid separators. Further, a low-pressure operation has been experimentally demonstrated to produce natural gas for liquefaction with 50 ppm CO_2 which is removed as the natural gas cools during the liquefaction process.

9 LITERATURE CITED

1. International Energy Agency *2014 Key World Energy Statistics*; 2014.

2. Environmental Protection Agency, Carbon Pollution Emission Guidelines for Existing Stationary Sources: Electric Utility Generating Units. In 2014; pp 34829 -34958.

3. Kislear, J., EPA Regulatory Primer: GHG Regulations. In US Department of Energy: 2014.

4. Renewable Energy Policy Network for the 21st Century *Renewables Global Status Report*; Ren21: Paris, 2007.

5. Global Wind Energy Council *Global Wind Report: Annual Market Update 2011*; 2012.

6. International Energy Agency *Solar Energy Perspectives*; Paris, 2011.

7. Sustainable Energy Solutions, Cryogenic Carbon Capture: Fossil-Fuel Energy for a Changing Market. In 2013.

8. Jensen, M. J.; Bergeson, D.; Frankman, D.; Baxter, L. L. In *Integrated Rapid Response Energy Storage with CO_2 Removal*, Power-Gen International, Orlando, 2012; Orlando, 2012.

9. Coal Industry Advisory Board *Power Generation from Coal: Measuring and Reporting Efficiency Performance and CO_2 Emissions*; International Energy Agency: Paris, 2010.

10. US Department of Energy, N. E. T. L. *Cost and Performance Baseline for Fossil Energy Plants Volume 1: Bituminous Coal and Natural Gas to Electricity* 2007.

11. Davison, J.; Thambimuthu, K., An overview of technologies and costs of carbon dioxide capture in power generation. *Proceedings of the Institution of Mechanical Engineers, Part A: Journal of Power and Energy* **2009,** 223, (3), 201-212.

12. Berstad, D.; Anantharaman, R.; Nekså, P., Low-temperature CO_2 capture technologies – Applications and potential. *International Journal of Refrigeration* **2013,** 36, (5), 1403-1416.

13. Rufford, T. E.; Smart, S.; Watson, G. C. Y.; Graham, B. F.; Boxall, J.; da Costa, J. C. D.; May, E. F., The removal of CO_2 and N_2 from natural gas: A review of conventional and emerging process technologies. *Journal of Petroleum Science and Engineering* **2012,** 94-95, 123-154.

14. Wilcox, J.; Haghpanah, R.; Rupp, E. C.; He, J.; Lee, K., Advancing Adsorption and Membrane Separation Processes for the Gigaton Carbon Capture Challenge. *Annual Review of Chemical and Biomolecular Engineering* **2014,** 5, (1), 479-505.

15. Gopan, A.; Kumfer, B. M.; Phillips, J.; Thimsen, D.; Smith, R.; Axelbaum, R. L., Process design and performance analysis of a Staged, Pressurized Oxy-Combustion (SPOC) power plant for carbon capture. *Applied Energy* **2014,** 125, (0), 179-188.

16. Matuszewski, M. N.; Woods, M. B. A. H.; Brasington, R. D. *Advancing Oxycombustion Technology for Bituminous Coal Power Plants: An R&D Guide*; NETL: 2012.

17. Zaman, M. H. L., Jay, Carbon capture from stationary power generation sources: A review of the current status of the technologies. *Korean Journal of Chemical Engineering* **2013,** 30, (8), 1497-1526.

18. Skorek-Osikowska, A.; Janusz-Szymańska, K.; Kotowicz, J., Modeling and analysis of selected carbon dioxide capture methods in IGCC systems. *Energy* **2012,** 45, (1), 92-100.

19. Sanchez Fernandez, E.; Goetheer, E. L. V.; Manzolini, G.; Macchi, E.; Rezvani, S.; Vlugt, T. J. H., Thermodynamic assessment of amine based CO_2 capture technologies in power plants based on European Benchmarking Task Force methodology. *Fuel* **2014,** 129, (0), 318-329.

20. Porcheron, F.; Gibert, A.; Jacquin, M.; Mougin, P.; Faraj, A.; Goulon, A.; Bouillon, P.-A.; Delfort, B.; Le Pennec, D.; Raynal, L., High throughput screening of amine thermodynamic properties applied to post-combustion CO_2 capture process evaluation. *Energy Procedia* **2011,** 4, 15-22.

21. Morton, F.; Laird, R.; Northington, J., The National Carbon Capture Center: Cost-effective test bed for carbon capture R&D. *Energy Procedia* **2013,** 37, 525-539.

22. Le Moullec, Y.; Kanniche, M., Screening of flowsheet modifications for an efficient monoethanolamine (MEA) based post-combustion CO_2 capture. *International Journal of Greenhouse Gas Control* **2011,** 5, (4), 727-740.

23. Duan, L.; Zhao, M.; Yang, Y., Integration and optimization study on the coal-fired power plant with CO_2 capture using MEA. *Energy* **2012,** 45, (1), 107-116.

24. Cohen, S. M.; Rochelle, G. T.; Webber, M. E., Optimizing post-combustion CO_2 capture in response to volatile electricity prices. *International Journal of Greenhouse Gas Control* **2012,** 8, (0), 180-195.

25. Amrollahi, Z.; Ystad, P. A. M.; Ertesvåg, I. S.; Bolland, O., Optimized process configurations of post-combustion CO_2 capture for natural-gas-fired power plant – Power plant efficiency analysis. *International Journal of Greenhouse Gas Control* **2012,** 8, 1-11.

26. Boot-Handford, M. E.; Abanades, J. C.; Anthony, E. J.; Blunt, M. J.; Brandani, S.; Mac Dowell, N.; Fernandez, J. R.; Ferrari, M.-C.; Gross, R.; Hallett, J. P.; Haszeldine, R. S.; Heptonstall, P.; Lyngfelt, A.; Makuch, Z.; Mangano, E.; Porter, R. T. J.; Pourkashanian, M.; Rochelle, G. T.; Shah, N.; Yao, J. G.; Fennell, P. S., Carbon capture and storage update. *Energy & Environmental Science* **2014,** 7, (1), 130-189.

27. Ishibashi, M.; Ota, H.; Akutsu, N.; Umeda, S.; Tajika, M.; Izumi, J.; Yasutke, A.; Kabata, T.; Kageyama, Y., Technology for removing carbon dioxide from power plant flue gas by the physical adsorption method.

28. Scholes, C. A.; Ho, M. T.; Aguiar, A. A.; Wiley, D. E.; Stevens, G. W.; Kentish, S. E., Membrane gas separation processes for CO_2 capture from cement kiln flue gas. *International Journal of Greenhouse Gas Control* **2014,** 24, 78-86.

29. Gazzani, M.; Turi, D. M.; Ghoniem, A. F.; Macchi, E.; Manzolini, G., Techno-economic assessment of two novel feeding systems for a dry-feed gasifier in an IGCC plant with Pd-membranes for CO_2 capture. *International Journal of Greenhouse Gas Control* **2014,** 25, 62-78.

30. Pan, X.; Clodic, D.; Toubassy, J., CO_2 capture by antisublimation process and its technical economic analysis. *Greenhouse Gases: Science and Technology* **2013,** 3, (1), 8-20.

31. Schach, M. O.; Oyarzun, B.; Schramm, H.; Schneider, R.; Repke, J. U., Feasibility Study of CO_2 Capture by Anti-Sublimation. *Energy Procedia* **2011,** 4, 1403-1410.

32. Herzog H, D. E., Tester J, Rosenthal R. , A research needs assessment for the capture, utilization and disposal of carbon dioxide from fossil fuel-fired power plans. *Final report DOE contract no. DE-FG02-92ER30194, Cambridge, MA, Massachusetts Institute of Technology, Energy Laboratory; 1993.* **1993**.

33. Berguerand, N.; Lyngfelt, A., Design and operation of a 10kWth chemical-looping combustor for solid fuels – Testing with South African coal. *Fuel* **2008,** 87, (12), 2713-2726.

34. Cho, P.; Mattisson, T.; Lyngfelt, A., Comparison of iron-, nickel-, copper- and manganese-based oxygen carriers for chemical-looping combustion. *Fuel* **2004,** 83, (9), 1215-1225.

35. Fan, L.-S.; Zeng, L.; Wang, W.; Luo, S., Chemical looping processes for CO_2 capture and carbonaceous fuel conversion - prospect and opportunity. *Energy & Environmental Science* **2012,** 5, (6), 7254-7280.

36. Fan, L.-S., Coal Direct Chemical Looping (CDCL) Retrofit to Pulverized Coal Power Plants for In-Situ CO2 Capture. In *NETL CO2 Capture Technology Meeting*, Pittsburgh, PA, 2012.

37. Tong, A.; Bayham, S.; Kathe, M. V.; Zeng, L.; Luo, S.; Fan, L.-S., Iron-based syngas chemical looping process and coal-direct chemical looping process development at Ohio State University. *Applied Energy* **2014,** 113, (0), 1836-1845.

38. National Energy Technology Laboratory *Advanced Carbon Dioxide Capture R&D Program: Technology Update*; 2013; pp B-516 - B-539.

39. National Energy Technology Laboratory, Cost Performance Baseline for Fossil Energy Plants, Revision 2a. In Department of Energy, Ed. 2013; Vol. 1.

40. Kothandaraman, A. *Carbon Dioxide Capture by Chemical Absorption: A Solvent Comparison Study*; Massachusetts Institute of Technology: Cambridge, 2010.

41. Chabanon, E.; Roizard, D.; Favre, E., Modeling strategies of membrane contactors for post-combustion carbon capture: A critical comparative study. *Chemical Engineering Science* **2013,** 87, 393-407.

42. Sjardin, M.; Damen, K.; Faaij, A., Techno-economic prospects of small-scale membrane reactors in a future hydrogen-fuelled transportation sector. *Energy* **2006,** 31, (14), 2523-2555.

43. Shao, P.; Dal-Cin, M. M.; Guiver, M. D.; Kumar, A., Simulation of membrane-based CO_2 capture in a coal-fired power plant. *Journal of Membrane Science* **2013,** 427, 451-459.

44. Clodic, D.; El Hitti, R.; Younes, M.; Bill, A.; Casier, F. In *CO_2 capture by anti-sublimation Thermo-economic process evaluation*, 4th Annual Conference on Carbon Capture & Sequestration, Alexandria, Virginia, May 2-5, 2005; Alexandria, Virginia, 2005.

45. Tuinier, M. J.; van Sint Annaland, M.; Kramer, G. J.; Kuipers, J. A. M., Cryogenic capture using dynamically operated packed beds. *Chemical Engineering Science* **2010,** 65, (1), 114-119.

46. Castrogiovanni, A.; Balepin, V.; Robertson, A.; Calayag, B. In *A High Efficiency Inertial CO2 Extraction System*, NETL CO2 Capture Technology Meeting, Pittsburgh, PA, 2012; Pittsburgh, PA, 2012.

47. Larsen, R.; Fox, C.; Meldrum, B.; Baxter, L. L. In *Cryogenic Pollutant Balances Extended*, American Institute of Chemical Engineers, 2010; 2010.

48. Larsen, R.; Fox, C.; Meldrum, B.; Hartvitssen, J.; Baxter, L. L. In *Cryogenic Pollutant Removal*, Int. Tech. Conf. Clean Coal Fuel Syst., 2010; American Chemical Society (ACS): 2010.

49. Tuinier, M. J.; Van Sint Annaland, M.; Kuipers, J. A. M., A Novel Process for Cryogenic CO_2 Capture using Dynamically Operated Packed Beds - An Experimental and Numerical Study. *International Journal of Greenhouse Gas Control* **2011,** 5, (4), 694-701.

50. James, D. W. *Falling Drop CO_2 Deposition (Desublimation) Heat Exchanger for the Cryogenic Carbon Capture*; BYU: Provo, 2011.

51. Burt, S.; Baxter, A.; Baxter, L. L. In *Cryogenic CO_2 Capture to Control Climate Change Emissions*, Clearwater, 2009; Clearwater Clean Coal Conference: Clearwater, 2009.

52. United Nations *World Population Prospects: The 2010 Revision*; New York, 2011.

53. PovcalNet: the on-line tool for poverty measurement developed by Development Research Group of the World Bank. http://iresearch.worldbank.org/PovcalNet/index.htm (July 2),

54. Department of Energy/US Energy Information Administration *Interational Energy Outlook 2011*; 2011.

55. International Energy Agency *World Energy Outlook 2012*; Paris, France, 2012.

56. BBC Hundreds of millions without power in India. http://www.bbc.co.uk/news/world-asia-india-19060279 (March 7),

57. LaCommare, K. H.; Eto, J. H. *Understanding the Cost of Power Interruptions to U.S. Electricity Consumers*; Lawerence Berkeley National Laboratory: Berkeley, CA, 2004.

58. GE Energy *Western Wind and Solar Integration Study*; National Renewable Energy Laboratory: 2010.

59. U.S. Energy Information Administration *Annual Energy Outlook 2014*; 2014.

60. U.S. Energy Information Administration *Annual Energy Outlook 2013*; 2013.

61. Pickard, W. F., The history, present state, and future prospects of underground pumped hydro for massive energy storage. *Proceedings of the IEEE* **2012,** 100, (2), 473-483.

62. U.S. Energy Information Administration *Levelized Cost of New Generation Resources in the Annual Energy Outlook 2012*; July 2012.

63. Dunn, B.; Kamath, H.; Tarascon, J.-M., Electrical Energy Storage for the Grid: A Battery of Choices. *Science* 2011, pp 928-935.

64. Divya, K. C.; Østergaard, J., Battery energy storage technology for power systems—An overview. *Electric Power Systems Research* **2009,** 79, (4), 511-520.

65. Sandia National Laboratories, DOE Energy Storage Database. In 2013.

66. Elmegaard, B.; Brix, W. In *Efficiency of Compressed Air Energy Storage*, ECOS, Novi Sad, Serbia, 2011; Novi Sad, Serbia, 2011; pp 2512-2523.

67. National Renewable Energy Laboratory Gemasolar Thermosolar Plant. http://www.nrel.gov/csp/solarpaces/project_detail.cfm/projectID=40 (10 Apr),

68. Crotogino, F.; Mohmeyer, K. U.; Scharf, R., Huntorf CAES: More than 20 years of successful operation. In *Solution Mining Research Institute Meeting*, Orlando, Florida, USA, 2001.

69. Chen, H.; Cong, T. N.; Yang, W.; Tan, C.; Li, Y.; Ding, Y., Progress in electrical energy storage system: A critical review. *Progress in Natural Science* **2009,** 19, (3), 291-312.

70. Lazarewicz, M. In *Status of Flywheel Storage Operation of First Frequency Regulation Plants*, EESAT, San Diego, CA, October 17-19 2011, 2011; San Diego, CA, 2011.

71. International Water Power & Dam Construction, The World's Pumped Storage Plants. *International Water Power & Dam Construction* 2009, p S280.

72. Fox, T. In *Storing Electricity Using Cryogenic Technology in a UK Policy Context*, Energy Storage Symposium, Lenfest Center for Sustainable Energy, Columbia University, 2012; Lenfest Center for Sustainable Energy, Columbia University, 2012.

73. Rochelle, G. T., Amine Scrubbing for CO_2 Capture. *Science* **2009,** 325, (5948), 1652-1654.

74. Grunvald, A.; Izotov, N.; Nemov, V., Gas Quality Requirements as a Factor of Successful LNG Projects Implementation. In *International Gas Union Research Conference*, Paris, 2008.

75. Gas Processors Suppliers Association; Gas Processors Association *GPSA Engineering Data Book*; Tulsa, 2004; pp 2-3,.

76. Nichols, J. L. V.; Friedman, B. M.; Nold, A. L.; McCutcheon, S.; Goethe, A. In *Processing Technologies for CO_2 Rich Gas*, 88th Annual Convention of the Gas Processors Association (GPA), San Antonio, Texas, 2009; San Antonio, Texas, 2009.

77. DIPPR Project 801. In Provo, UT, 2012.

78. Gillespie, P. C. Removal of Carbon Dioxide from Natural Gas by Cryogenic Distillation. Brigham Young University, Provo, Utah, 1980.

79. Berstad, D.; Nekså, P.; Anantharaman, R., Low-temperature CO_2 Removal from Natural Gas. *Energy Procedia* **2012,** 26, (0), 41-48.

80. Willems, G. P.; Golombok, M.; Tesselaar, G.; Brouwers, J. J. H., Condensed rotational separation of CO_2 from natural gas. *AIChE Journal* **2010,** 56, (1), 150-159.

81. van Wissen, R. J. E. Centrifugal Separation for Cleaning Well Gas Streams: from Concept to Prototype. Eindhoven University of Technology, 2006.

82. Holmes, A. S.; Ryan, J. M. Solidification prevention. 1982.

83. Holmes, A. S.; Ryan, J. M. Distillative separations of gas mixtures containing methane, carbon dioxide and other components. 1984.

84. Amin, R.; Jackson, A.; Kennaird, T., The Cryocell: An Advanced Gas Sweetening Technology. In *International Petroleum Technology Conference*, Doha, Qatar, 2005.

85. Amin, R. Method of removing solid carbon dioxide. 2009.

86. Amin, R.; Groothuis, C. K. Removing contaminants from natural gas. US7152431 B2, 2006.

87. Amin, R.; Kennaird, A. F. Process and device for production of LNG by removal of freezable solids. US7325415 B2, 2008.

88. Hart, A.; Gnanendran, N., Cryogenic CO_2 capture in natural gas. *Energy Procedia* **2009,** 1, (1), 697-706.

89. Surovtseva, D.; Amin, R.; Barifcani, A., Design and Operation of Pilot Plant for CO_2 Capture from IGCC Flue Gases by Combined Cryogenic and Hydrate Method. *Chemical Engineering Research and Design* **2011,** 89, (9), 1752-1757.

90. Victory, D. J.; Valencia, J. A., Methane CO_2 Fractionation. *Hydrocarbon Processing* **1987,** 66, (5), 44-46.

91. Thomas, E. R.; Denton, R. D., Conceptual studies for CO_2/natural gas separation using the controlled freeze zone (CFZ) process. *Gas Separation & Purification* **1988,** 2, (2), 84-89.

92. Valencia, J. A.; Northrop, P. S.; Mart, C. J. In *Controlled Freeze Zone Technology for Enabling Processing of High CO_2 and H_2S Gas Reserves*, International Petroleum Technology Conference, Kuala Lumpur, Malaysia, 2008; Society of Petroleum Engineers: Kuala Lumpur, Malaysia, 2008; pp 2358-2363.

93. Oelfke, R. H.; Denton, R. D.; Valencia, J. A., Controlled Freeze Zone™ Commercial Demonstration Plant Advances Technology for the Commercialization of North American Sour Gas Resources. In *Sour Gas and Related Technologies*, John Wiley & Sons, Inc.: 2012; pp 79-90.

94. Valencia, J. A.; Kelman, S. D.; Nagavarapu, A.; Maher, D. W., The Controlled Freeze Zone Technology for the Commercialization of Sour Gas Resources. In International Petroleum Technology Conference: 2014.

95. Grunvald, A.; Izotov, N.; Nemov, V. In *Gas Quality Requirements as a Factor of Successful LNG Projects Implementation*, International Gas Union Research Conference, Paris, 2008; Paris, 2008.

96. Gas Proccesors Suppliers Association, *GPSA Engineering Data Book*. Eleventh Edition ed.; Tulsa, OK, 1998.

97. Shen, T.; Gao, T.; Lin, W.; Gu, A., Determination of CO_2 Solubility in Saturated Liquid CH_4 + N_2 and CH_4 + C_2H_6 Mixtures above Atmospheric Pressure. *Journal of Chemical & Engineering Data* **2012,** 57, (8), 2296-2303.

98. Baxter, L. L. Carbon Dioxide Capture from Flue Gas. US2011/0226010, 2008.

99. Span, R.; Wagner, W., A New Equation of State for Carbon Dioxide Covering the Fluid Region from the Triple-Point Temperature to 1100 K at Pressures up to 800 MPa. *Journal of Physical and Chemical Reference Data* **1996,** 25, (6), 1509-1596.

100. DIPPR, Project 801. In Provo, UT, 2012.

101. NIST, Standard Reference Database. In 2012.

102. Shen, T.; Lin, W., Calculation of Carbon Dioxide Solubility in Liquefied Natural Gas. *International Journal of Chemical Engineering and Applications* **2011,** 2, (5).

103. Bryson, C. E.; Cazcarra, V.; Levenson, L. L. J., Sublimation rates and vapor pressure of H_2O, CO_2, N_2O, and Xe oxide, and Xenon. *Chemical Engineering Data* **1974,** 19, (107).

104. Tickner, A. W.; Lossing, F. P., The Measurement of Low Vapor Pressures by Means of a Mass Spectrometer. *Journal of Physical and Colloid Chemistry* **1951**, (55), 733-40.

105. Stull, D. R., Vapor Pressure of Pure Substances. *Industrial & Engineering Chemistry* **1947**, (39), 517-540.

106. Kaye, G. W. C.; Laby, T. H., *Tables of Physical and Chemical Constants, 14th ed.* Longman Group Limited: London, 1973.

107. Thermodynamics Research Center, Selected Values of Properties of Chemical Compounds. In Texas A&M University, College Station, TX.

108. Giauque, W. F.; Egan, C. J., Carbon Dioxide. The Heat Capacity and Vapor Pressure of the Solid. *Journal of Chemical Physics* **1937,** 5, (45).

109. Bilkadi, Z.; Lee, M. W.; Bigeleisen, J., Phase equilibrium isotope effects in molecular solids and liquids. Vapor pressures of the isotopic carbon dioxide molecules. *The Journal of Chemical Physics* **1975,** 62, (6), 2087-2093.

110. Ambrose, D., The vapour pressures and critical temperatures of acetylene and carbon dioxide. *Transactions of the Faraday Society* **1956,** 52, (0), 772-781.

111. Heuse, W.; Otto, J., Eine neue gasthermometrische Bestimmung von Fixpunkten unterhalb 00 in Verbindung mit Tensions- und Widerstandsthermometern. *Annalen der Physik* **1931,** 401, (4), 486-504.

112. Fernandez-Fassnacht, E.; Del Rio, F., The Vapor Pressure of CO_2 from 194 to 243K. *Journal of Chemical Thermodynamics* **1984,** 16, (469).

113. Meyers, C. H.; Van Dusen, M. S., The Vapor Pressure of Liquid and Solid Carbon Dioxide. *Journal of Research of the National Bureau of Standards* **1933,** 10, 381-412.

114. Mullins, J. C.; Kirk, B. S.; Ziegler, W. T. *Calculation of the Vapor Pressure and Heats of Vaporization and Sublimation of Liquids and Solids, Especially below One Atmosphere. V. Carbon Monoxide and Carbon Dioxide*; Ga. Inst. Technol.: 1963.

115. Marsh, K. N., *Recommended Reference Materials for the Realization of Physicochemical Properties*. Blackwell Sci. Pub.: Oxford, 1987.

116. Baughman, G. L.; Westhoff, S. P.; Dincer, S.; Duston, D. D.; Kidnay, A. J., The solid + vapor phase equilibrium and the interaction second virial coefficients for argon +, nitrogen +, methane +, and helium + neopentane. *Journal of Chemical Thermodynamics* **1974,** 6, (1121).

117. Lavik, V. F. Freeze out in natural gas systems. Norwegian University of Science and Technology, Trondhiem, Norway, 2009.

118. Martynov, S.; Brown, S.; Mahgerefteh, H., An extended Peng-Robinson equation of state for carbon dioxide solid-vapor equilibrium. *Greenhouse Gases: Science and Technology* **2013,** 3, (2), 136-147.

119. Yokozeki, A., Analytical Equation of State for Solid-Liquid-Vapor Phases. *International Journal of Thermophysics* **2003,** 24, (3), 589-620.

120. Vinš, V.; Jäger, A.; Hrubý, J.; Span, R. In *Phase equilibria of carbon dioxide and methane gas-hydrates predicted with the modified analytical S-L-V equation of state*, 2012; 2012.

121. Stringari, P.; Campestrini, M.; Coquelet, C.; Arpentinier, P., An equation of state for solid–liquid–vapor equilibrium applied to gas processing and natural gas liquefaction. *Fluid Phase Equilibria* **2014,** 362, (0), 258-267.

122. Donnelly, H. G.; Katz, D. L., Phase Equilibria in the Carbon Dioxide–Methane System. *Industrial & Engineering Chemistry* **1954,** 46, (3), 511-517.

123. De Guido, G.; Langè, S.; Moioli, S.; Pellegrini, L. A., Thermodynamic method for the prediction of solid CO_2 formation from multicomponent mixtures. *Process Safety and Environmental Protection* **2014,** 92, (1), 70-79.

124. Sandler, S. I., *Chemical, Biochemical, and Engineering Thermodynamics*. 4th ed.; John Wiley & Sons, Inc.: 2006.

125. Le, T. Measurement of carbon dioxide freezing in mixtures of methane, ethane and nitrogen. M.Sc., University of Calgary (Canada), Ann Arbor, 2006.

126. ZareNezhad, B., Prediction of CO_2 freezing points for the mixtures of CO_2-CH_4 at cryogenic conditions of NGL extraction plants. *Korean Journal of Chemical Engineering* **2006,** 23, (5), 827-831.

127. Holderbaum, T.; Gmehling, J., PSRK: A Group Contribution Equation of State Based on UNIFAC. *Fluid Phase Equilibria* **1991,** 70, (2–3), 251-265.

128. Horstmann, S.; Jabłoniec, A.; Krafczyk, J.; Fischer, K.; Gmehling, J., PSRK group contribution equation of state: comprehensive revision and extension IV, including critical constants and α-function parameters for 1000 components. *Fluid Phase Equilibria* **2005,** 227, (2), 157-164.

129. Agrawal, G. M.; Laverman, R. J., Phase Behavior of the Methane Carbon Dioxide System in the Solid-Vapor Region. *Advances in Cryogenic Engineering* **1974,** 19, 327-338.

130. Pikaar, M. J. Study of phase equilibria in hydrocarbon-CO_2 systems. Imperial College of Science and Technology, London, 1959.

131. Zhang, L.; Burgass, R.; Chapoy, A.; Tohidi, B.; Solbraa, E., Measurement and Modeling of CO_2 Frost Points in the CO_2–Methane Systems. *Journal of Chemical & Engineering Data* **2011,** 56, (6), 2971-2975.

132. Le, T. T.; Trebble, M. A., Measurement of Carbon Dioxide Freezing in Mixtures of Methane, Ethane, and Nitrogen in the Solid−Vapor Equilibrium Region. *Journal of Chemical & Engineering Data* **2007,** 52, (3), 683-686.

133. Kurata, F., Solubility of Solid Carbon Dioxide in Pure Light Hydrocarbons and Mixtures of Light Hydrocarbons. *GPA* **1974**.

134. Davis, J. A.; Rodewald, N.; Kurata, F., Solid-liquid-vapor phase behavior of the methane-carbon dioxide system. *AIChE Journal* **1962,** 8, (4), 537-539.

135. Safdarnejad, S. M.; Hedengren, J. D.; Baxter, L. L., Grid-level dynamic optimization of cryogenic carbon capture with conventional and renewable power sources. *Applied Energy. Under Review.* **2015**.

136. Safdarnejad, S. M.; Kennington, L.; Baxter, L. L.; Hedengren, J. D. In *Investigating the impact of Cryogenic Carbon Capture on power plant performance*, American Control Conference, Chicago, IL. Accepted, 2015; Chicago, IL. Accepted, 2015.

137. Bukowski, J. In *Innovations in Natural Gas Liquefaction Technology for Future LNG Plants and Floating LNG Facilities*, International Gas Union Research Conference, 2011; 2011.

138. Ransbarger, W., A Fresh Look at LNG Process Efficiency. **2007**, (Spring).

139. Shukri, T., LNG Technologies and the Important Criteria for Selection. **2004**, (February).

140. Air Products, Air Products' AP-SMR and AP-C_3MR LNG Processes: Unlocking the potential for midsize plants. In 2013.

141. Hasan, M. M. F.; Zheng, A. M.; Karimi, I. A., Minimizing Boil-Off Losses in Liquefied Natural Gas Transportation. **2009,** 48, (9571-9580).

142. Moon, J. W.; Lee, Y. P.; Jin, Y. W.; Hong, E. S.; Chang, H. M. In *Cryogenic Refrigeration Cycle for Re-Liquefaction of LNG Boil-Off Gass*, International Cryocooler Conference, Boulder, CO, 2007; Commerical Cryocooler Applications: Boulder, CO, 2007.

143. Yang, Y.; Kim, J.; Seo, H.; Lee, K.; Yoon, I. In *Development of the World's Largest Above-Ground Full Containment LNG Storage Tank*, Amsterdam, 2006; 23rd World Gas Conference: Amsterdam, 2006.

144. Shirazi, M. M. H. S.; Mowla, D., Energy Optimization for Liquefaction Process of Natural Gas in Peak Shaving Plant. *Energy* **2010,** 35, (2878-2885).

145. Chukwudeme, E. A.; Hamouda, A. A., Enhanced Oil Recovery (EOR) by Miscible CO2 and Water Flooding of Asphaltenic and Non-Asphaltenic Oils. *Energies* **2009,** 2, (3), 714-737.

146. Chen, G.; Wang, X.; Liang, Z.; Gao, R.; Sema, T.; Luo, P.; Zeng, F.; Tontiwachwuthikul, P., Simulation of CO2-Oil Minimum Miscibility Pressure (MMP) for CO2 Enhanced Oil Recovery (EOR) using Neural Networks. *Energy Procedia* **2013,** 37, 6877-6884.

147. Su, K.; Liao, X.; Zhao, X.; Zhang, H., Coupled CO2Enhanced Oil Recovery and Sequestration in China's Demonstration Project: Case Study and Parameter Optimization. *Energy & Fuels* **2013,** 27, (1), 378-386.

148. Nielson, B. J. Cryogenic Carbon Capture using a Desublimating Spray Tower. Brigham Young University, Provo, UT, 2013.

149. Johnson, L. L.; Renaudin, G., Liquid turbines improve LNG operations. *Journal Name: Oil and Gas Journal; Journal Volume: 94; Journal Issue: 47; Other Information: PBD: 18 Nov 1996* **1996**, Medium: X; Size: pp. 31-36.

150. US Department of Energy, N. E. T. L. *Pulverized Coal Oxycombustion Power Plants Volume 1: Bituminous Coal to Electricity: Revision 2*; 2008.

151. Hoeger, C.; Bence, C.; Burt, S. S.; Baxter, A.; Baxter, L. In *Cryogenic CO_2 capture for improved efficiency at reduced cost*, 2010 AIChE Annual Meeting, 10AIChE, November 7, 2010 - November 12, 2010, Salt Lake City, UT, United states, 2010; American Institute of Chemical Engineers: Salt Lake City, UT, United states, 2010.

152. Baxter, L. L. Carbon Dioxide Capture from Flue Gas. PCT/US2008/85075, November 28,2007, 2007.

153. Baxter, L. L. Fossil and Biomass Power Systems with Stable CO_2 Sequestration. 61,005,802, 2008.

154. Baxter, L. L. Carbon Dioxide Capture from Flue Gas. PCT/US2008/85075, November 28,2007, 2011.

155. Baxter, L. L. The Cryogenic Carbon Capture Process. 2009:740158(Patent), 5/24/2011, 2011.

156. Baxter, L. L. Methods and systems for separating condensable vapors from gases. US8715401, 2014.

157. Baxter, L. L.; Bence, C. S. Systems and methods for separating condensable vapors from gases by direct-contact heat exchange. US8764885, 2014.

158. Nagavarapu, A. K.; Valencia, J. A.; Kelman, S. D. In *Application of Controlled Freeze Zone™ Technology for Commercialization of Sour Gas Resources*, AIChE Spring Meeting, New Orleans. LA, April 2, 2014, 2014; New Orleans. LA, 2014.

APPENDIX

A Process Flow Diagrams of Full-Scale CCC ES

B Stream Table of Base Case CCC ES at Full-Scale

C CCC NG & CCC LNG Apparatus Piping & Instrumentation Diagram

D Natural Gas Apparatus Wiring Diagram

E LabVIEW Program to control Natural Gas Apparatus

F Calibration Summaries for MKS

A PROCESS FLOW DIAGRAMS OF FULL-SCALE CCC ES

The process flow diagrams are broken into two sections. The first section is the CCC portion of the process and the second section is the energy storage portion of the process.

C–101 Flue Gas Blower	C–105 Separations Makeup Compressor	C–106 CF4 Compresor	C–520 NG Booster	C–521 Staged Propane Compressor	C–522 Mixed Refrigerant Compressor	C–524 Combustion Air Compressor
E–121 CF4 Recuperator	E–122 CF4 After–cooler	E–123 Condenser/Melter	E–510 NG Liquefying Heat Exchanger	E–511 Refrigerant Regenerator	E–512 NG Pre–cooler	E–513 Combustion Air Recuperator
V–101 A/B Molecular Sieve Assembly	V–102 Separations Decanter	V–103 CO2 Vaporizer	V–104 Solid/Liquid Separations Cyclone	V–106 Expansion Tank	V–501 CO2 Removal	V–502 NG Dryer

Stream Legend

- Flue Gas/CO2
- Air
- Natural Gas
- Contact Liquid
- N2 Rich
- Utility Stream
- CO2 Rich
- CF4 Refrigerant

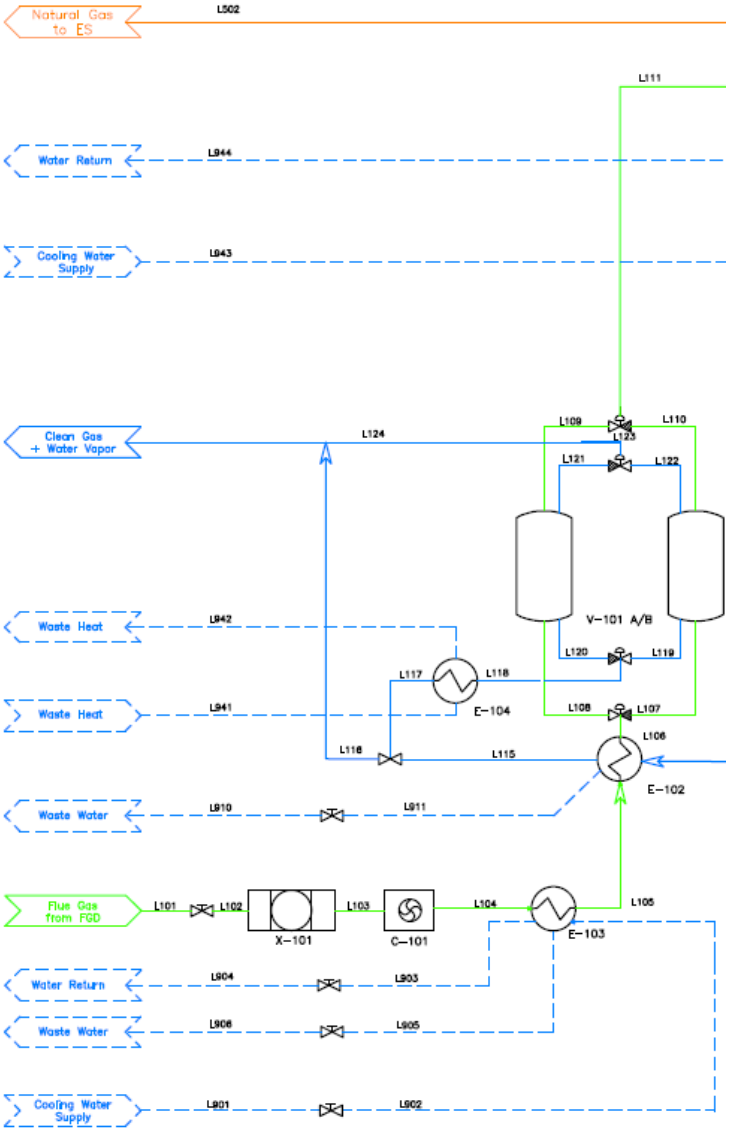

Flue Gas Condition:	Lines
16 psi	Lines
16 °C	Lines
N2: 68.90%	Lines
H2O: 15.17%	Lines
CO2: 13.53%	Lines
O2: 02.40%	Lines
SO2: <1ppm	

C-525 LNG Pump
E-102 Flue Gas Freezer
E-103 Flue Gas Aftercooler
E-104 Molecular Sieve Regenerator/Heater
E-109 Flue Gas Pre-Desublimating Cooler
E-110 Primary Desublimator
E-111 Contact Liquid Cooler
E-116 Separations Recuperator
E-120 CF4 Sub-cooler
G-500 Generator
P-102 Liquid Circulation Pump
P-103 Liquid CO2 Booster Pump
P-105 Slurry Pressurizing Pump
P-109 Pipeline Pump
T-523 NG Turbine
TK-102 Intermediate CO2 Storage
TK-103 Contact Liquid Reservoir
TK-503 Liquid NG Tank
X-101 Bag Particulate Filter

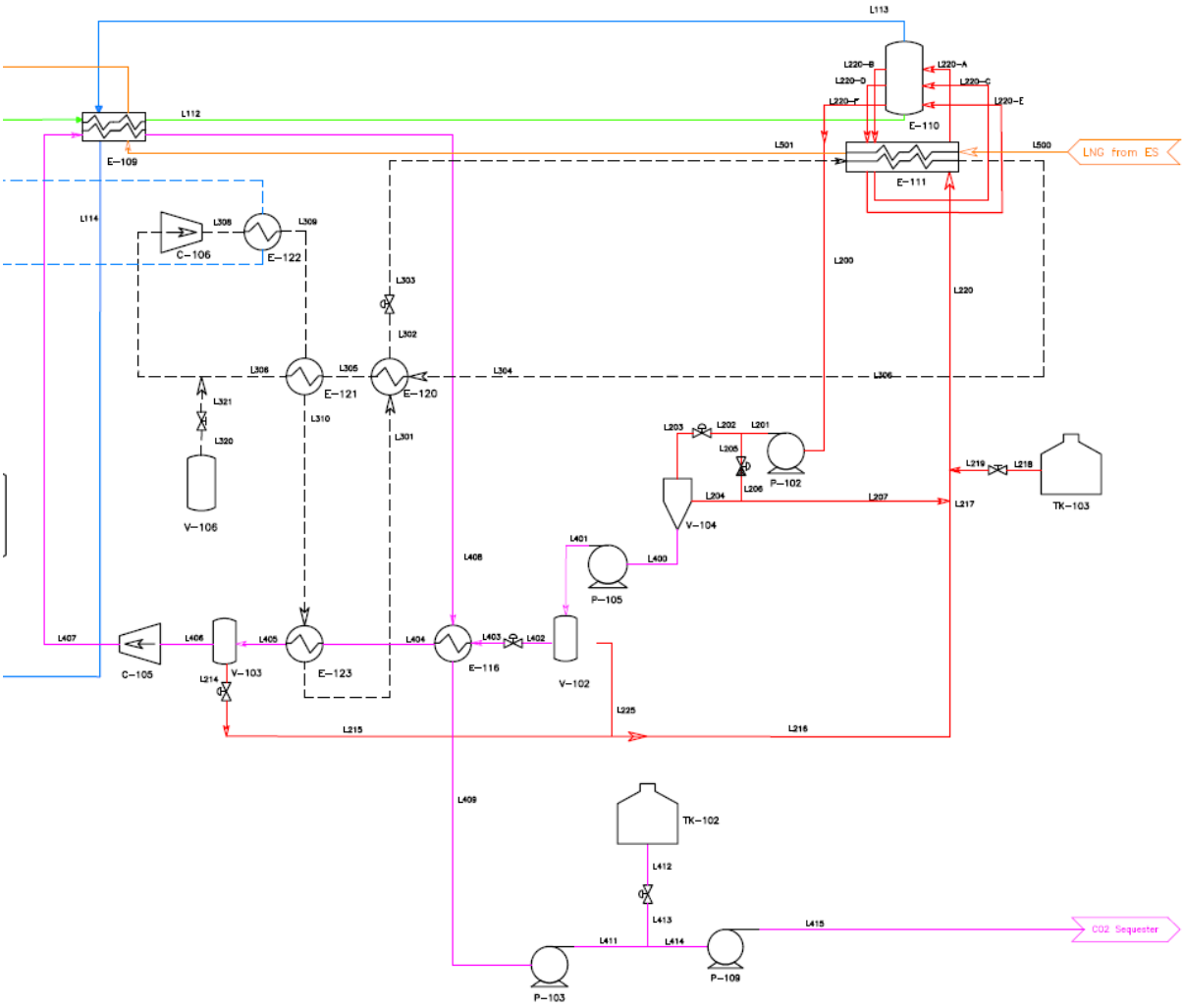

100 – 199 are nitrogen rich
200 – 299 are contact liquid rich
300 – 399 are CF4 refrigerant
400 – 499 are CO2 rich
500 – 599 are natural gas
900 – 999 are utilities

REV	DESCRIPTION	BY	DATE
1	Preliminary PFD	DB	3/1/13

CONFIDENTIAL

Date: 19-FEB-2013
Engineer: D BERGESON
Approved By: M JENSEN
Title: ES-CCC MAIN CONCEPTUAL PFD
Size: B
DWG No.: BYU_ESCCC_FULL_CCC
Rev.: 1

C–101 Flue Gas Blower	C–105 Separations Makeup Compressor	C–106 CF4 Compresor	C–520 NG Booster	C–521 Staged Propane Compressor	C–522 Mixed Refrigerant Compressor	C–524 Combustion Air Compressor	L
E–121 CF4 Recuperator	E–122 CF4 After–cooler	E–123 Condenser/Melter	E–510 NG Liquefying Heat Exchanger	E–511 Refrigerant Regenerator	E–512 NG Pre–cooler	E–513 Combustion Air Recuperator	
V–101 A/B Molecular Sieve Assembly	V–102 Separations Decanter	V–103 CO2 Vaporizer	V–104 Solid/Liquid Separations Cyclone	V–106 Expansion Tank	V–501 CO2 Removal	V–502 NG Dryer	Bag F

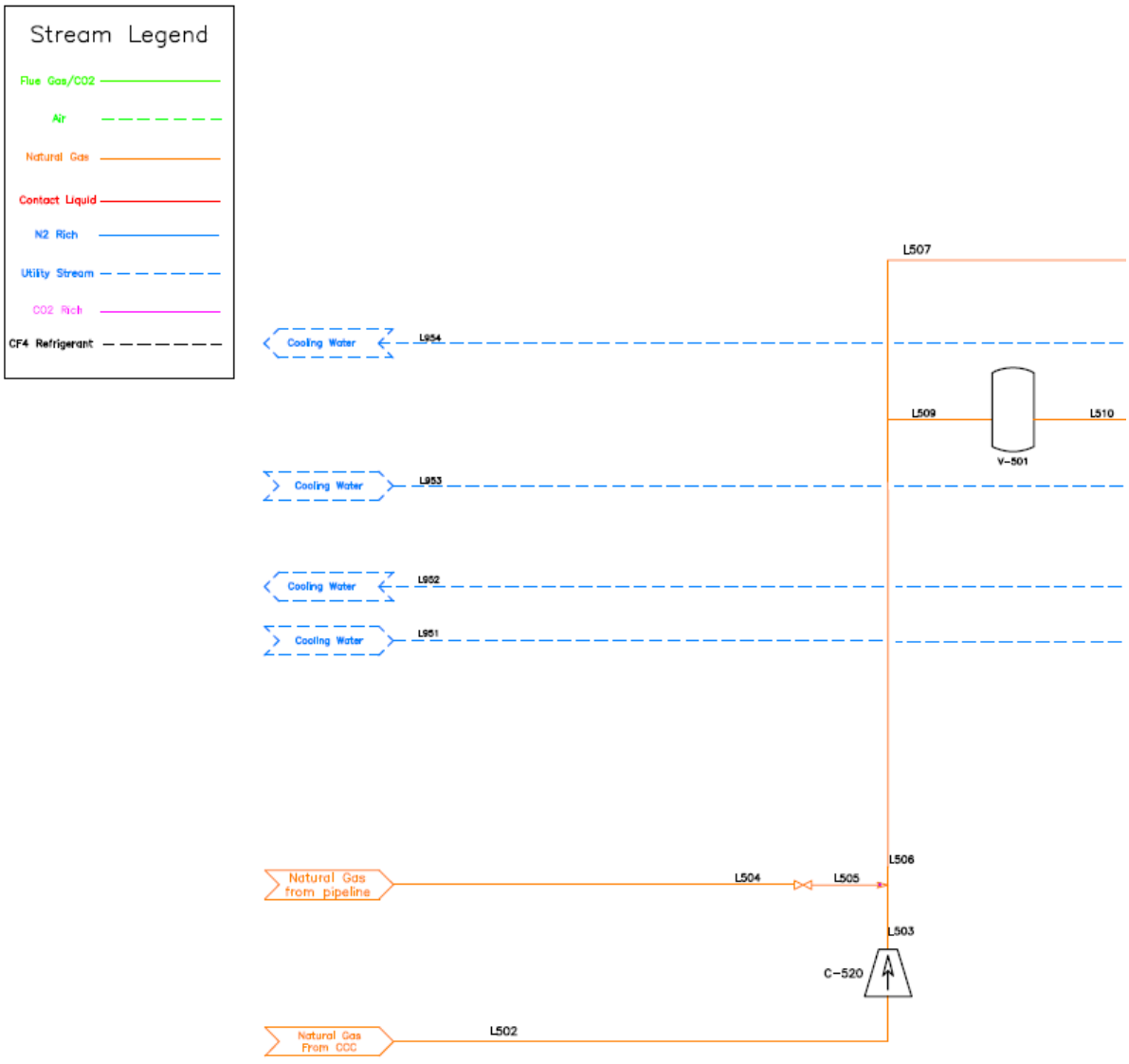

Natural Gas Composition 800 psi 25 °C			
Methane:	89.08%	N–butane:	0.288%
N2:	2.39%	Iso–pentane:	0.095%
CO2:	1.91%	N–pentane:	0.095%
Ethane:	4.80%	Hexane:	0.077%
Propane:	0.973%	Heptane:	0.006%
Iso–butane:	0.286%		

Lines 1(
Lines 2(
Lines 3(
Lines 4(
Lines 5(
Lines 9(

C–525 LNG Pump
E–102 Flue Gas Freezer
E–103 Flue Gas Aftercooler
E–104 Molecular Sieve Regenerator/Heater
E–109 Flue Gas Pre–Desublimating Cooler
E–110 Primary Desublimator
E–111 Contact Liquid Cooler
E–116 Separations Recuperator
E–120 CF4 Sub–cooler
G–500 Generator
P–102 Liquid Circulation Pump
P–103 Liquid CO2 Booster Pump
P–105 Slurry Pressurizing Pump
P–109 Pipeline Pump
T–523 NG Turbine
TK–102 Intermediate CO2 Storage
TK–103 Contact Liquid Reservoir
TK–503 Liquid NG Tank
X–101 Particulate Filter

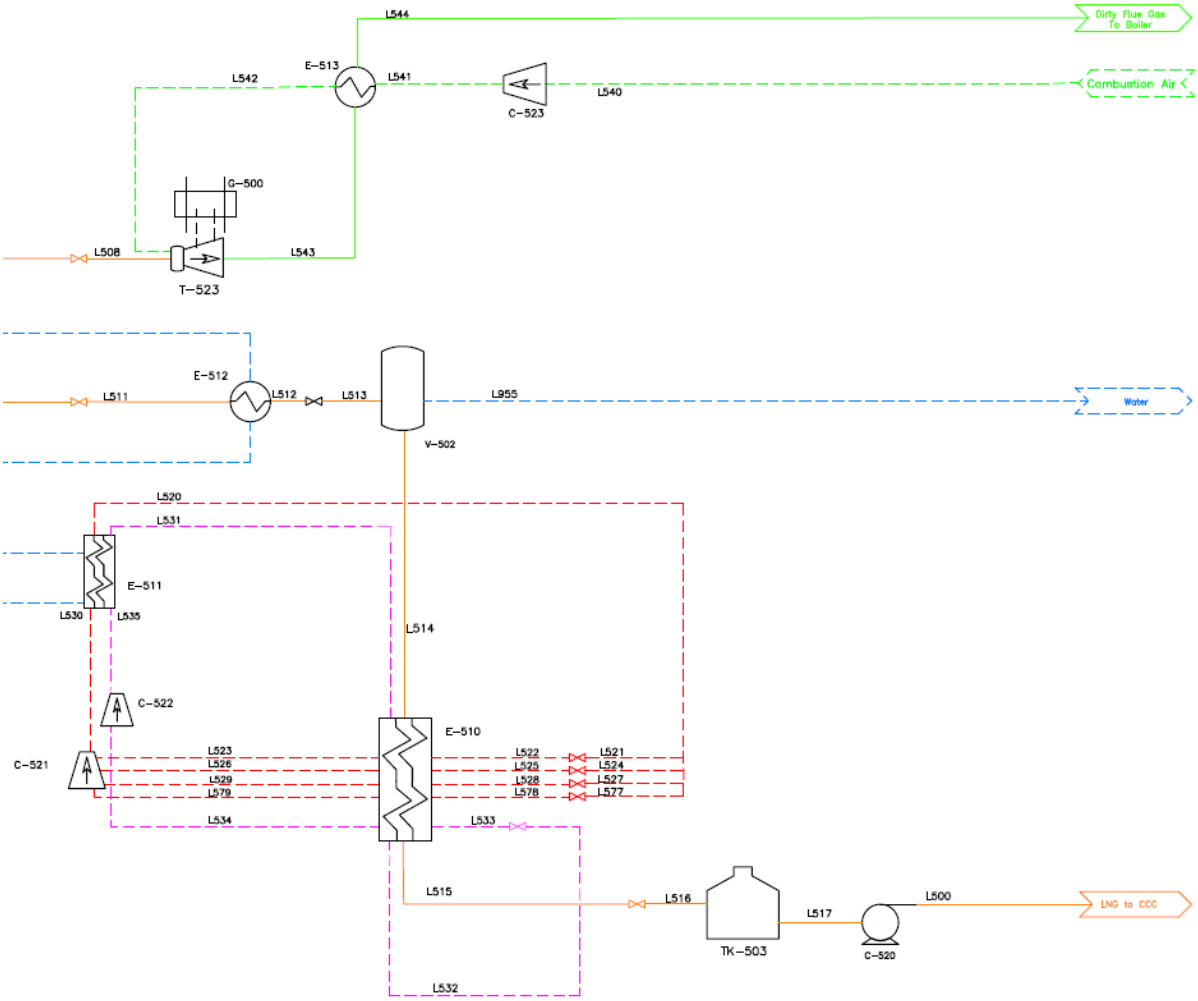

100 – 199 are nitrogen rich 200 – 299 are contact liquid rich 300 – 399 are CF4 refrigerant 400 – 499 are CO2 rich 500 – 599 are natural gas 900 – 999 are utilities	REV	DESCRIPTION	BY	DATE
	1	Preliminary PFD	DB	3/1/13

CONFIDENTIAL

Date: 23–FEB–2013
Engineer: D BERGESON
Approved By: M JENSEN

Title: ES–CCC LNG CONCEPTUAL PFD
Size: B
DWG No.: BYU_ESCCC_FULL_LNG
Rev.: 1

B STREAM TABLE OF BASE CASE CCC ES AT FULL-SCALE

Substream	L100	L101	L102	L104	L106	L111	L112	L112A
O_2 [kmol/sec]	0.5012	0.5011998	0.5011998	0.5011997	0.5011997	0.5011997	0.5011997	0.5013493
N_2 [kmol/sec]	14.21737	14.21737	14.21737	14.21746	14.21746	14.21746	14.21746	14.21797
CO_2 [kmol/sec]	2.825515	2.825515	2.825515	2.82559	2.82559	2.82559	2.82559	2.770428
CO_2(S) [kmol/sec]	0	0	0	0	0	0	0	0
CF_4 [kmol/sec]	0	0	0	0	0	0	0	0
CH_4 [kmol/sec]	0	0	0	0	0	0	0	0
C_2H_6 [kmol/sec]	0	0	0	0	0	0	0	0
C_3H_8 [kmol/sec]	0	0	0	0	0	0	0	0
C_4H_{10} [kmol/sec]	0	0	0	0	0	0	0	0
n-C_5H_{12} [kmol/sec]	0	0	0	0	0	0	0	0
HC3 [kmol/sec]	0	0	0	0	0	0	0	0.0055727
H_2O [kmol/sec]	3.168002	0.2904017	0.2904017	0.3444228	0.3444228	0	0	0
Ar [kmol/sec]	0.1712433	0.1712433	0.1712433	0.1712432	0.1712432	0.1712432	0.1712432	0.1712869
Total Flow [kmol/sec]	20.88	18.01	18.01	18.06	18.06	17.72	17.72	17.67
Total Flow [kg/sec]	602.58	550.74	550.74	551.72	551.72	545.51	545.51	543.51
Total Flow [cum/sec]	559.61	447.06	369.35	362.42	342.89	362.81	242.32	231.07
Temperature [K]	330.15	290.15	315.1662	296.336	273.15	272.8767	174.95	174.6808
Pressure [kPa]	102.0424	97.04241	127.6	122.6	117.6	110.6	105.6	110.23
Vapor Fraction	0.9977276	1	1	1	0.9848698	1	1	1
Liquid Fraction	0.0022724	0	0	0	0.0151301	0	0	0
Solid Fraction	0	0	0	0	0	0	0	0
Enthalpy [MJ/kmol]	-89.08418	-65.95152	-65.18741	-66.29349	-67.71298	-63.592	-66.52292	-65.52519
Enthalpy [MJ/kg]	-3.087351	-2.156205	-2.131223	-2.17005	-2.216515	-2.065146	-2.160327	-2.129882
Enthalpy [MW]	-1860.375	-1187.505	-1173.747	-1197.255	-1222.89	-1126.563	-1178.486	-1157.608
Entropy [kJ/kmol-K]	4.175111	4.802361	5.054943	3.447242	-1.176413	1.962236	-10.94503	-11.51576
Entropy [kJ/kg-K]	0.144695	0.1570074	0.1652652	0.112842	-0.038509	0.0637235	-0.355439	-0.374317
Density [kmol/cum]	0.0373178	0.0402759	0.0487491	0.0498317	0.0526702	0.0488284	0.0731076	0.0764545
Density [kg/cum]	1.076791	1.231915	1.491084	1.522326	1.609037	1.503572	2.251204	2.352102
Average MW	28.85457	30.58685	30.58685	30.54929	30.54929	30.79298	30.79298	30.76471
Liq Vol 60F [cum/sec]	0.7208472	0.6689024	0.6689024	0.6698845	0.6698845	0.6636671	0.6636671	0.6613939

Substream	L112B	L112C	L112D	L112E	L112F	L112G	L112H	L112I
O_2 [kmol/sec]	0.5016951	0.5024346	0.5038511	0.5061377	0.5089647	0.5113818	0.5127541	0.5128294
N_2 [kmol/sec]	14.21924	14.22198	14.22699	14.23436	14.24244	14.24867	14.25198	14.25331
CO_2 [kmol/sec]	2.668926	2.469385	2.110132	1.577457	1.004222	0.5930577	0.3888978	0.3073525
CO_2(S) [kmol/sec]	0	0	0	0	0	0	0	0
CF_4 [kmol/sec]	0	0	0	0	0	0	0	0
CH_4 [kmol/sec]	0	0	0	0	0	0	0	0
C_2H_6 [kmol/sec]	0	0	0	0	0	0	0	0
C_3H_8 [kmol/sec]	0	0	0	0	0	0	0	0
C_4H_{10} [kmol/sec]	0	0	0	0	0	0	0	0
n-C_5H_{12} [kmol/sec]	0	0	0	0	0	0	0	0
HC3 [kmol/sec]	0.0053344	0.0048735	0.0040604	0.0028941	0.0017065	0.0009183	0.0005575	0.0004216
H_2O [kmol/sec]	0	0	0	0	0	0	0	0
Ar [kmol/sec]	0.1713884	0.1716055	0.1720191	0.1726806	0.173489	0.1741731	0.1745601	0.1745983
Total Flow [kmol/sec]	17.57	17.37	17.02	16.49	15.93	15.53	15.33	15.25
Total Flow [kg/sec]	539.07	530.37	514.7	491.48	466.52	448.64	439.78	436.23
Total Flow [cum/sec]	230.09	227.4	221.78	212.56	201.3	191.6	185.71	183.14
Temperature [K]	174.3289	173.6305	172.247	169.7093	165.8132	161.3762	157.9286	156.0443
Pressure [kPa]	109.86	109.49	109.12	108.75	108.38	108.01	107.64	107.27
Vapor Fraction	1	1	1	1	1	1	1	1
Liquid Fraction	0	0	0	0	0	0	0	0
Solid Fraction	0	0	0	0	0	0	0	0
Enthalpy [MJ/kmol]	-63.60495	-59.76445	-52.62861	-41.49588	-28.72486	-19.0354	-14.06771	-12.06118
Enthalpy [MJ/kg]	-2.072667	-1.957366	-1.740007	-1.392555	-0.980911	-0.658844	-0.490333	-0.421605
Enthalpy [MW]	-1117.322	-1038.125	-895.584	-684.4133	-457.6108	-295.5855	-215.6403	-183.9151
Entropy [kJ/kmol-K]	-11.5909	-11.77326	-12.16898	-12.92052	-14.06021	-15.28744	-16.17324	-16.62349
Entropy [kJ/kg-K]	-0.377708	-0.38559	-0.402331	-0.433598	-0.480135	-0.529121	-0.563721	-0.581082
Density [kmol/cum]	0.0763467	0.0763875	0.0767281	0.0775954	0.0791386	0.0810428	0.0825429	0.0832628
Density [kg/cum]	2.342891	2.33235	2.320735	2.312219	2.317485	2.341502	2.368167	2.381966
Average MW	30.68749	30.5331	30.24621	29.79838	29.28385	28.89214	28.69014	28.60781
Liq Vol 60F [cum/sec]	0.6560108	0.6454396	0.6264148	0.5982152	0.5678949	0.5461832	0.5354198	0.5311052

Substream	L113	L114	L115	L200	L201	L214	L215	L217
O_2 [kmol/sec]	0.5012006	0.5012006	0.5011996	0.013583	0.013583	0	0	0.013583
N_2 [kmol/sec]	14.21746	14.21746	14.21711	0.0817496	0.0817496	0	0	0.0817496
CO_2 [kmol/sec]	0.276677	0.276677	0.276376	0	0	0.0653346	0.0653346	0
CO_2(S) [kmol/sec]	0	0	0	2.613448	2.613448	0	0	0.0653346
CF_4 [kmol/sec]	0	0	0	0	0	0	0	0
CH_4 [kmol/sec]	0	0	0	0	0	0	0	0
C_2H_6 [kmol/sec]	0	0	0	0	0	0	0	0
C_3H_8 [kmol/sec]	0	0	0	0	0	0	0	0
C_4H_{10} [kmol/sec]	0	0	0	0	0	0	0	0
n-C_5H_{12} [kmol/sec]	0	0	0	0	0	0	0	0
HC3 [kmol/sec]	0.0003721	0.0003721	0.0003721	34.82824	34.82824	0.1675789	0.1675789	34.8286
H_2O [kmol/sec]	0	0	0.2735192	0	0	0	0	0
Ar [kmol/sec]	0.1712435	0.1712435	0.1712434	0.0041862	0.0041862	0	0	0.0041862
Total Flow [kmol/sec]	15.17	15.17	15.44	37.54	37.54	0.23	0.23	34.99
Total Flow [kg/sec]	433.36	433.36	438.27	2630.78	2630.78	14.97	14.97	2518.66
Total Flow [cum/sec]	181.82	337.74	370.5	3.56	3.56	0.02	0.02	3.49
Temperature [K]	155.2265	273.15	288.8726	174.6808	174.8136	233.0182	217.15	175.7243
Pressure [kPa]	106.9	101.9	100	110.23	700	550	545	111.9
Vapor Fraction	1	1	1	0	0	0	0	0
Liquid Fraction	0	0	0	0.9303846	0.9303846	1	1	0.9981329
Solid Fraction	0	0	0	0.0696154	0.0696154	0	0	0.0018671
Enthalpy [MJ/kmol]	-11.32837	-7.925706	-11.61817	-211.4008	-211.3419	-250.4087	-252.1845	-195.8481
Enthalpy [MJ/kg]	-0.396474	-0.277386	-0.4093	-3.016692	-3.015851	-3.897013	-3.924649	-2.721049
Enthalpy [MW]	-171.8168	-120.2088	-179.3825	-7936.241	-7934.03	-58.32358	-58.73719	-6853.399
Entropy [kJ/kmol-K]	-16.82305	-0.132876	1.559734	-589.6009	-589.5637	-442.6289	-450.5177	-621.2194
Entropy [kJ/kg-K]	-0.588778	-0.00465	0.0549482	-8.41361	-8.41308	-6.88846	-7.01123	-8.631021
Density [kmol/cum]	0.0834166	0.0449072	0.0416726	10.54314	10.54156	11.37724	11.63673	10.01378
Density [kg/cum]	2.383449	1.283126	1.182899	738.8323	738.7212	731.0623	747.7368	720.7441
Average MW	28.57281	28.57281	28.3855	70.07704	70.07704	64.25658	64.25658	71.97519
Liq Vol 60F [cum/sec]	0.5277935	0.5277935	0.5327027	4.173377	4.173377	0.0228777	0.0228777	4.037545

Substream	L218	L220	L220A	L220B	L220C	L220D	L220E	L220F
O_2 [kmol/sec]	0.013583	0.0135808	0.0252096	0.0251344	0.0237621	0.0213453	0.0185188	0.0162328
N_2 [kmol/sec]	0.0817496	0.0817409	0.1175909	0.1162605	0.1129519	0.1067271	0.0986406	0.0912802
CO_2 [kmol/sec]	0	0	0	0	0	0	0	0
CO_2(S) [kmol/sec]	0.0653346	0.06533	0.0960049	0.1775483	0.3816938	0.7928003	1.365909	1.898409
CF_4 [kmol/sec]	0	0	0	0	0	0	0	0
CH_4 [kmol/sec]	0	0	0	0	0	0	0	0
C_2H_6 [kmol/sec]	0	0	0	0	0	0	0	0
C_3H_8 [kmol/sec]	0	0	0	0	0	0	0	0
C_4H_{10} [kmol/sec]	0	0	0	0	0	0	0	0
n-C_5H_{12} [kmol/sec]	0	0	0	0	0	0	0	0
HC3 [kmol/sec]	34.8286	34.82861	34.82866	34.8288	34.82916	34.82995	34.83113	34.8323
H_2O [kmol/sec]	0	0	0	0	0	0	0	0
Ar [kmol/sec]	0.0041862	0.0041855	0.0075404	0.0075022	0.0071152	0.0064312	0.0056229	0.0049616
Total Flow [kmol/sec]	34.99	34.99	35.08	35.16	35.35	35.76	36.32	36.84
Total Flow [kg/sec]	2518.66	2518.66	2521.53	2525.08	2533.94	2551.81	2576.77	2599.98
Total Flow [cum/sec]	3.41	3.41	3.42	3.42	3.44	3.46	3.49	3.52
Temperature [K]	154.85	154.85	155.2265	156.0443	157.9286	161.3762	165.8132	169.7093
Pressure [kPa]	106.9	106.9	106.9	107.27	107.64	108.01	108.38	108.75
Vapor Fraction	0	0	0	0	0	0	0	0
Liquid Fraction	0.9981329	0.9981331	0.9972629	0.9949495	0.9892035	0.9778267	0.9623888	0.9484687
Solid Fraction	0.0018671	0.0018669	0.0027372	0.0050505	0.0107965	0.0221733	0.0376111	0.0515312
Enthalpy [MJ/kmol]	-198.0336	-198.0337	-197.9181	-198.3688	-199.5107	-201.7952	-204.9128	-207.7319
Enthalpy [MJ/kg]	-2.751415	-2.751415	-2.753088	-2.761773	-2.783663	-2.827654	-2.888266	-2.943675
Enthalpy [MW]	-6929.881	-6929.881	-6941.979	-6973.704	-7053.637	-7215.64	-7442.397	-7653.505
Entropy [kJ/kmol-K]	-634.4466	-634.4469	-632.9083	-631.2886	-627.3954	-619.8902	-609.9061	-601.0214
Entropy [kJ/kg-K]	-8.814795	-8.814797	-8.803904	-8.789062	-8.753703	-8.686211	-8.596687	-8.516801
Density [kmol/cum]	10.24903	10.24903	10.25978	10.26759	10.28847	10.33364	10.399	10.46042
Density [kg/cum]	737.6758	737.6758	737.5706	737.4863	737.3955	737.4586	737.7744	738.1802
Average MW	71.97519	71.97521	71.8895	71.82662	71.672	71.36486	70.94665	70.56892
Liq Vol 60F [cum/sec]	4.037545	4.037546	4.040857	4.045172	4.055935	4.077643	4.107957	4.136147

Substream	L220G	L220H	L220I	L225	L230	L232	L301	L302
O_2 [kmol/sec]	0.014817	0.0140781	0.0137325	0.013583	0	0	0	0
N_2 [kmol/sec]	0.0862736	0.0835347	0.0822607	0.0817496	0	0	0	0
CO_2 [kmol/sec]	0	0	0	0	0	0	0	0
CO_2(S) [kmol/sec]	2.25748	2.456869	2.558286	0	0	0	0	0
CF_4 [kmol/sec]	0	0	0	0	0	0	6.554722	6.554722
CH_4 [kmol/sec]	0	0	0	0	0	0	0	0
C_2H_6 [kmol/sec]	0	0	0	0	0	0	0	0
C_3H_8 [kmol/sec]	0	0	0	0	0	0	0	0
C_4H_{10} [kmol/sec]	0	0	0	0	0	0	0	0
n-C_5H_{12} [kmol/sec]	0	0	0	0	0	0	0	0
HC3 [kmol/sec]	34.83311	34.83357	34.83381	34.64001	0.0210027	0.0210027	0	0
H_2O [kmol/sec]	0	0	0	0	0	0	0	0
Ar [kmol/sec]	0.0045482	0.0043313	0.0042299	0.0041862	0	0	0	0
Total Flow [kmol/sec]	37.2	37.39	37.49	34.74	0.02	0.02	6.55	6.55
Total Flow [kg/sec]	2615.64	2624.34	2628.77	2502.18	1.52	1.52	576.85	576.85
Total Flow [cum/sec]	3.54	3.55	3.56	3.47	0	0	0.6	0.46
Temperature [K]	172.247	173.6305	174.3289	174.8136	293.15	174.3556	219.5372	197.15
Pressure [kPa]	109.12	109.49	109.86	700	550	545	2942	2937
Vapor Fraction	0	0	0	0	0	0	0.0186975	0
Liquid Fraction	0.9393043	0.9342911	0.9317629	1	1	1	0.9813025	1
Solid Fraction	0.0606957	0.0657088	0.068237	0	0	0	0	0
Enthalpy [MJ/kmol]	-209.5905	-210.6073	-211.1196	-195.4702	-180.3645	-196.0751	-945.4722	-948.8198
Enthalpy [MJ/kg]	-2.98052	-3.000794	-3.01105	-2.713852	-2.499844	-2.717594	-10.74344	-10.78148
Enthalpy [MW]	-7795.975	-7875.111	-7915.362	-6790.543	-3.788149	-4.118117	-6197.307	-6219.25
Entropy [kJ/kmol-K]	-595.2174	-592.0535	-590.4575	-622.7081	-557.095	-624.717	-263.6624	-279.6177
Entropy [kJ/kg-K]	-8.464399	-8.435751	-8.421279	-8.645501	-7.721314	-8.658552	-2.996007	-3.177307
Density [kmol/cum]	10.50181	10.52474	10.53639	10.01073	8.506845	9.999978	10.89065	14.33821
Density [kg/cum]	738.4884	738.6671	738.7582	721.0413	613.7713	721.5012	958.4271	1261.829
Average MW	70.3201	70.18386	70.11494	72.02684	72.15028	72.15028	88.0046	88.0046
Liq Vol 60F [cum/sec]	4.155162	4.165725	4.171104	4.012236	0.0024307	0.0024307	0.3591816	0.3591816

Substream	L303A	L303B	L303C	L303D	L303F	L304A	L304B	L304C
O_2 [kmol/sec]	0	0	0	0	0	0	0	0
N_2 [kmol/sec]	0	0	0	0	0	0	0	0
CO_2 [kmol/sec]	0	0	0	0	0	0	0	0
CO_2(S) [kmol/sec]	0	0	0	0	0	0	0	0
CF_4 [kmol/sec]	1.605694	2.049167	0.7065056	0.3363333	1.857022	1.605694	2.049167	0.7065056
CH_4 [kmol/sec]	0	0	0	0	0	0	0	0
C_2H_6 [kmol/sec]	0	0	0	0	0	0	0	0
C_3H_8 [kmol/sec]	0	0	0	0	0	0	0	0
C_4H_{10} [kmol/sec]	0	0	0	0	0	0	0	0
n-C_5H_{12} [kmol/sec]	0	0	0	0	0	0	0	0
HC3 [kmol/sec]	0	0	0	0	0	0	0	0
H_2O [kmol/sec]	0	0	0	0	0	0	0	0
Ar [kmol/sec]	0	0	0	0	0	0	0	0
Total Flow [kmol/sec]	1.61	2.05	0.71	0.34	1.86	1.61	2.05	0.71
Total Flow [kg/sec]	141.31	180.34	62.18	29.6	163.43	141.31	180.34	62.18
Total Flow [cum/sec]	0.11	0.14	0.05	0.02	0.13	2.21	2	0.45
Temperature [K]	197.15	197.15	197.15	197.15	197.15	162.0333	166.8614	172.8753
Pressure [kPa]	2937	2937	2937	2937	2937	280	363.3685	492.0525
Vapor Fraction	0	0	0	0	0	0.3010644	0.2702339	0.2284408
Liquid Fraction	1	1	1	1	1	0.6989356	0.7297661	0.7715592
Solid Fraction	0	0	0	0	0	0	0	0
Enthalpy [MJ/kmol]	-948.8198	-948.8198	-948.8198	-948.8198	-948.8198	-948.8198	-948.8198	-948.8198
Enthalpy [MJ/kg]	-10.78148	-10.78148	-10.78148	-10.78148	-10.78148	-10.78148	-10.78148	-10.78148
Enthalpy [MW]	-1523.515	-1944.29	-670.3465	-319.1197	-1761.979	-1523.515	-1944.29	-670.3465
Entropy [kJ/kmol-K]	-279.6177	-279.6177	-279.6177	-279.6177	-279.6177	-276.7456	-277.331	-277.9251
Entropy [kJ/kg-K]	-3.177307	-3.177307	-3.177307	-3.177307	-3.177307	-3.144671	-3.151324	-3.158074
Density [kmol/cum]	14.33821	14.33821	14.33821	14.33821	14.33821	0.7270367	1.0239	1.575741
Density [kg/cum]	1261.829	1261.829	1261.829	1261.829	1261.829	63.98258	90.10791	138.6724
Average MW	88.0046	88.0046	88.0046	88.0046	88.0046	88.0046	88.0046	88.0046
Liq Vol 60F [cum/sec]	0.0879878	0.112289	0.0387146	0.0184301	0.10176	0.0879878	0.112289	0.0387146

Substream	L304D	L304F	L307A	L307B	L307C	L307D	L307F	L310
O_2 [kmol/sec]	0	0	0	0	0	0	0	0
N_2 [kmol/sec]	0	0	0	0	0	0	0	0
CO_2 [kmol/sec]	0	0	0	0	0	0	0	0
CO_2(S) [kmol/sec]	0	0	0	0	0	0	0	0
CF_4 [kmol/sec]	0.3363333	1.857022	1.605694	2.049167	0.7065056	0.3363333	1.857022	6.554722
CH_4 [kmol/sec]	0	0	0	0	0	0	0	0
C_2H_6 [kmol/sec]	0	0	0	0	0	0	0	0
C_3H_8 [kmol/sec]	0	0	0	0	0	0	0	0
C_4H_{10} [kmol/sec]	0	0	0	0	0	0	0	0
n-C_5H_{12} [kmol/sec]	0	0	0	0	0	0	0	0
HC3 [kmol/sec]	0	0	0	0	0	0	0	0
H_2O [kmol/sec]	0	0	0	0	0	0	0	0
Ar [kmol/sec]	0	0	0	0	0	0	0	0
Total Flow [kmol/sec]	0.34	1.86	1.61	2.05	0.71	0.34	1.86	6.55
Total Flow [kg/sec]	29.6	163.43	141.31	180.34	62.18	29.6	163.43	576.85
Total Flow [cum/sec]	0.02	0.13	14.03	13.69	3.45	0.49	1.87	4.74
Temperature [K]	196.4748	196.8044	292.6946	292.6946	292.6946	292.6946	292.6946	294.15
Pressure [kPa]	1559.074	2189.161	275	358.3685	487.0525	1554.074	2184.161	2952
Vapor Fraction	0	0	1	1	1	1	1	1
Liquid Fraction	1	1	0	0	0	0	0	0
Solid Fraction	0	0	0	0	0	0	0	0
Enthalpy [MJ/kmol]	-948.8198	-948.8198	-934.1077	-934.14	-934.19	-934.6145	-934.8733	-935.0955
Enthalpy [MJ/kg]	-10.78148	-10.78148	-10.61431	-10.61467	-10.61524	-10.62006	-10.62301	-10.62553
Enthalpy [MW]	-319.1197	-1761.979	-1499.892	-1914.208	-660.0104	-314.342	-1736.081	-6129.291
Entropy [kJ/kmol-K]	-279.1616	-279.3714	-197.7426	-200.023	-202.6965	-213.3944	-216.8743	-219.8556
Entropy [kJ/kg-K]	-3.172125	-3.174509	-2.246957	-2.27287	-2.303249	-2.424809	-2.464352	-2.498228
Density [kmol/cum]	14.40286	14.37139	0.114426	0.1496854	0.2046416	0.6864311	0.9943139	1.383913
Density [kg/cum]	1267.518	1264.749	10.07001	13.17301	18.0094	60.4091	87.5042	121.7907
Average MW	88.0046	88.0046	88.0046	88.0046	88.0046	88.0046	88.0046	88.0046
Liq Vol 60F [cum/sec]	0.0184301	0.10176	0.0879878	0.112289	0.0387146	0.0184301	0.10176	0.3591816

Substream	L311	L313	L402	L403A	L403C	L404	L405	L406
O_2 [kmol/sec]	0	0	0	0	0	0	0	0
N_2 [kmol/sec]	0	0	0	0	0	0	0	0
CO_2 [kmol/sec]	0	0	0	0	0	2.613448	2.613448	2.548113
CO_2(S) [kmol/sec]	0	0	2.613448	2.613448	0	0	0	0
CF_4 [kmol/sec]	6.554722	6.554722	0	0	0	0	0	0
CH_4 [kmol/sec]	0	0	0	0	0	0	0	0
C_2H_6 [kmol/sec]	0	0	0	0	0	0	0	0
C_3H_8 [kmol/sec]	0	0	0	0	0	0	0	0
C_4H_{10} [kmol/sec]	0	0	0	0	0	0	0	0
n-C_5H_{12} [kmol/sec]	0	0	0	0	0	0	0	0
HC3 [kmol/sec]	0	0	0.1882221	0	0.1882221	0.1882221	0.1882221	0.0206432
H_2O [kmol/sec]	0	0	0	0	0	0	0	0
Ar [kmol/sec]	0	0	0	0	0	0	0	0
Total Flow [kmol/sec]	6.55	6.55	2.8	2.61	0.19	2.8	2.8	2.57
Total Flow [kg/sec]	576.85	576.85	128.6	115.02	13.58	128.6	128.6	113.63
Total Flow [cum/sec]	4.74	2.1	0.09	0.07	0.02	0.11	8.4	8.45
Temperature [K]	294.15	219.5925	174.8136	174.8136	174.8136	206.87	233.15	233.0182
Pressure [kPa]	2952	2947	700	700	700	560	555	550
Vapor Fraction	1	1	0	0	0	0	0.9166318	1
Liquid Fraction	0	0	0.0671821	0	1	1	0.0833682	0
Solid Fraction	0	0	0.9328179	1	0	0	0	0
Enthalpy [MJ/kmol]	-935.0955	-941.0276	-408.1451	-423.423	-196.0127	-397.7467	-382.688	-394.682
Enthalpy [MJ/kg]	-10.62553	-10.69294	-8.891985	-9.621108	-2.716729	-8.665442	-8.337367	-8.922201
Enthalpy [MW]	-6129.291	-6168.174	-1143.488	-1106.594	-36.89393	-1114.355	-1072.165	-1013.842
Entropy [kJ/kmol-K]	-219.8556	-243.4244	-178.5891	-146.4784	-624.4443	-129.1121	-60.53518	-25.81975
Entropy [kJ/kg-K]	-2.498228	-2.766042	-3.890802	-3.328312	-8.654773	-2.812878	-1.318839	-0.583683
Density [kmol/cum]	1.383913	3.114456	30.77811	36.19937	9.994772	24.46042	0.3336509	0.3038254
Density [kg/cum]	121.7907	274.0865	1412.726	1593.127	721.1256	1122.741	15.31469	13.44
Average MW	88.0046	88.0046	45.90034	44.0098	72.15028	45.90034	45.90034	44.23594
Liq Vol 60F [cum/sec]	0.3591816	0.3591816	0.161141	0.139358	0.0217829	0.161141	0.161141	0.1382632

Substream	L407	L408	L413	L414	L416	L500	L501	L503
O_2 [kmol/sec]	0	0	0	0	0	0	0	0
N_2 [kmol/sec]	0	0	0	0	0	0	0	0
CO_2 [kmol/sec]	2.548113	2.548113	2.548113	2.548113	2.548113	0	0	0
CO_2(S) [kmol/sec]	0	0	0	0	0	0	0	0
CF_4 [kmol/sec]	0	0	0	0	0	0	0	0
CH_4 [kmol/sec]	0	0	0	0	0	5.594444	5.594444	5.594444
C_2H_6 [kmol/sec]	0	0	0	0	0	0.1766667	0.1766667	0.1766667
C_3H_8 [kmol/sec]	0	0	0	0	0	0.1177778	0.1177778	0.1177778
C_4H_{10} [kmol/sec]	0	0	0	0	0	0	0	0
n-C_5H_{12} [kmol/sec]	0	0	0	0	0	0	0	0
HC3 [kmol/sec]	0.0206432	0.0206432	0.0206432	0.0206432	0.0206432	0	0	0
H_2O [kmol/sec]	0	0	0	0	0	0	0	0
Ar [kmol/sec]	0	0	0	0	0	0	0	0
Total Flow [kmol/sec]	2.57	2.57	2.57	2.57	2.57	5.89	5.89	5.89
Total Flow [kg/sec]	113.63	113.63	113.63	113.63	113.63	100.26	100.26	100.26
Total Flow [cum/sec]	11.1	10.26	0.1	0.1	0.14	1.55	6.19	3.53
Temperature [K]	292.6946	300.1044	220.6609	224.2239	292.6946	153.7398	174.65	294.15
Pressure [kPa]	545	604	599	10000	9995	1145	1140	3700
Vapor Fraction	1	1	0	0	0	0.2541398	0.9497007	1
Liquid Fraction	0	0	1	1	1	0.7458602	0.0502993	0
Solid Fraction	0	0	0	0	0	0	0	0
Enthalpy [MJ/kmol]	-392.3205	-392.0459	-410.3974	-410.0156	-403.4676	-86.84232	-81.29796	-76.69716
Enthalpy [MJ/kg]	-8.868818	-8.862609	-9.277463	-9.268833	-9.120808	-5.100978	-4.775311	-4.505068
Enthalpy [MW]	-1007.776	-1007.07	-1054.211	-1053.23	-1036.41	-511.4048	-478.7546	-451.6611
Entropy [kJ/kmol-K]	-16.72893	-16.63713	-97.53696	-97.37034	-72.13801	-165.8413	-130.7107	-118.7529
Entropy [kJ/kg-K]	-0.378175	-0.3761	-2.204926	-2.201159	-1.630756	-9.741248	-7.677736	-6.975354
Density [kmol/cum]	0.2315197	0.2504755	25.92133	25.6413	17.97415	3.795225	0.9507914	1.666024
Density [kg/cum]	10.24149	11.08002	1146.655	1134.267	795.1034	64.61234	16.18688	28.36347
Average MW	44.23594	44.23594	44.23594	44.23594	44.23594	17.02464	17.02464	17.02464
Liq Vol 60F [cum/sec]	0.1382632	0.1382632	0.1382632	0.1382632	0.1382632	0.3249619	0.3249619	0.3249619

Substream	L504	L514	L555	L700	L701	L702	L703	L704
O_2 [kmol/sec]	0	0	0	0	0	0	0	0
N_2 [kmol/sec]	0	0	0	0	0	0	0	0
CO_2 [kmol/sec]	0	0	0	0	0	0	0	0
CO_2(S) [kmol/sec]	0	0	0	0	0	0	0	0
CF_4 [kmol/sec]	0	0	0	0	0	0	0	0
CH_4 [kmol/sec]	5.594444	5.594444	5.594444	0.0916666	0.0916666	0.0916666	0.0916666	0.0885649
C_2H_6 [kmol/sec]	0.1766667	0.1766667	0.1766667	1.833333	1.833333	1.833333	1.833333	1.599146
C_3H_8 [kmol/sec]	0.1177778	0.1177778	0.1177778	0	0	0	0	0
C_4H_{10} [kmol/sec]	0	0	0	0.0611111	0.0611111	0.0611111	0.0611111	0.0250966
n-C_5H_{12} [kmol/sec]	0	0	0	0.1833333	0.1833333	0.1833333	0.1833333	0.021686
HC3 [kmol/sec]	0	0	0	0	0	0	0	0
H_2O [kmol/sec]	0	0	0	0	0	0	0	0
Ar [kmol/sec]	0	0	0	0	0	0	0	0
Total Flow [kmol/sec]	5.89	5.89	5.89	2.17	2.17	2.17	2.17	1.73
Total Flow [kg/sec]	100.26	100.26	100.26	73.38	73.38	73.38	73.38	52.53
Total Flow [cum/sec]	12.26	3.53	0.31	0.18	0.13	2.59	50.72	0.15
Temperature [K]	292.8861	294.15	179.15	294.15	195.15	179.8196	292.8861	294.15
Pressure [kPa]	1135	3700	3695	4500	4495	108	103	4500
Vapor Fraction	1	1	0	0	0	0.0843688	1	0
Liquid Fraction	0	0	1	1	1	0.9156311	0	1
Solid Fraction	0	0	0	0	0	0	0	0
Enthalpy [MJ/kmol]	-76.20628	-76.69716	-86.60761	-102.62	-111.7629	-112.0547	-91.09246	-95.36387
Enthalpy [MJ/kg]	-4.476234	-4.505068	-5.087191	-3.034002	-3.304316	-3.312944	-2.693186	-3.148834
Enthalpy [MW]	-448.7703	-451.6611	-510.0226	-222.6284	-242.4634	-243.0965	-197.62	-165.408
Entropy [kJ/kmol-K]	-107.8006	-118.7529	-165.974	-263.2139	-300.5046	-300.3634	-199.0132	-236.2198
Entropy [kJ/kg-K]	-6.332033	-6.975354	-9.749048	-7.782027	-8.884542	-8.880367	-5.883905	-7.799777
Density [kmol/cum]	0.4803897	1.666024	18.80735	12.05824	16.54087	0.8375653	0.0427693	11.30665
Density [kg/cum]	8.178463	28.36347	320.1884	407.8495	559.4672	28.32923	1.446601	342.4272
Average MW	17.02464	17.02464	17.02464	33.82331	33.82331	33.82331	33.82331	30.28545
Liq Vol 60F [cum/sec]	0.3249619	0.3249619	0.3249619	0.187	0.187	0.187	0.187	0.1449254

Substream	L705	L724	L725	L726	L727	L734	L735	L736
O_2 [kmol/sec]	0	0	0	0	0	0	0	0
N_2 [kmol/sec]	0	0	0	0	0	0	0	0
CO_2 [kmol/sec]	0	0	0	0	0	0	0	0
CO_2(S) [kmol/sec]	0	0	0	0	0	0	0	0
CF_4 [kmol/sec]	0	0	0	0	0	0	0	0
CH_4 [kmol/sec]	0.0916666	2.24E-05	0.0003895	0.000619	0.0020708	2.24E-05	0.0003895	0.000619
C_2H_6 [kmol/sec]	1.833333	0.0025073	0.0401658	0.0554037	0.1361106	0.0025073	0.0401658	0.0554037
C_3H_8 [kmol/sec]	0	0	0	0	0	0	0	0
C_4H_{10} [kmol/sec]	0.0611111	0.0008847	0.0110033	0.0106579	0.0134685	0.0008847	0.0110033	0.0106579
n-C_5H_{12} [kmol/sec]	0.1833333	0.0096737	0.0768246	0.0452302	0.0299186	0.0096737	0.0768246	0.0452302
HC3 [kmol/sec]	0	0	0	0	0	0	0	0
H_2O [kmol/sec]	0	0	0	0	0	0	0	0
Ar [kmol/sec]	0	0	0	0	0	0	0	0
Total Flow [kmol/sec]	2.17	0.01	0.13	0.11	0.18	0.01	0.13	0.11
Total Flow [kg/sec]	73.38	0.83	7.4	5.56	7.07	0.83	7.4	5.56
Total Flow [cum/sec]	0.18	0	0.01	0.01	0.02	0	0.01	0.01
Temperature [K]	298.6033	294.15	294.15	294.15	294.15	295.8477	295.9011	295.9806
Pressure [kPa]	4500	675.8083	1086.621	1745.325	2801.504	4500	4500	4500
Vapor Fraction	0	0	0	0	0	0	0	0
Liquid Fraction	1	1	1	1	1	1	1	1
Solid Fraction	0	0	0	0	0	0	0	0
Enthalpy [MJ/kmol]	-102.0409	-156.9712	-146.934	-132.2252	-112.1182	-156.5458	-146.5743	-131.9575
Enthalpy [MJ/kg]	-3.01688	-2.489842	-2.550381	-2.662008	-2.88039	-2.483095	-2.544136	-2.656619
Enthalpy [MW]	-221.372	-2.05446	-18.86387	-14.79743	-20.35714	-2.048892	-18.81768	-14.76748
Entropy [kJ/kmol-K]	-261.26	-477.5582	-436.6433	-378.0423	-300.2136	-477.4383	-436.5403	-377.9679
Entropy [kJ/kg-K]	-7.724258	-7.574925	-7.578956	-7.610892	-7.712687	-7.573021	-7.577169	-7.609394
Density [kmol/cum]	11.74915	9.463198	9.986442	10.83239	11.94072	9.434197	9.952048	10.78598
Density [kg/cum]	397.3951	596.6037	575.3448	538.0578	464.7885	594.7753	573.3632	535.7528
Average MW	33.82331	63.04462	57.61259	49.67122	38.92465	63.04462	57.61259	49.67122
Liq Vol 60F [cum/sec]	0.187	0.0014097	0.0133152	0.0109614	0.0163881	0.0014097	0.0133152	0.0109614

Substream	L737	L741	L961	L964	L970	L971	L972	L972A
O_2 [kmol/sec]	0	0	0	0	0	1.08E-06	8.44E-07	5.18E-07
N_2 [kmol/sec]	0	0	0	0	0	0.000348	0.0003071	0.0001886
CO_2 [kmol/sec]	0	0	0	0	0	0.000301	0.0002753	0.000169
CO_2(S) [kmol/sec]	0	0	0	0	0	0	0	0
CF_4 [kmol/sec]	0	0	0	0	0	0	0	0
CH_4 [kmol/sec]	0.0020708	0.0031017	0	0	0	0	0	0
C_2H_6 [kmol/sec]	0.1361106	0.2341874	0	0	0	0	0	0
C_3H_8 [kmol/sec]	0	0	0	0	0	0	0	0
C_4H_{10} [kmol/sec]	0.0134685	0.0360144	0	0	0	0	0	0
n-C_5H_{12} [kmol/sec]	0.0299186	0.1616473	0	0	0	0	0	0
HC3 [kmol/sec]	0	0	0	0.00E+00	0.00E+00	2.05E-23	1.10E-23	6.76E-24
H_2O [kmol/sec]	0	0	13.33333	13.33333	19.44444	19.17093	16.01223	9.831511
Ar [kmol/sec]	0	0	0	0.00E+00	0.00E+00	3.61E-09	2.63E-09	1.61E-09
Total Flow [kmol/sec]	0.18	0.43	13.33	13.33	19.44	19.17	16.01	9.83
Total Flow [kg/sec]	7.07	20.85	240.2	240.2	350.3	345.39	288.49	177.13
Total Flow [cum/sec]	0.02	0.04	0.24	0.24	0.35	0.34	0.29	0.18
Temperature [K]	296.0803	296.6825	289.15	292.6946	289.15	276.2872	274.2	274.2
Pressure [kPa]	4500	4500	150	145	100	100	127.6	127.6
Vapor Fraction	0	0	0	0	0.00E+00	0.00E+00	3.23E-05	3.23E-05
Liquid Fraction	1	1	1	1	1	1	0.9999677	0.9999677
Solid Fraction	0	0	0	0	0	0	0	0
Enthalpy [MJ/kmol]	-111.9685	-128.6674	-288.4703	-288.1813	-286.9202	-287.9174	-289.6877	-289.6877
Enthalpy [MJ/kg]	-2.876544	-2.684399	-16.01253	-15.99649	-15.92649	-15.98132	-16.07954	-16.07954
Enthalpy [MW]	-20.32995	-55.964	-3846.271	-3842.418	-5579.004	-5519.83	-4638.715	-2848.171
Entropy [kJ/kmol-K]	-300.1815	-365.1156	-170.46	-169.4663	-166.7756	-170.3094	-174.7881	-174.7881
Entropy [kJ/kg-K]	-7.711861	-7.617436	-9.461966	-9.406811	-9.257452	-9.453301	-9.701869	-9.701869
Density [kmol/cum]	11.85731	10.95656	55.78117	55.59249	56.28965	56.8146	54.78699	54.78699
Density [kg/cum]	461.5418	525.1651	1004.913	1001.514	1014.074	1023.564	987.0381	987.0381
Average MW	38.92465	47.93156	18.01528	18.01528	18.01528	18.01587	18.01592	18.01592
Liq Vol 60F [cum/sec]	0.0163881	0.0420745	0.2406861	0.2406861	0.3510005	0.3460913	0.2890695	0.1774887

Substream	L972B	L972C	L973A	L973B	L991	L992	L993	LE416A
O_2 [kmol/sec]	9.45E-08	2.31E-07	5.18E-07	9.45E-08	1.62E-07	3.61E-07	0	0
N_2 [kmol/sec]	3.44E-05	8.41E-05	0.0001886	3.44E-05	1.49E-07	3.70E-07	0	0
CO_2 [kmol/sec]	3.08E-05	7.54E-05	0.000169	3.08E-05	0	0	0	2.613448
CO_2(S) [kmol/sec]	0	0	0	0	0	0	0	0
CF_4 [kmol/sec]	0	0	0	0	0	0	0	0
CH_4 [kmol/sec]	0	0	0	0	0	0	0	0
C_2H_6 [kmol/sec]	0	0	0	0	0	0	0	0
C_3H_8 [kmol/sec]	0	0	0	0	0	0	0	0
C_4H_{10} [kmol/sec]	0	0	0	0	0	0	0	0
n-C_5H_{12} [kmol/sec]	0	0	0	0	0	0	0	0
HC3 [kmol/sec]	1.23E-24	3.02E-24	6.76E-24	1.23E-24	0	0	0	0
H_2O [kmol/sec]	1.79337	4.387352	9.831511	1.79337	2.8776	4.333331	0.3444228	0
Ar [kmol/sec]	2.94E-10	7.20E-10	1.61E-09	2.94E-10	4.51E-08	1.01E-07	0	0
Total Flow [kmol/sec]	1.79	4.39	9.83	1.79	2.88	4.33	0.34	2.61
Total Flow [kg/sec]	32.31	79.05	177.13	32.31	51.84	78.07	6.2	115.02
Total Flow [cum/sec]	0.03	0.08	0.18	0.03	0.05	0.08	0.01	0.1
Temperature [K]	274.2	274.2	292.6946	292.8861	290.15	296.336	272.8767	216.58
Pressure [kPa]	127.6	127.6	122.6	122.6	97.04241	122.6	110.6	695
Vapor Fraction	3.23E-05	3.23E-05	3.16E-05	3.16E-05	0	0	0	0
Liquid Fraction	0.9999677	0.9999677	0.9999684	0.9999684	1	1	1	1
Solid Fraction	0	0	0	0	0	0	0	0
Enthalpy [MJ/kmol]	-289.6877	-289.6877	-288.1779	-288.1623	-288.3896	-287.8848	-289.8	-412.6267
Enthalpy [MJ/kg]	-16.07954	-16.07954	-15.99574	-15.99487	-16.00805	-15.98003	-16.08634	-9.37579
Enthalpy [MW]	-519.5361	-1271.008	-2833.328	-516.8005	-829.87	-1247.5	-99.81373	-1078.378
Entropy [kJ/kmol-K]	-174.7881	-174.7881	-169.4594	-169.406	-170.1777	-168.4581	-175.1902	-95.7361
Entropy [kJ/kg-K]	-9.701869	-9.701869	-9.40609	-9.403129	-9.446294	-9.350841	-9.724535	-2.175336
Density [kmol/cum]	54.78699	54.78699	53.72387	53.71352	55.728	55.3979	56.63866	26.5866
Density [kg/cum]	987.0381	987.0381	967.8849	967.6985	1003.956	998.0089	1020.361	1170.071
Average MW	18.01592	18.01592	18.01592	18.01592	18.01528	18.01528	18.01528	44.0098
Liq Vol 60F [cum/sec]	0.0323757	0.079205	0.1774887	0.0323757	0.0519448	0.0782229	0.0062173	0.139358

Substream	LE416C	LM416
O_2 [kmol/sec]	0	0
N_2 [kmol/sec]	0	0
CO_2 [kmol/sec]	0	2.613448
CO_2(S) [kmol/sec]	0	0
CF_4 [kmol/sec]	0	0
CH_4 [kmol/sec]	0	0
C_2H_6 [kmol/sec]	0	0
C_3H_8 [kmol/sec]	0	0
C_4H_{10} [kmol/sec]	0	0
n-C_5H_{12} [kmol/sec]	0	0
HC3 [kmol/sec]	0.1882221	0.1882221
H_2O [kmol/sec]	0	0
Ar [kmol/sec]	0	0
Total Flow [kmol/sec]	0.19	2.8
Total Flow [kg/sec]	13.58	128.6
Total Flow [cum/sec]	0.02	0.11
Temperature [K]	216.58	206.8418
Pressure [kPa]	695	695
Vapor Fraction	0	0
Liquid Fraction	1	1
Solid Fraction	0	0
Enthalpy [MJ/kmol]	-191.1396	-397.7467
Enthalpy [MJ/kg]	-2.649187	-8.665442
Enthalpy [MW]	-35.97669	-1114.355
Entropy [kJ/kmol-K]	-599.5079	-129.138
Entropy [kJ/kg-K]	-8.309155	-2.813444
Density [kmol/cum]	9.50519	24.46204
Density [kg/cum]	685.8021	1122.816
Average MW	72.15028	45.90034
Liq Vol 60F [cum/sec]	0.0217829	0.161141

C CCC NG & CCC LNG APPARATUS PIPING & INSTRUMENTATION DIAGRAM

The apparatus diagram is broken into six regions: wall, gas cabinet, rack, fume hood, HX cold box, and bubbler box. The apparatus diagram is presented on the next two pages. The process flow diagram is simplified and does not contain all detail.

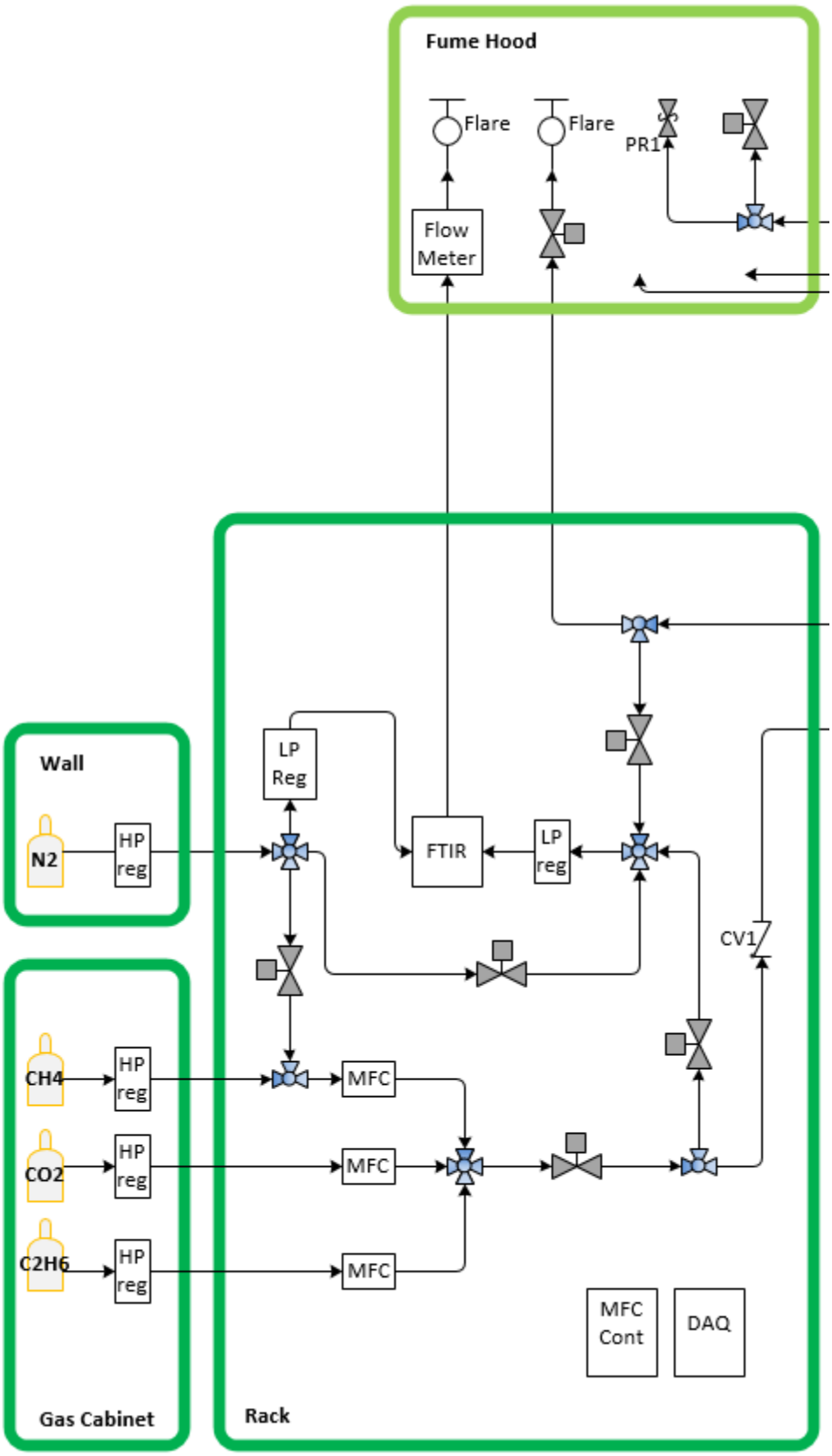

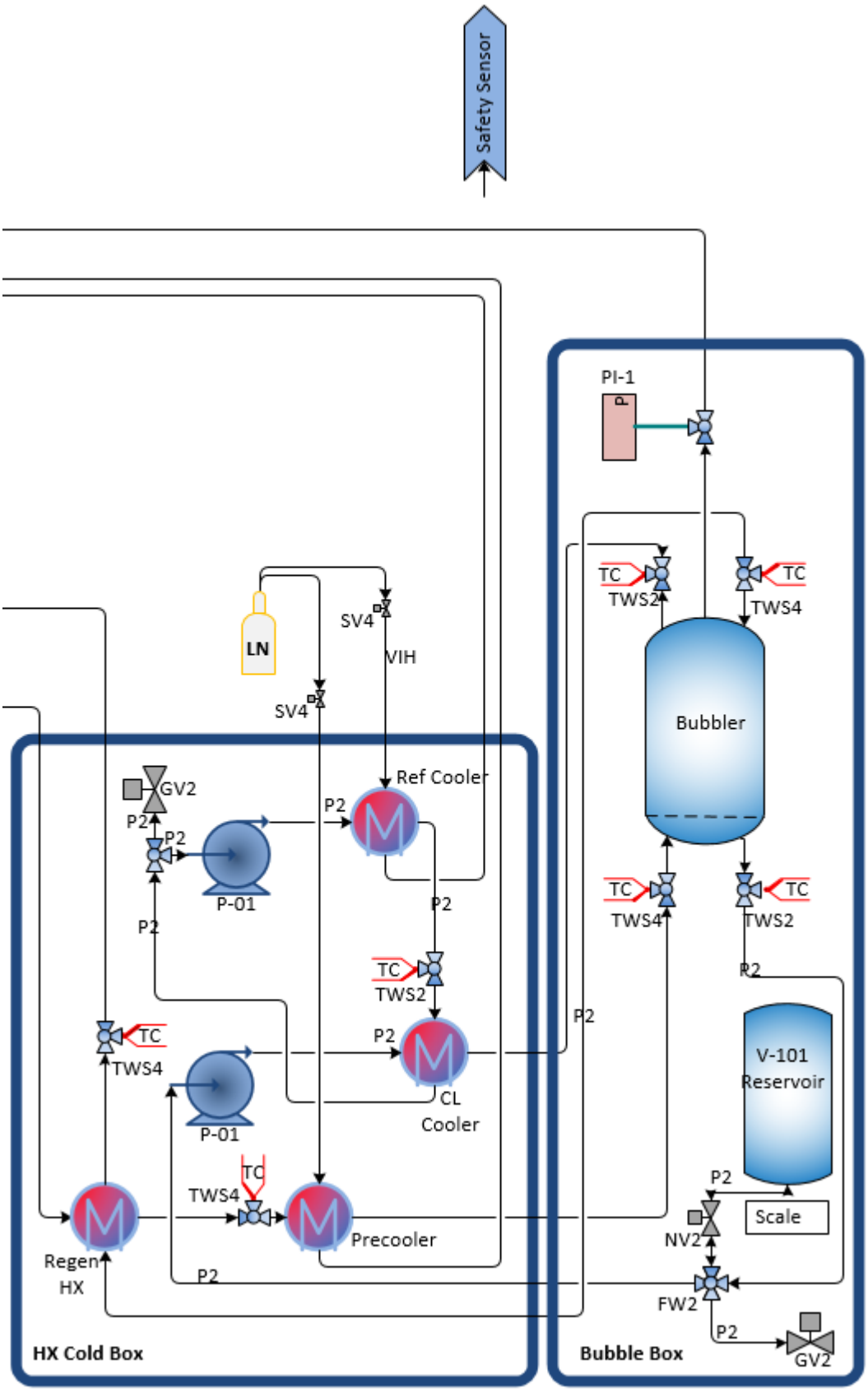

D NATURAL GAS APPARATUS WIRING DIAGRAM

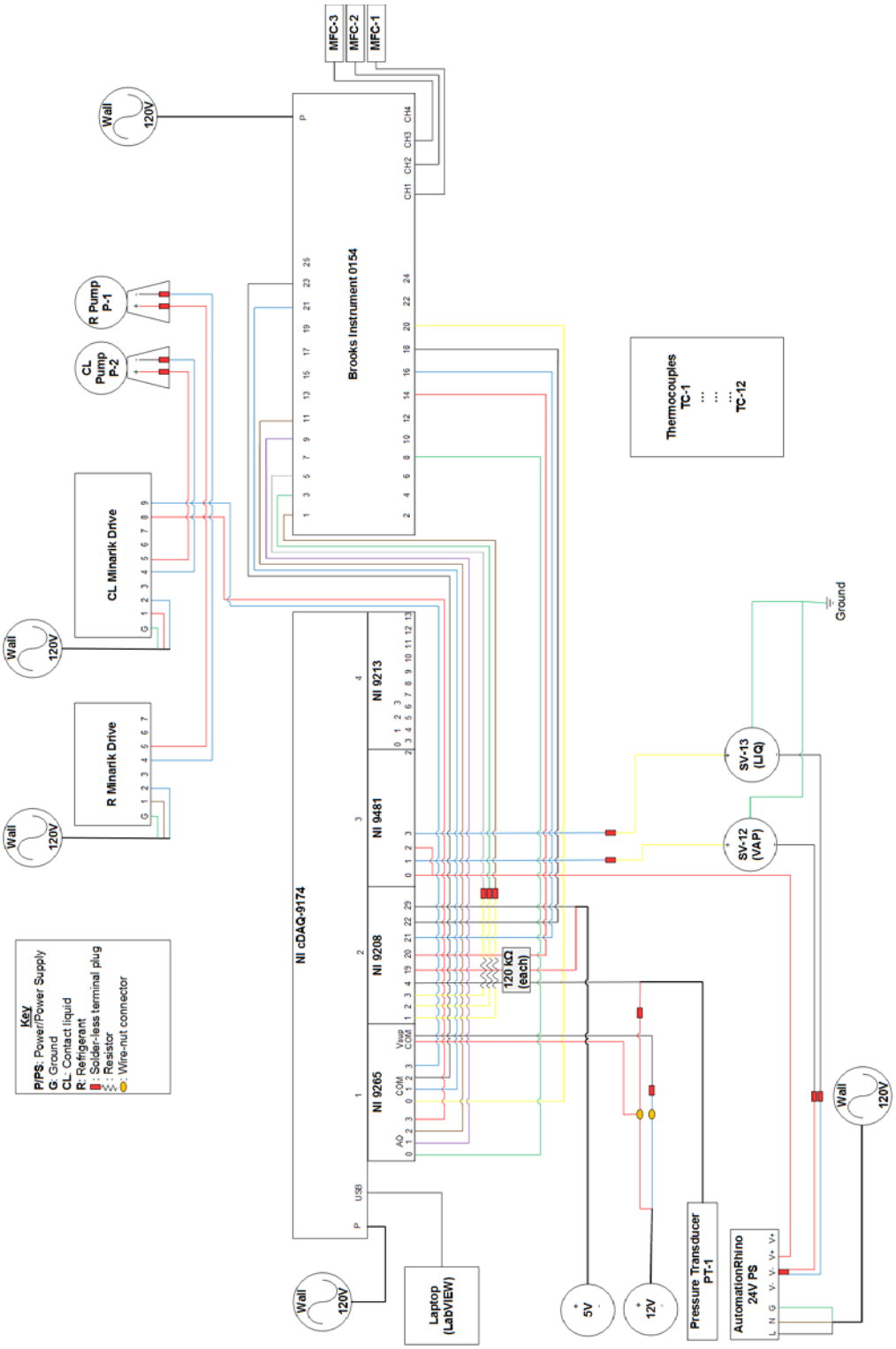

E LABVIEW PROGRAM TO CONTROL NATURAL GAS APPARATUS

LabVIEW front panel contains controls for pump flow rate and mass flow controllers. The front panel also allows the user to adjust the P&ID controller parameters on the fly. The P&ID controller adjusts the total flow rate of the mass flow controllers to achieve the set pressure. The display also has numerical and graphical indicators for actual flow through mass flow controllers, two pressure transducers, and 16 thermocouples that are broken into four groups: bubbler contact liquid, bubbler gas, metal contacts, and other process areas.

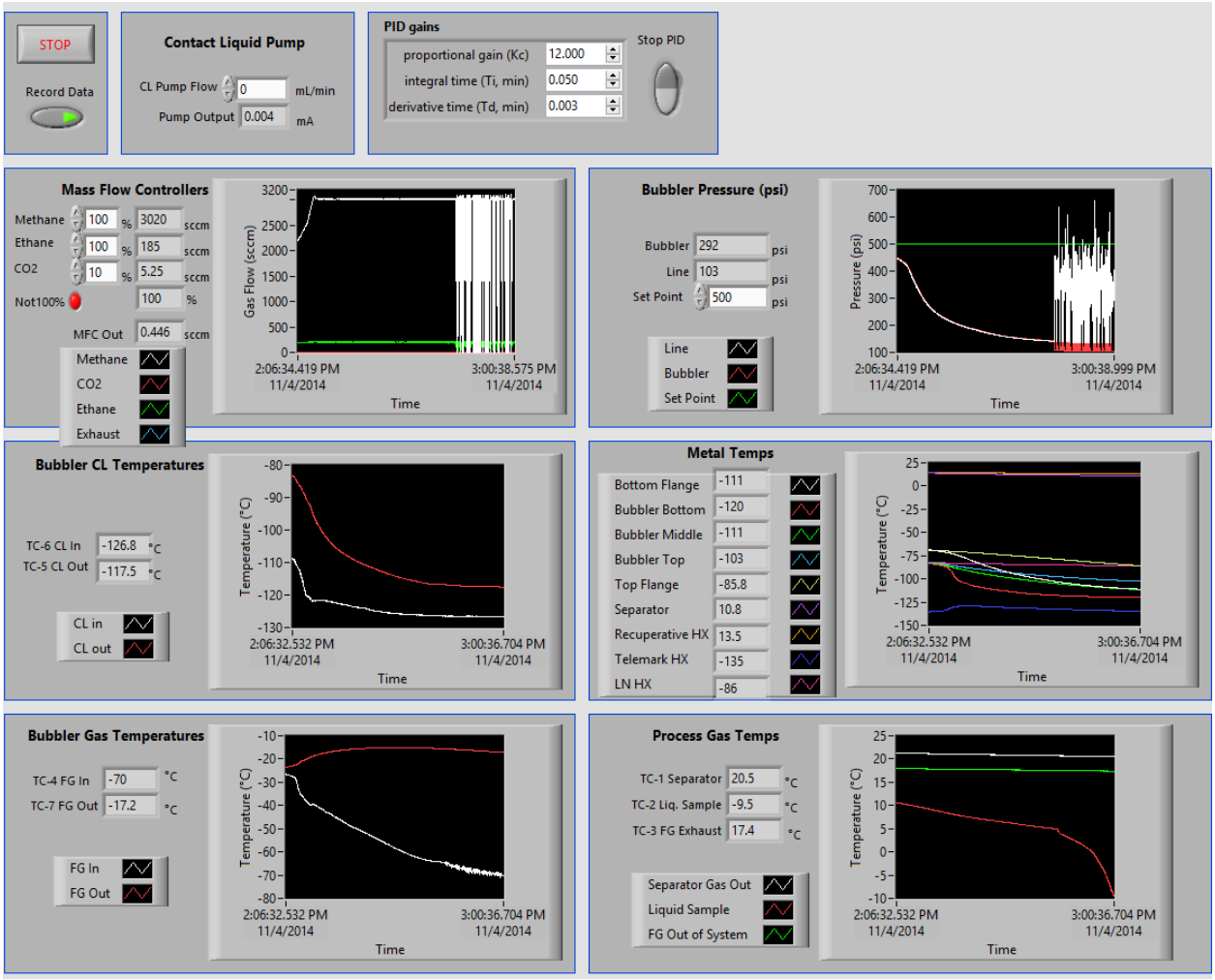

To support the front panel, the inputs, outputs, and signal manipulation occurs in the block diagram. The block diagram is presented in several sections. The first section is reading the 16 thermocouple signals and displaying them. On the right side of the 'Write to Measurement File' block records the thermocouples and every other signal to a comma separated value file with a time stamp.

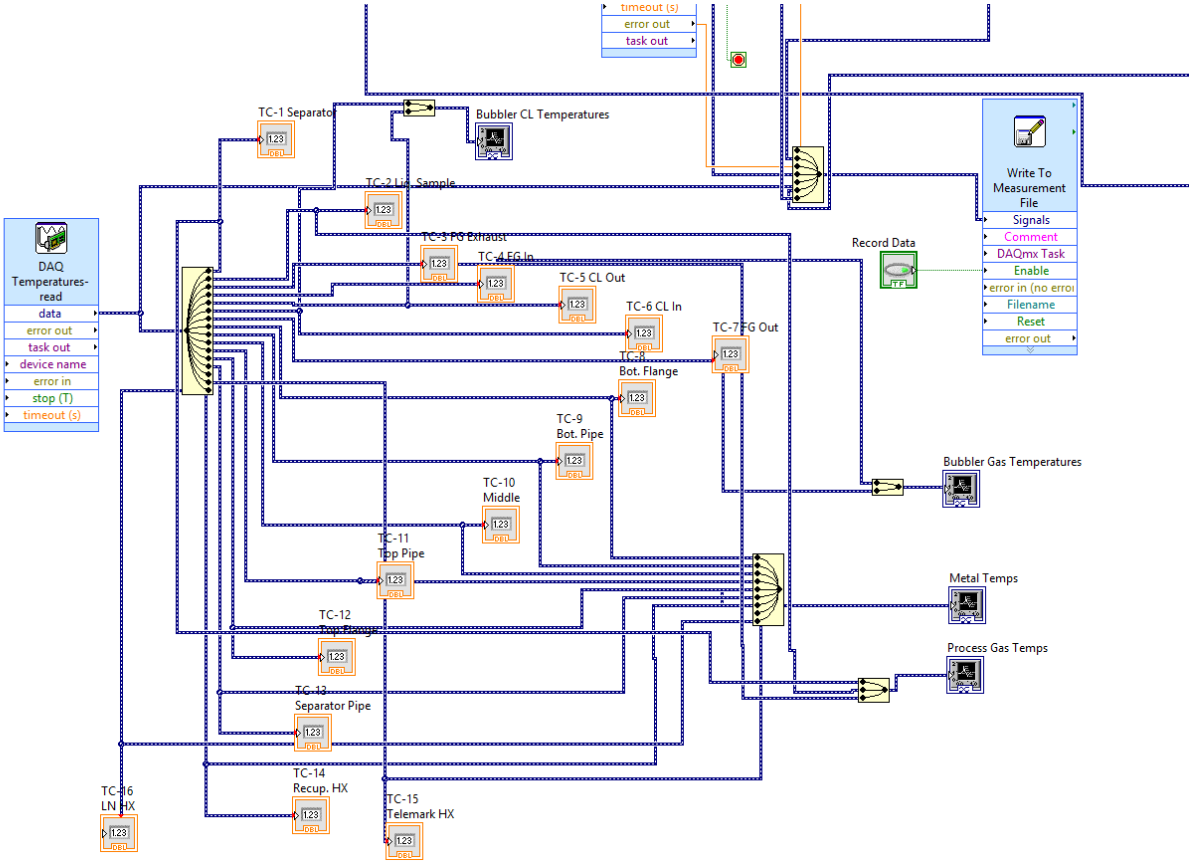

The block on the left, takes the set pump flow rate and sends a 4-20 mA signal to the pump motor controller. The blocks on the right take the mass flow set points and in send 4-20 mA signals to control the mass flow controllers. Since the mass flow controller operates on a voltage signal, precision resistors are used to convert the amperage control signal into a voltage control signal.

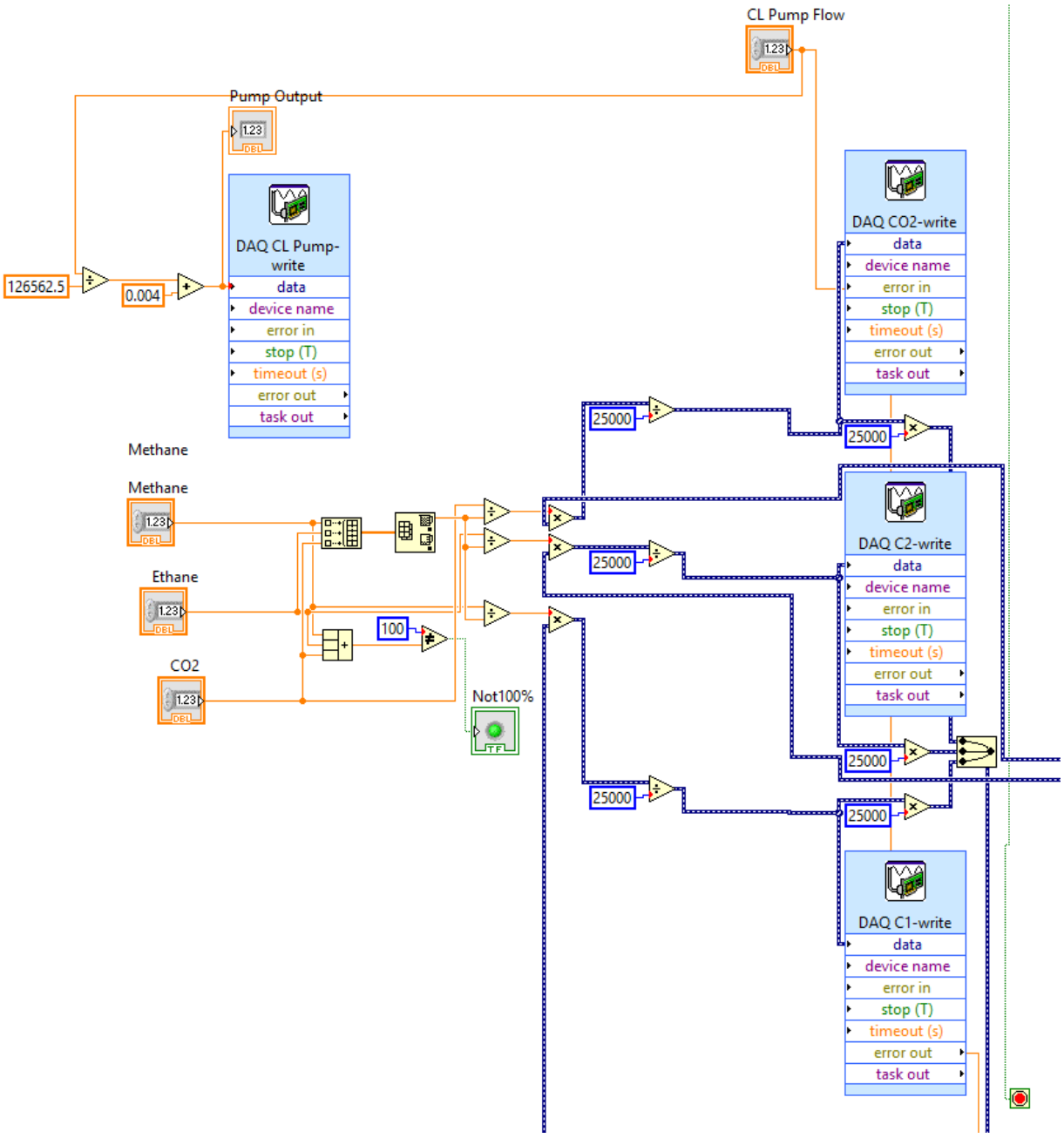

The flow rates of the mass flow controller are scaled as a whole in order to maintain a desired set pressure. This PID controller compares the setpoint pressure with the bubbler pressure to scale the mass flow controllers equally from 0-100 %.

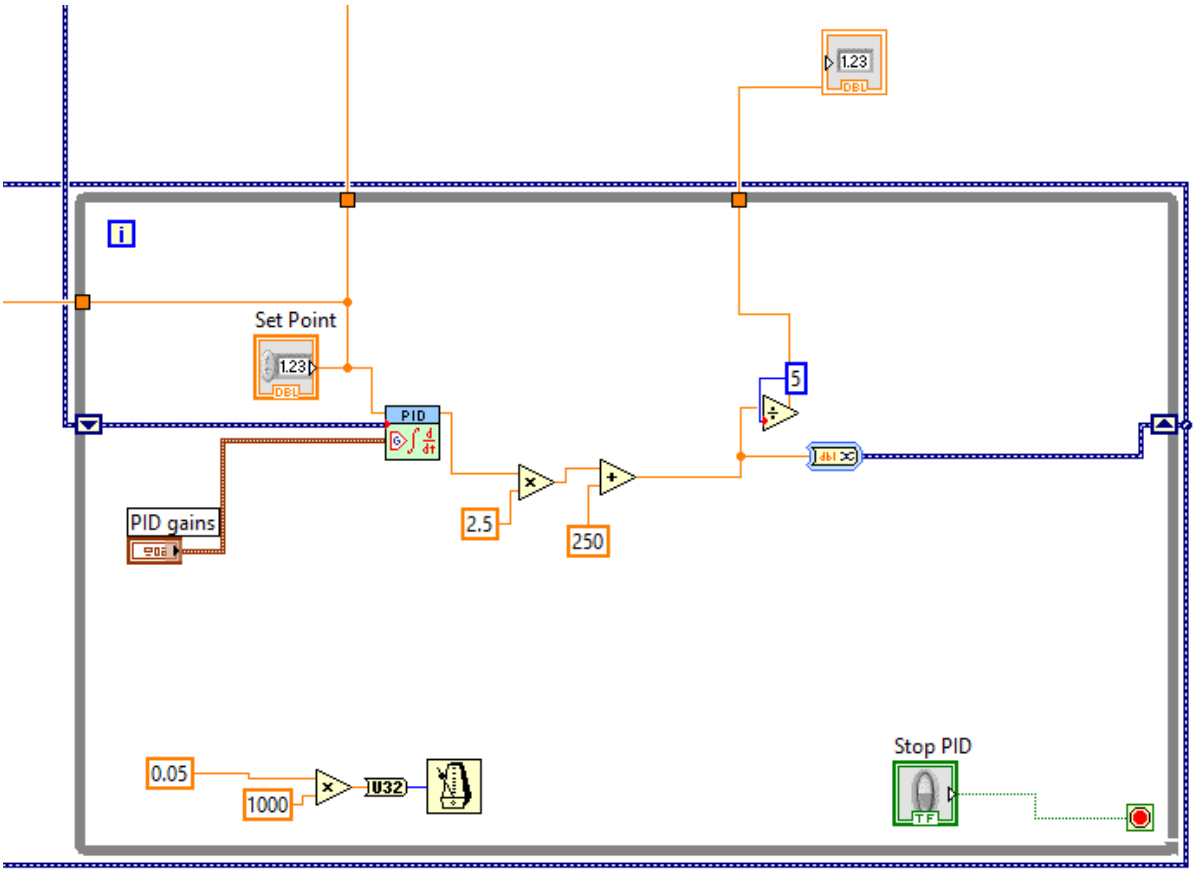

To ensure that the mass flow controllers are working properly and to record actual mass flow, a feedback from the controller is returned to the DAQ and recorded in the system. Also, in this block the pressure transducer 4-20 mA signals are read and converted to units of psi. For some experiments a Horiba was used to measure CO_2 concentration, and thus another input signal is optional from the Horiba to record CO_2 concentration. If CO_2 concentration was measured with the FTIR, the CO_2 concentrations were recorded with software from MKS.

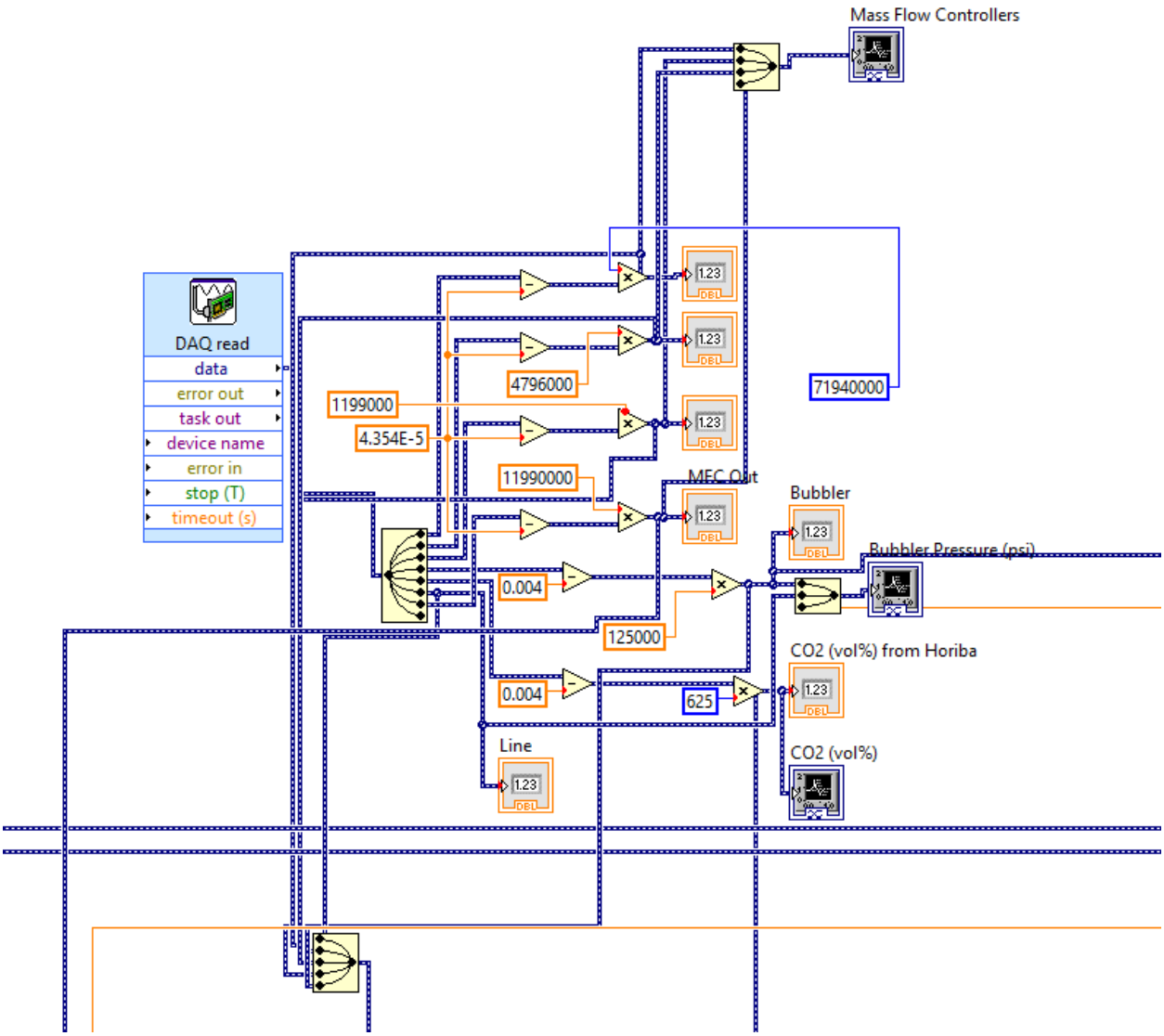

F CALIBRATION SUMMARIES FOR MKS

CO_2 Calibration for 13 ppm to 4030 ppm

Calibration Name: Calibration Editor - C:\OLT\Methods\CO2andCH4\CO2ppmv3 13ppm to 4030ppm150C_11.lrf
*** Regions ***
Region 00 - 634.47 to 701.73 cm-1
Region 01 - 600.00 to 634.23 cm-1
Region 02 - 701.97 to 847.81 cm-1
Region 03 - 2035.28 to 2080.60 cm-1
Region 04 - 2223.55 to 2391.09 cm-1
Region 05 - 3533.00 to 3762.49 cm-1
*** Segments Removed From Analysis Region ***
Region 00 - 665.09 to 672.08 cm-1
*** Parameters ***
Baseline Correction : ON
Use Mutations : OFF
*** Interpolation ***
Type of interpolation : Quadratic
Force Through Zero : ON
Exclude Zero Conc : OFF
Min % Residuals : OFF
Quant w/ Highest : OFF
Correlation Coefficient R : 0.999998
Max Residuals : 3.006 %
*** Calibration Spectra ***

Filename	Temp (C)	Pressure (atm)	Conc (ppm-m)	Residual (%)
C:\OLT\Methods\CO2ppm calibration\Carbon Dioxide (13.8ppm, 5.10m, 149C).lab	149.020	0.996	70.348	-0.526 %
C:\OLT\Methods\CO2ppm calibration\Carbon Dioxide (27.6ppm, 5.10m, 150C).lab	149.765	0.996	140.695	2.884 %
C:\OLT\Methods\CO2ppm calibration\Carbon Dioxide (55.2ppm, 5.10m, 150C).lab	149.765	0.996	281.391	2.862 %
C:\OLT\Methods\CO2ppm calibration\Carbon Dioxide (103.5ppm, 5.10m, 150C).lab	149.765	0.996	527.608	2.304 %
C:\OLT\Methods\CO2ppm calibration\Carbon Dioxide (103.5ppm, 5.10m, 149C).lab	149.392	0.996	527.608	3.006 %
C:\OLT\Methods\CO2ppm calibration\Carbon Dioxide (151.7ppm, 5.10m, 149C).lab	149.020	0.996	773.824	2.240 %
C:\OLT\Methods\CO2ppm calibration\Carbon Dioxide (206.9ppm, 5.10m, 150C).lab	149.765	0.996	1055.215	0.853 %
C:\OLT\Methods\CO2ppm calibration\Carbon Dioxide (248.3ppm, 5.10m, 149C).lab	149.020	0.996	1266.258	0.679 %
C:\OLT\Methods\CO2ppm calibration\Carbon Dioxide (303.5ppm, 5.10m, 149C).lab	149.392	0.996	1547.649	-0.086 %
C:\OLT\Methods\CO2ppm calibration\Carbon Dioxide (358.6ppm, 5.10m, 149C).lab	149.392	0.996	1829.039	-0.612 %
C:\OLT\Methods\CO2ppm calibration\Carbon Dioxide (413.8ppm, 5.10m, 149C).lab	149.392	0.996	2110.430	-0.874 %
C:\OLT\Methods\CO2ppm calibration\Carbon Dioxide (4000ppm, 5.10m, 150C).lab	150.000	1.000	20440.001	0.004 %

*** Calibration Information ***

CO_2 Calibration for 0.4 % to 20.1 %

Calibration Name: Calibration Editor - C:\OLT\Methods\CO2andCH4\CO2% 150C_10.lrf
*** Regions ***
Region 00 - 2211.02 to 2236.33 cm-1
Region 01 - 500.44 to 1127.69 cm-1
Region 02 - 2236.57 to 2525.36 cm-1
Region 03 - 3271.69 to 3852.89 cm-1
Region 04 - 1819.77 to 2210.78 cm-1
*** Segments Removed From Analysis Region ***
*** Parameters ***
Baseline Correction : ON
Use Mutations : OFF
*** Interpolation ***
Type of interpolation : Spline
Force Through Zero : ON
Exclude Zero Conc : OFF
Min % Residuals : OFF
Quant w/ Highest : OFF
Correlation Coefficient R : 0.999789
Max Residuals : 3.903 %
*** Calibration Spectra ***

Filename	Temp (C)	Pressure (atm)	Conc (%-m)	Residual (%)
C:\OLT\Methods\CO2 Calibration\Carbon Dioxide (0.4%, 5.10m, 150C).lab	150.000	1.000	2.061	-3.903 %
C:\OLT\Methods\CO2 Calibration\Carbon Dioxide (1.0%, 5.10m, 150C).lab	150.000	1.000	5.131	1.309 %
C:\OLT\Methods\CO2 Calibration\Carbon Dioxide (2.0%, 5.10m, 150C).lab	150.000	1.000	10.261	-1.128 %
C:\OLT\Methods\CO2 Calibration\Carbon Dioxide (3.0%, 5.10m, 150C).lab	150.000	1.000	15.454	1.388 %
C:\OLT\Methods\CO2 Calibration\Carbon Dioxide (4.4%, 5.10m, 150C).lab	150.000	1.000	22.307	-1.410 %
C:\OLT\Methods\CO2 Calibration\Carbon Dioxide (6.6%, 5.10m, 150C).lab	150.000	1.000	33.461	0.219 %
C:\OLT\Methods\CO2 Calibration\Carbon Dioxide (8.3%, 5.10m, 150C).lab	150.000	1.000	42.384	-0.266 %
C:\OLT\Methods\CO2 Calibration\Carbon Dioxide (10.1%, 5.10m, 150C).lab	150.000	1.000	51.307	1.254 %
C:\OLT\Methods\CO2 Calibration\Carbon Dioxide (12.2%, 5.10m, 150C).lab	150.000	1.000	62.461	-2.134 %
C:\OLT\Methods\CO2 Calibration\Carbon Dioxide (16.2%, 5.10m, 150C).lab	150.000	1.000	82.538	1.105 %
C:\OLT\Methods\CO2 Calibration\Carbon Dioxide (20.1%, 5.10m, 150C).lab	150.000	1.000	102.614	1.464 %

*** Calibration Information ***

CH_4 Calibration for 40 % to 100 %

Calibration Name: Calibration Editor - C:\OLT\Methods\CO2andCH4\Methane2 40% to 100%_8.lrf
*** Regions ***
Region 00 - 2469.44 to 2549.00 cm-1
Region 01 - 986.19 to 2019.62 cm-1
Region 02 - 2213.92 to 2469.20 cm-1
Region 03 - 2549.24 to 3252.66 cm-1
Region 04 - 3700.55 to 4780.99 cm-1
*** Segments Removed From Analysis Region ***
*** Parameters ***
Baseline Correction : ON
Use Mutations : OFF
*** Interpolation ***
Type of interpolation : Quadratic
Force Through Zero : ON
Exclude Zero Conc : OFF
Min % Residuals : OFF
Quant w/ Highest : OFF
Correlation Coefficient R : 0.999905
Max Residuals : 2.005 %
*** Calibration Spectra ***

Filename	Temp (C)	Pressure (atm)	Conc (%-m)	Residual (%)
C:\OLT\Methods\methane calibration\methane (40%, 150C).LAB	149.758	0.853	204.400	-2.005 %
C:\OLT\Methods\methane calibration\methane (50%, 150C).LAB	149.758	0.853	255.500	-0.409 %
C:\OLT\Methods\methane calibration\methane (60%, 150C).LAB	149.769	0.853	306.600	0.557 %
C:\OLT\Methods\methane calibration\methane (70%, 150C).LAB	149.803	0.853	357.700	0.797 %
C:\OLT\Methods\methane calibration\methane (80%, 150C).LAB	149.668	0.852	408.800	0.824 %
C:\OLT\Methods\methane calibration\methane (90%, 150C).LAB	149.769	0.852	459.900	0.268 %
C:\OLT\Methods\methane calibration\methane (95%, 150C).LAB	149.882	0.852	485.450	-0.047 %
C:\OLT\Methods\methane calibration\methane (98%, 150C).LAB	149.792	0.852	500.780	-0.114 %
C:\OLT\Methods\methane calibration\methane (100%, 150C).LAB	149.792	0.852	511.000	-0.614 %

*** Calibration Information ***
:

C_2H_6 Calibration for 0.13 % to 20 %

Calibration Name: Calibration Editor - C:\OLT\Methods\CO2andCH4\C2H6 0.13% to 20% linear 150C_9.lrf
*** Regions ***
Region 00 - 3260.61 to 3305.21 cm-1
Region 01 - 693.54 to 1005.71 cm-1
Region 02 - 1094.18 to 1874.26 cm-1
Region 03 - 1952.37 to 2082.30 cm-1
Region 04 - 2150.04 to 2415.21 cm-1
Region 05 - 2519.10 to 3260.37 cm-1
Region 06 - 3305.45 to 3460.69 cm-1
Region 07 - 3595.93 to 4537.28 cm-1
*** Segments Removed From Analysis Region ***
*** Parameters ***
Baseline Correction : ON
Use Mutations : OFF
*** Interpolation ***
Type of interpolation : Linear
Force Through Zero : ON
Exclude Zero Conc : OFF
Min % Residuals : OFF
Quant w/ Highest : OFF
Correlation Coefficient R : 0.999928
Max Residuals : 41.350 %
*** Calibration Spectra ***

Filename	Temp (C)	Pressure (atm)	Conc (%-m)	Residual (%)
C:\OLT\Methods\Ethane calibration\Ethane (0.13%, 5.11 m, 150C).LAB	149.794	0.855	0.664	41.350 %
C:\OLT\Methods\Ethane calibration\Ethane (1%, 5.11 m, 150C).LAB	149.750	0.855	5.110	16.119 %
C:\OLT\Methods\Ethane calibration\Ethane (2%, 5.11 m, 150C).LAB	149.723	0.855	10.220	1.099 %
C:\OLT\Methods\Ethane calibration\Ethane (3%, 5.11 m, 150C).LAB	149.750	0.855	15.330	0.927 %
C:\OLT\Methods\Ethane calibration\Ethane (4%, 5.11 m, 150C).LAB	149.779	0.855	20.440	0.253 %
C:\OLT\Methods\Ethane calibration\Ethane (5%, 5.11 m, 150C).LAB	149.779	0.855	25.550	0.286 %
C:\OLT\Methods\Ethane calibration\Ethane (8%, 5.11 m, 150C).LAB	149.824	0.855	40.880	1.225 %
C:\OLT\Methods\Ethane calibration\Ethane (10%, 5.11 m, 150C).LAB	149.866	0.855	51.100	0.041 %
C:\OLT\Methods\Ethane calibration\Ethane (15%, 5.11 m, 150C).LAB	149.692	0.855	76.650	0.584 %
C:\OLT\Methods\Ethane calibration\Ethane (20%, 5.11 m, 150C).LAB	149.881	0.855	102.200	-0.710 %

*** Calibration Information ***

Hydrocarbon 3 Calibration for 1581 ppm to 5184 ppm

Calibration Name: Calibration Editor - C:\OLT\Methods\CO2andCH4\HC3 1581ppm to 5184ppm 150C_5.lrf
*** Regions ***
Region 00 - 993.66 to 1016.08 cm-1
Region 01 - 694.26 to 935.32 cm-1
Region 02 - 939.18 to 993.42 cm-1
Region 03 - 1016.32 to 2124.24 cm-1
Region 04 - 2541.76 to 3251.45 cm-1
Region 05 - 3465.52 to 4013.69 cm-1
Region 06 - 4031.05 to 4486.66 cm-1
*** Segments Removed From Analysis Region ***
*** Parameters ***
Baseline Correction : ON
Use Mutations : OFF
*** Interpolation ***
Type of interpolation : Quadratic
Force Through Zero : ON
Exclude Zero Conc : OFF
Min % Residuals : OFF
Quant w/ Highest : OFF
Correlation Coefficient R : 0.995159
Max Residuals : 7.233 %
*** Calibration Spectra ***

Filename	Temp (C)	Pressure (atm)	Conc (ppm-m)	Residual (%)	
C:\OLT\Methods\HC3 Calibration\HC3B (1581ppm, 150 C).LAB	149.358	0.905	8078.910	4.792 %	
C:\OLT\Methods\HC3 Calibration\HC3 (1581ppm, 150C).LAB	149.494	0.963	8078.910	-5.986 %	
C:\OLT\Methods\HC3 Calibration\HC3B (3748ppm, 150C).LAB	149.596	0.863	19152.281	7.233 %	
C:\OLT\Methods\HC3 Calibration\HC3 (3748ppm, 150C).LAB	149.634	0.901	19152.281	-0.846 %	
C:\OLT\Methods\HC3 Calibration\HC3B (5184ppm, 150C).LAB	149.837	0.858	26490.241	-0.463 %	
C:\OLT\Methods\HC3 Calibration\HC3 (5184ppm, 150C).LAB	149.648	0.868	26490.241	0.282 %	

*** Calibration Information ***